

# **Design of Aerospace Thermal Structures using Multidisciplinary Structural and Topology Optimization**

Joshua D. Deaton

Wright State University

**- Research Proposal -**

## **Abstract**

The design of structures subjected to elevated temperature environments has long been an important area of study in the aerospace industry. This is especially true in the modern day, where new problems related to embedded engine aircraft and high temperature exhaust present new structural design challenges not found in past thermal structures applications. In this document, the thermoelastic response of a special class of thermal structures, called engine exhaust-washed structures, is investigated. As a more advanced design tool for these components, structural topology optimization is proposed to develop lightweight structures that satisfy challenging criteria related to damaging thermal stresses. Primary technical contributions to date in this work include an investigation of the effect of nonlinearity, the development of topology optimization-based methods for stiffening thermally loaded structures, and demonstrating the effectiveness of stress-based topology optimization techniques for thermal stresses. Future work includes applying the methods to structures of greater geometric complexity and incorporating design-dependent temperature loading into the topology optimization framework.

## **Contents**

<b>1</b>	<b>Introduction</b>	<b>2</b>
1.1	Motivation . . . . .	2
1.2	Chapter Outline . . . . .	2
1.3	Historical Perspective on Thermal Structures . . . . .	3
1.4	Engine Exhaust-Washed Structures . . . . .	5
1.5	Technical Challenges for Thermoelastic Optimization . . . . .	7

<b>2 Characteristic Responses of Thermal Structures</b>	<b>10</b>
2.1 Exhaust Structure Thermoelastic Response . . . . .	10
2.1.1 Thermal-Structural Analysis Technique . . . . .	11
2.1.2 Heat Transfer Model . . . . .	12
2.1.3 Heat Transfer Results . . . . .	15
2.1.4 Structural Model . . . . .	17
2.1.5 Structural Results . . . . .	19
2.1.6 Summary . . . . .	22
2.2 Significance of Geometric Nonlinearity . . . . .	23
2.2.1 Beam Strip Model . . . . .	24
2.2.2 Deformation . . . . .	25
2.2.3 Parametric Contributions . . . . .	26
2.2.4 Boundary Contributions . . . . .	28
2.2.5 Summary . . . . .	30
2.3 Challenging Design Response . . . . .	30
2.3.1 Observations from Beam Strip Model . . . . .	30
2.3.2 Curved Shell Model . . . . .	31
2.4 Chapter Summary . . . . .	33
<b>3 Topology Optimization</b>	<b>34</b>
3.1 Background . . . . .	34
3.2 Methods . . . . .	34
3.2.1 Homogenization . . . . .	35
3.2.2 Density-based Methods . . . . .	35
3.2.3 Hard-kill Methods . . . . .	41
3.2.4 Boundary Variation Methods . . . . .	42
3.2.5 A Biologically-inspired Method . . . . .	45
3.3 Literature Formulations & Applications . . . . .	47
3.3.1 Minimum Compliance . . . . .	47
3.3.2 Thermoelastic Structures . . . . .	48
3.3.3 Heat Transfer . . . . .	51
3.3.4 Coupled Thermal-Structures . . . . .	54
3.3.5 Stress-based Topology Optimization . . . . .	56

3.4	Chapter Summary . . . . .	59
<b>4</b>	<b>Thermoelastic Stiffening via Topology Optimization</b>	<b>61</b>
4.1	Introduction . . . . .	61
4.1.1	Displacement-stress Relationship . . . . .	61
4.1.2	Functional Topology Design Space . . . . .	63
4.2	Finite Element Parameterization . . . . .	64
4.3	Topology Optimization Formulations . . . . .	66
4.3.1	Minimum Compliance with Thermal Loading . . . . .	66
4.3.2	Artificial Mechanical Load Method . . . . .	68
4.3.3	Thermoelastic Combination Method . . . . .	69
4.4	Computational Implementation . . . . .	72
4.5	Example 1: Stiffened Beam Strip . . . . .	72
4.5.1	Design Problem Setup . . . . .	72
4.5.2	Topology Optimization Results . . . . .	73
4.5.3	Qualitative Assessment . . . . .	77
<b>5</b>	<b>Stress-based Topology Optimization with Thermal Loads</b>	<b>80</b>
5.1	A Practical Consideration . . . . .	80
5.2	Finite Element Analysis for Stress . . . . .	81
5.3	Relaxed Stress . . . . .	82
5.4	Adaptive Stress Aggregation . . . . .	84
5.5	Problem Formulations . . . . .	85
5.6	Demonstration . . . . .	86
5.6.1	Results . . . . .	87
5.6.2	Effectiveness of Adaptive Stress Measure . . . . .	88
5.7	Chapter Summary . . . . .	89
<b>6</b>	<b>Future Work</b>	<b>92</b>
6.1	Coupled Thermal-Structural Topology Optimization . . . . .	92
6.1.1	Finite Element Formulation . . . . .	93
6.1.2	Sensitivity Analysis . . . . .	94
6.2	Topology Layout for Engine Exhaust-Washed Structures . . . . .	96
<b>7</b>	<b>Research Plan Summary</b>	<b>98</b>

## List of Figures

1	Example applications in aerospace thermal structures . . . . .	4
2	Military aircraft with embedded engine configurations . . . . .	6
3	Cross-section of a notional embedded engine configuration showing ducted exhaust path . . . . .	6
4	Engine exhaust-washed structure (EEWS) configuration . . . . .	7
5	Standard design optimization process . . . . .	8
6	Typical mission profile for an ESAV aircraft . . . . .	10
7	Finite element discretization of EEWS system . . . . .	11
8	Exhaust temperature, altitude, and Mach for an ESAV mission . . . . .	12
9	Ambient/adiabatic wall temperatures and convection coefficients for ESAV mission . . . . .	14
10	Temperature distribution in EEWS during transient analysis . . . . .	16
11	Transient temperatures at specified nodes in EEWS system . . . . .	17
12	Boundary conditions on EEWS structural model . . . . .	18
13	Displacement and stress distributions in EEWS structure . . . . .	20
14	Principle stress in nozzle structure of EEWS system . . . . .	21
15	Maximum principle stresses in nozzle structure along section lines . . . . .	22
16	Stress response at several locations in EEWS as a function of time . . . . .	23
17	Parameterized curved beam strip model . . . . .	25
18	Deformation of curved beam strip under temperature loads . . . . .	26
19	Maximum stress and displacement in curved beam strip with clamped and simply supported boundaries	27
20	Stress as a function of thickness for beam strip with finite rotational stiffness at boundaries . . . . .	29
21	Stress as a function of thickness for beam strip with finite axial stiffness at boundaries . . . . .	29
22	Schematic of curved shell model . . . . .	32
23	Finite element model and characteristic results for thermally loaded curved shell . . . . .	32
24	Stress as a function of thickness for curved shell with finite in-plane stiffness at boundaries . . . . .	33
25	Three categories of structural optimization. . . . .	34
26	Microstructures for 2D continuum topology optimization with homogenization . . . . .	36
27	Interpolation functions for density-based topology optimization . . . . .	38
28	Example of checkerboarding in topology optimization . . . . .	38
29	Example of mesh dependency in topology optimization . . . . .	39

30	Neighborhood definition for sensitivity and density filters. . . . .	40
31	Result of filtering and projection methods in topology optimization . . . . .	42
32	Implicit versus explicit parameterization of topology design domain . . . . .	43
33	Level set definition of topology optimization . . . . .	44
34	Domain definition using a phase field function . . . . .	45
35	Example of a cellular division process using map-L system . . . . .	46
36	Results from Rodrigues and Hernandes for different temperatures . . . . .	49
37	Comparison of SIMP and RAMP for thermoelastic minimum compliance . . . . .	50
38	Example of topology optimization for an optimal heat conductor . . . . .	52
39	Resolution of numerical oscillations in modeling for topology optimization with convection . . . . .	54
40	Thermally actuated compliant mechanisms . . . . .	55
41	Comparison of stress constraints in topology optimization . . . . .	59
42	Thermal stress as a function of displacement at center of beam strip . . . . .	62
43	Reaction loads as a function of displacement at center of beam strip . . . . .	62
44	Two-dimensional schematic of exhaust-washed and sub-structure region. . . . .	63
45	Topology optimization design space for stiffened strip example . . . . .	64
46	Generalized thermoelastic structural design domain . . . . .	64
47	Beam strip domain for the minimum compliance with thermal loading formulation . . . . .	68
48	Beam strip domain for the artificial mechanical load formulation with three load sets . . . . .	69
49	Beam strip domain for the thermoelastic combination formulation . . . . .	71
50	FEA mesh for topology optimization stiffened strip example . . . . .	73
51	Results for for minimum compliance with thermal load formulation . . . . .	74
52	Compliance sensitivity for each element for various density fields . . . . .	75
53	Topology results for the fictitious load method . . . . .	76
54	Iteration history for the fictitious load method . . . . .	76
55	Topology results for the thermoelastic combination method . . . . .	77
56	Iteration history for the thermoelastic combination method . . . . .	78
57	Stress and compliance in two axial rods . . . . .	80
58	Application of relaxation to remove the singularity phenomena . . . . .	83
59	Design domain for bi-clamped structure subjected to combined loading . . . . .	87
60	Demonstration results for both topology optimization with stress criteria . . . . .	90
61	Effectiveness of adaptive stress measure in the stress-constrained demonstration problem . . . . .	91
62	Heat transfer effects in topology optimization . . . . .	92

63	2D EEWs substructure topology design domains	96
64	Full EEWs substructure topology design domain	97

## **List of Tables**

1	Material and surface properties for thermal analysis	15
2	Structural material properties for the EEWs system	19
3	Comparison of various engineering material properties at high operating temperature	25
4	Reaction and displacement comparison for strip stiffening example topology results	79

# 1 Introduction

## 1.1 Motivation

The motivation for the research proposed in this document is twofold. First, there exists a lack of appropriate design methodologies for a new class of aerospace thermal structures that are related to low observability aircraft and sustained hypersonic flight vehicles. In these cases, the requirements on platform capabilities demand improved performance from thermally loaded structures and create new thermoelastic design scenarios that are not well addressed with existing design tools. In fact, application of conventional design practices may well lead to inherently flawed designs. Second, within the multidisciplinary optimization community, topology optimization has become the most active area of research; however, the majority of applications have been restricted to problems of purely mechanical origin. This is despite the fact that the fundamental properties of topology optimization indicate it would be a valuable design tool for a number of alternative and multiphysics applications, including thermoelasticity. To this end, the proposed work aims to investigate and develop topology optimization formulations suitable for thermal-structural design environments. These developments will then be applied to aerospace thermal structures design problems, specifically engine exhaust-washed structures, to develop structural systems with improved thermoelastic performance.

## 1.2 Chapter Outline

The remaining sections of Chapter 1 provide a short historical perspective and literature review on thermal structures for aerospace applications, highlight the particular design application of aircraft engine exhaust-washed structures, and describe some of the basic design challenges associated with applying multidisciplinary design and topology optimization methods to thermal structures. Chapter 2 demonstrates the basic thermoelastic responses (using thermal and structural finite element analysis) of characteristic thermal structures that the design methodologies discussed in this work must address. Chapter 3 gives a literature review of topology optimization including methods, basic formulations, and topics relevant to the developments in this work. Chapters 4 and 5 describe topology optimization work that has already been completed during the course of Ph.D. studies. This work addresses situations for stiffening thermally restrained structures and incorporating thermal stress design criteria using topology optimization, both of which are motivated by observations made in Chapter 2. Chapter 6 outlines future work that will address the coupled thermal-structural design scenario with both heat transfer and structural effects in topology optimization in addition to the application of the developed methods real-world aerospace thermal structures problems. Finally, Chapter 7 provides a summary of the completed work and research plan.

### 1.3 Historical Perspective on Thermal Structures

The design of aerospace structures subjected to elevated temperature environments has been a critical area of research since the advent of supersonic flight in the late 1940's [1]. As flight speed increased, designers realized that the elevated temperatures resulting from high speed aerodynamic phenomena and their effects on aircraft structural performance could place a "thermal barrier" on supersonic flight. In response, a new area of research emerged, known as *thermal structures*, to help overcome this barrier with advances in aerospace materials and improved structural designs. The thermal structures field focuses on both the transfer of thermal energy (heat transfer) throughout a structure in addition to the mechanical effects of reduced or elevated temperatures and spatial or temporal temperature gradients on structural components. Fundamentally, these effects are related to two primary considerations. First, the properties of most engineering materials are dependent on temperature. Thus the presence of a thermal environment may reduce structural performance by influencing a components behavior at the material level. Second, elevated or reduced temperatures induce thermal expansion or contraction in structures that, if restrained by boundary fixivity or spatial temperature gradients, leads to thermal stresses, buckling, and other detrimental thermoelastic effects. Since its inception, the thermal structures field has evolved to address these issues alongside varying applications and challenges in the aerospace, defense, energy, and manufacturing industries.

The foundation for the study of thermal structures is well developed in two classical texts written in the 1950's. The first, by Boley and Weiner [2], gives a comprehensive mathematical treatment, beginning with the coupled governing energy equation for heat transfer and elastic equilibrium equations, for the case of linear thermoelasticity. The need for a coupled solution is discussed and guidelines for when a weak coupling of the thermal and structural systems may be suitable are provided. Analytical solutions are presented for a variety of structural elements including straight and curved beams, trusses and frames, flat plates and curved shells, and linear thermal buckling for various load and boundary conditions. A limited treatment of inelastic (material nonlinear) thermal structures is also given.

The second text, by Gatewood [3], approaches the topic from a more applied standpoint, especially for aerospace components. Analytical and semi-analytical solutions are provided for basic geometry as in [2], but additional discussion focuses on assembled structures such as skin-stringer combinations and joints in two dimensions. Common to both texts are extensive references to research works that give a flavor to early challenges in the thermal structures field, which at this time stemmed primarily from supersonic flight.

A more recent text, by Thornton [1], highlights the evolution of aerospace thermal structures applications. Presentation spans from the time of [2, 3], through increased supersonic flight speeds in the 1950s, space applications including deployable space structures, atmospheric reentry vehicles, and the Space Shuttle in the 1960s-1970s, to the National Aerospace Plane (NASP) in the late 1980s. In addition, sufficient discussion of mathematical foundations and additional references are provided. Some applications highlighted in [1] along with some other aerospace thermal

structures are shown in Figure 1.

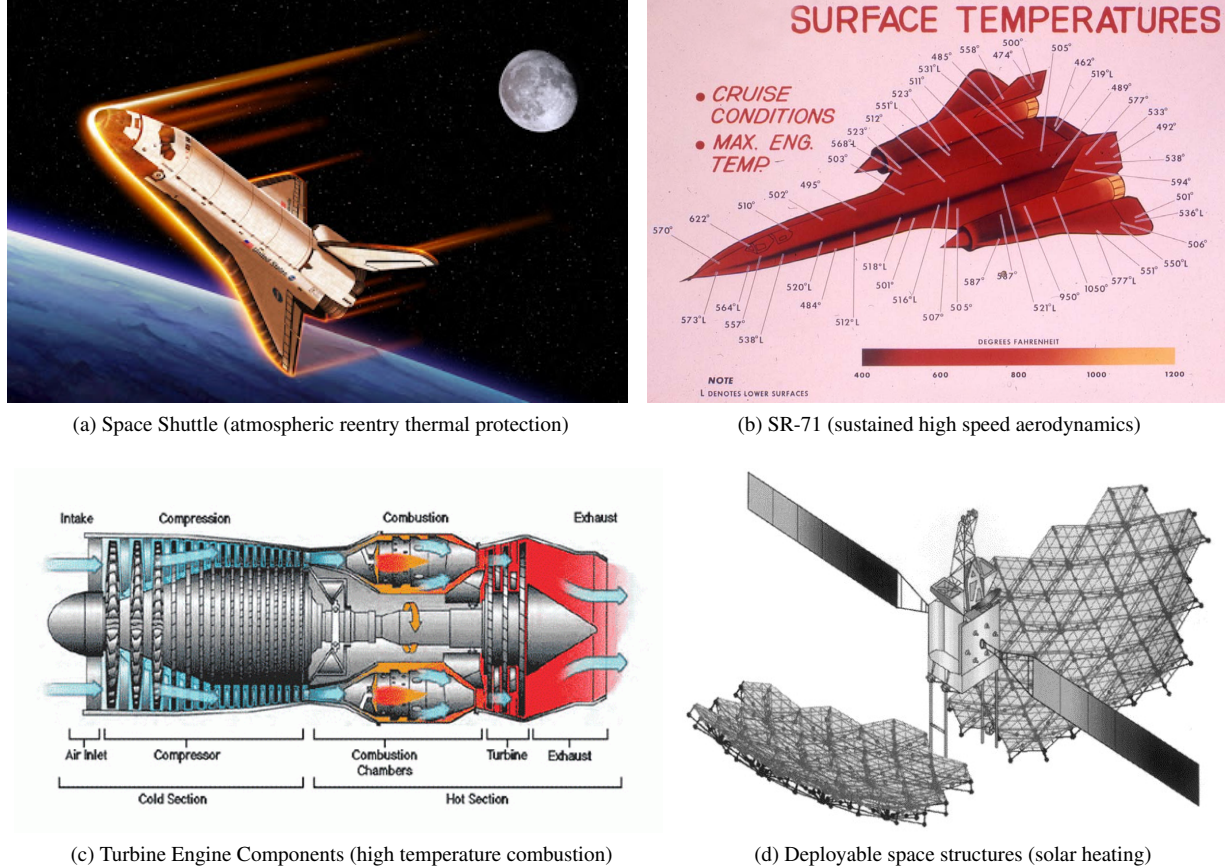


Figure 1: Historical applications in aerospace thermal structures: (a) Space shuttle reentry thermal protection structure, (b) SR-71 Blackbird aerodynamic heating environment, (c) gas turbine engine combustion and exhaust components, and (d) deployable space structures subject to radiative heating/cooling.

Thornton [1] also covers two additional topics that are especially important to modern thermal structures problems and only became possible with improvements in computational capacity. The first, geometric nonlinearity in thermal structures, is addressed with the derivation and presentation of approximate solutions to large displacement beam and shells structures. The second, and perhaps most important topic to all modern day structural analysis, is the introduction of discretized numerical analysis methods, including the finite element method (FEM). A concise discussion of the finite element formulation for quasi-steady (or weakly/sequentially coupled) thermal-structural analysis, including conduction, free convection, radiation, and linear elasticity, is given along with early applications including built-up plate and frame structures.

Advances in finite element analysis techniques gradually increased its acceptance in the thermal structures community. In recent years, capabilities for multiphysics thermal-structural *analysis*, including chained analysis and mixed-element formulations, have been well matured in commercial finite element programs such as Abaqus, ANSYS, and

Nastran. In addition, renewed interest in hypersonic flight platforms have driven new developments in thermal structures related to aerothermoelasticity and fluid-structure interaction [4] where the prediction of the elevated temperature environment itself is more challenging than legacy applications.

The introduction of finite element analysis to thermal structures also enabled the application of automated design and optimization methods practiced by the structural and multidisciplinary design optimization (MDO) community. Early works in the structural synthesis of thermal structures include an optimality criteria method for minimum-mass problems with temperature constraints [5], a fully stressed design (FSD) technique for minimum-mass sizing of thermoelastic structures [6], and approximation methods for the combined thermal-structural problem [7, 8]. More recently, improved sensitivity analysis formulations have been developed [9, 10], design-oriented thermostructural analysis frameworks for sizing and shape optimization problems have been demonstrated [11, 12], and limited applications are found in topology optimization primarily for thermal micro-mechanical actuation (as discussed in Section (3)). It is important to note that to date the majority of thermoelastic optimization has been only academic work. While some commercial structural optimization software does have the capability to solve simple linear steady-state thermal-structures problems, their automated design capabilities generally lag far behind those for analysis.

In conclusion, a review of the literature regarding the *design* of thermal structures for elevated temperature applications (dating back to the 1950s) yields two basic design rules: (1) minimize temperatures and gradients and (2) accommodate thermal expansion. Related to the second rule, it is often evident that allowing even small levels of expansion can altogether eliminate the most damaging thermoelastic effects [13]. The application of this rule is relatively commonplace, with the placement of expansion joints in concrete structures such as bridges and sliding attachments for copper plumbing in addition to aerospace structures subjected to more severe environments. However, one application where these basic rules cannot be readily applied is in the area of embedded engine integration for modern low observable military aircraft. In this case, the configuration-level design requirements necessary to evade enemy detection supersede the conventional thermal structures design wisdom.

## 1.4 Engine Exhaust-Washed Structures

To meet the growing demands for increased mission capability, combat survivability, and versatility of aerospace systems, future military aircraft will continue to rely on low observable technology. A critical component of this technology is embedded engine integration, as seen on the current B-2 Spirit stealth bomber and the Efficient Supersonic Air Vehicle (ESAV) concept shown in Figure 2. This configuration, in which engines are buried inside the aircraft, allows for a smooth outer mold line (OML), reduced exhaust noise, and cooler exhaust gases, which all reduce the vehicle's observability by decreasing radar, acoustic, and infrared detectability [14]. In addition, by utilizing a ducted exhaust system to pass exhaust gases to the rear of the aircraft, direct line of sight into hot engine components is

prevented, denying the enemy a vulnerable infrared target. This is demonstrated in Figure 3 with a simplified notional cross-section of an embedded engine configuration with ducted exhaust. While such a configuration affords tremendous tactical capabilities, it also comes with increased structural design complexity. In a legacy aircraft, where engines are located either under the wings or in the aft fuselage, high temperature exhaust gases are expelled directly into the airstream. In the case of embedded engines, the hot exhaust creates an extreme thermal-structural design environment as it is ducted to the rear of the aircraft. In this environment damaging effects of elevated temperatures including excessive deformations, thermal stresses, thermal buckling, and creep may occur.

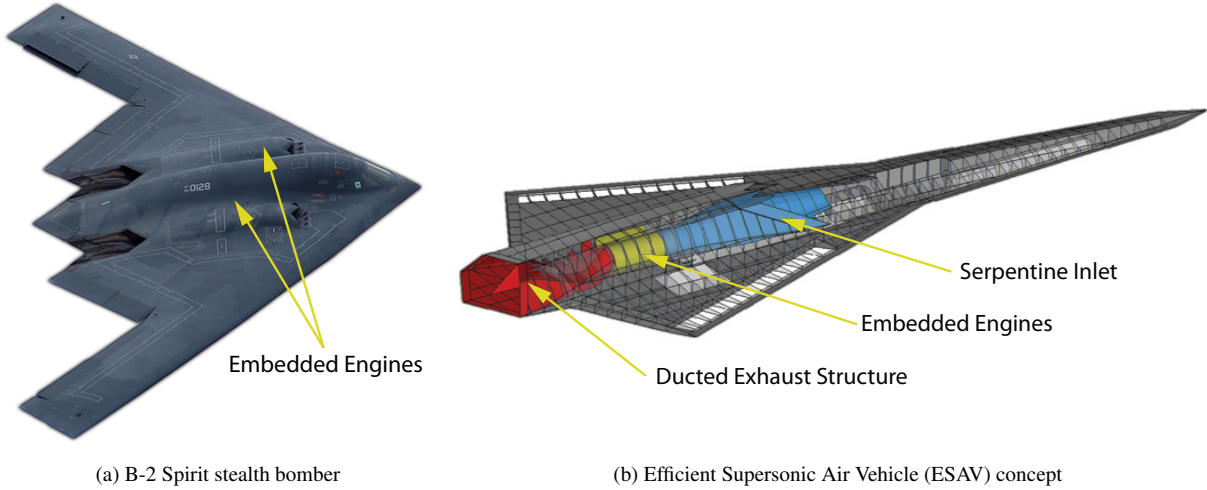


Figure 2: Military aircraft featuring embedded engine configurations and ducted exhaust.

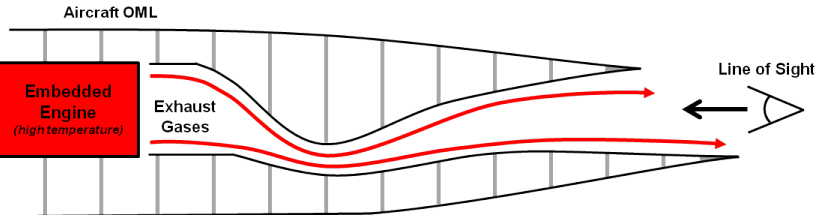


Figure 3: Cross-section of a notional embedded engine configuration showing ducted exhaust path.

The structural components located aft of the engines on an embedded engine aircraft that make up the ducted exhaust path are known as *engine exhaust-washed structures* (EEWS) [15]. In particular, exhaust-washed structures include the ducted nozzle (internal to the aircraft), the aft-deck (exhaust-washed regions on the exterior of the vehicle), and adjoining substructures. These components are subjected to a multidisciplinary environment where both thermal and structural loading produce a combined response. Thermal loads include transient elevated temperature from the exhaust flow that may be in excess of 1000°F and additional aerodynamic effects, both of which are driven largely by the aircraft's mission envelope and operating environment. The temperature loading is combined with pressure loading from the exhaust flow, mechanical loading reacted from adjoining airframe structure, and wide-band acoustic

loading. In this document we restrict our consideration primarily to loading of thermal origin.

One of the primary challenges associated with the design of the EEWs is the dominance of low observability design criteria. In a typical configuration, like that shown in Figure 4, the geometric shape of the exhaust flow path is fixed by propulsion system efficiency and low observability design criteria. In addition, all components must be smoothly integrated within the aircraft's OML. This places strict geometric shape and fixivity on structural components that are subject to elevated temperatures. Undoubtedly then, these components are subject to restrained expansion and are susceptible to thermal buckling and thermal stresses. These problems were observed on an exhaust-washed structure on the B-2 bomber known as the aft-deck. In this case, thermal stresses produced cracking and failure in the aft-deck within only a small percentage of its intended life, necessitating costly replacement and retrofitting [16].

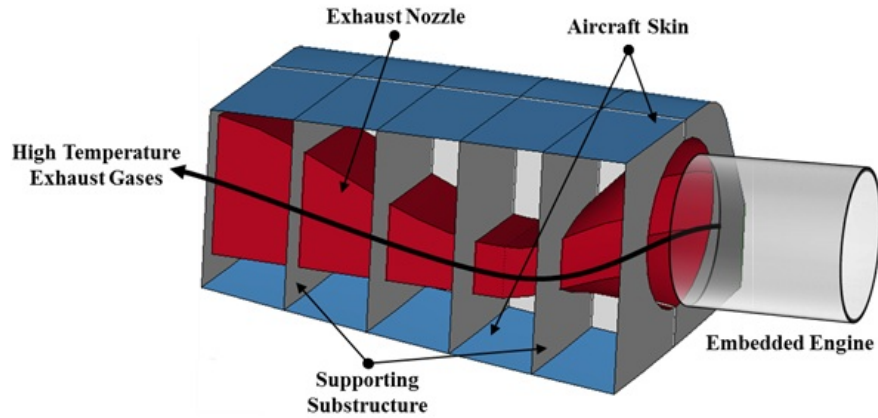


Figure 4: Conceptual engine exhaust-washed structure (EEWS) configuration located aft of embedded engines on a low observable aircraft and its primary components.

Since future embedded engine concepts share similar configurations to the B-2, it can be expected they will face similar challenges, which are also common to hypersonic flight thermal protection applications. In all cases, structural designers must accommodate thermal expansion effects to prevent excessive thermal stresses and also prevent excessive thermal loads from being transferred to surrounding structures. In theory, these types of design challenges are particularly well addressed using multidisciplinary design optimization techniques, which can simultaneously manage multiple competing responses and arrive at a suitable configuration [17]. In the following section, we highlight some of the evident issues related to the application of design optimization to practical thermoelastic design cases such as EEWs systems.

## 1.5 Technical Challenges for Thermoelastic Optimization

The standard process for a design optimization problem is given in Figure 5. The process begins with an initial design configuration, an objective function to minimize, and a set of constraints that must be satisfied. The objective function

and constraints are evaluated using a suite of analysis tools, including for example finite element analysis in the case of structural optimization. Sensitivity information regarding the objective and constraints are utilized by a numerical optimization algorithm to propose a new design. This process repeats in an iterative fashion, sometimes using a so-called approximate problem for increased efficiency, until convergence is observed in the objective function.

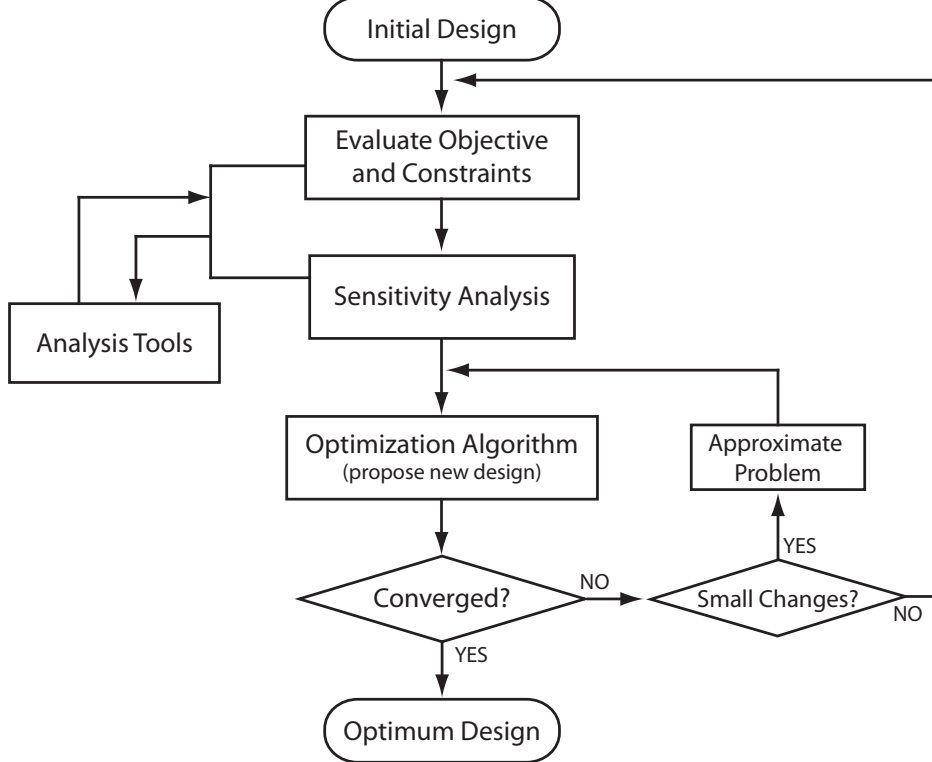


Figure 5: Standard design optimization process.

There exist several technical challenges and important considerations for the application of such a design process to the thermoelastic problems of interest in this document. The first of these issues is related to the design dependency of thermal loading that exists in both the thermal and structural domains of the thermoelastic problem. That is, any design modification of the current design, for example increasing structural thickness or changing structural topology, changes the thermal load on the structure. This modification influences the heat transfer mechanisms that determine temperature distributions in a component and also modifies the magnitude of thermal load (resulting from the temperature distributions) in the structural domain. In Figure 5, this dependency must be captured in the sensitivity analysis used to guide the design process. Another issue is the transient nature of the potential loading on an EEWS system. Transient responses in optimization are difficult to handle because of need to enforce design criteria at all points throughout a temporal response. Unless the primary mechanisms in the transient response can be captured using a reduced number of responses, a large number of constraints are required by the process in Figure 5. This results in a massive design problem that may not always be tractable with available computational resources and time require-

ments. Finally, the accuracy of boundary conditions in a thermoelastic system are extremely important. In Figure 5, it is desirable to utilize the most efficient analysis models and tools available to reduce computational time. However, to properly capture the true response of a thermoelastic structure, a design model often must include large portions of adjoining structures around a particular component of interest, which increases the size of the simulation model. In the following section, some characteristic responses of thermal structures are presented to demonstrate some of these challenges and to motivate the application of MDO and topology optimization methods to exhaust-washed structures.

## 2 Characteristic Responses of Thermal Structures

In this chapter, the fundamental thermal and structural responses that are characteristic of engine exhaust-washed structure design problems are presented using finite element analysis results. These fundamental responses provide the motivation for the application of multidisciplinary topology optimization to solve the design challenges related to engine exhaust-washed structures. Both the physical behavior of the systems that must be addressed and the several of the technical challenges that must be accommodated in advanced design are demonstrated.

### 2.1 Exhaust Structure Thermoelastic Response

The thermoelastic response of an EEWs system like that shown previously in Figure 4 involves the coupled physics of heat transfer and structural mechanics. In each discipline, loading and boundary conditions are governed by the actual vehicle configuration and transient mission envelope. While a variety of exhaust structure configurations are possible, they share characteristic responses of interest. To demonstrate these responses, an exhaust-washed structure configuration belonging to an Efficient Supersonic Air Vehicle (ESAV) conceptual design, shown in Figure 2b, is considered here.

A typical mission for this type of aircraft includes take-off, supersonic cruise, munitions deployment/combat, and landing as shown in Figure 6 [18]. Supersonic cruise ranges from Mach 2.0-2.4, which can lead to temperatures due to aerodynamic heating effects of approximately 300°F on external skin panels. In addition, exhaust temperatures from advanced gas turbine engines are approximately 900-1000°F during cruise and exceed 1400°F during high power take-off and combat phases.

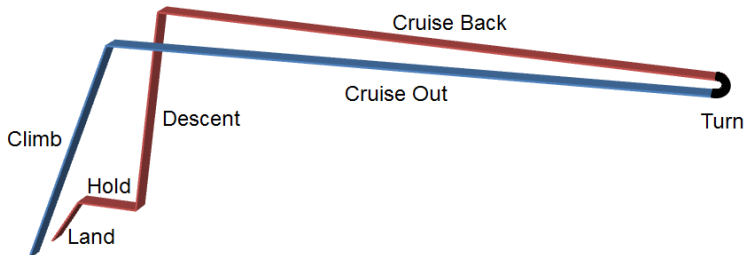


Figure 6: Typical mission profile for an ESAV aircraft [18].

Figure 7 shows the finite element discretization of the EEWs system. Details of loading, boundary conditions, and element selection are given in proceeding sections related to heat transfer and structural analysis. Approximate geometry, dimensions, and thicknesses are extracted from an ESAV aircraft model that was originally sized primarily for aeroelastic design criteria including flutter and aerodynamic flight loads. In this configuration, high temperature composite materials are utilized. The aircraft skins and substructure (green/purple/blue shell elements) are constructed from honeycomb sandwich panels consisting of a 0.5 inch titanium honeycomb core and 0.08 inch

graphite-bismaleimide (Gr/BMI) facesheets in a symmetric layup. The nozzle structure (red shell elements) exposed directly to the exhaust gases is CMC material of 0.4 inch thickness and the entire system is assembled using composite pi joints (thick black 1-D elements) common to modern composite airframes [19]. In addition, to reduce the effects of radiation from the hot nozzle to surrounding structure, a 0.375 inch layer of aerogel insulation (yellow solid elements) wraps the exterior surface of the nozzle.

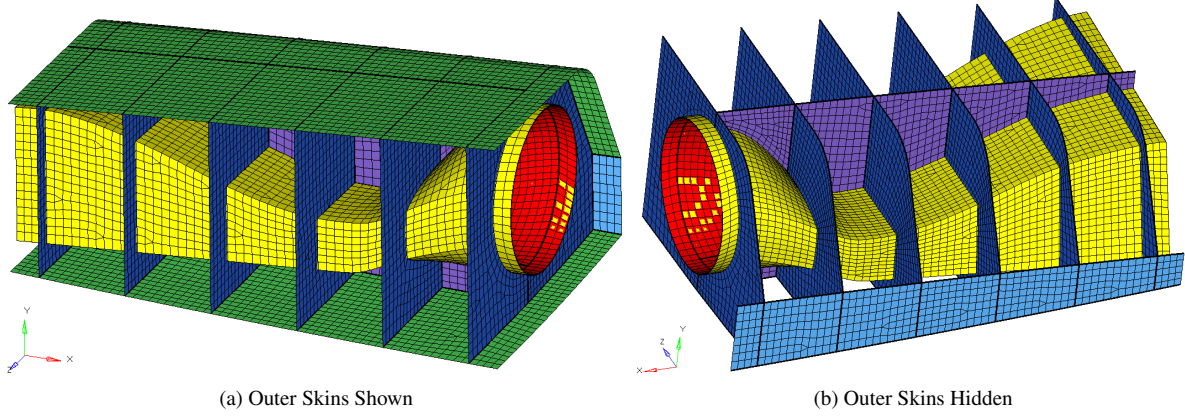


Figure 7: Finite element discretization of EEWS system with outer skins (a) shown and (b) hidden to show internal structure.

Primary loading on the structure includes the temperatures resulting from the thermal environment and pressure loading from the exhaust flow. Heat transfer processes in the structure include transient conduction, radiation both within internal enclosures and externally from the skins to the environment, convective transfer on the skins from aerodynamic flow, and convective ventilation within compartments inside the structure. In addition, acoustic and flight load contributions are present in the combined environment, but are neglected in this analysis. It is also important to note that in reality the EEWS is structurally integrated in the aircraft. This is reflected in the local analysis model's structural boundaries due to the significance of structural fixity on thermoelastic responses.

### 2.1.1 Thermal-Structural Analysis Technique

A sequentially coupled analysis technique is employed to study the thermoelastic response of the EEWS. In this technique, first a heat transfer analysis (steady-state or transient) analysis is performed to determine nodal temperature distributions throughout the model. These distributions are then mapped to the structural model where additional structural loads and boundary conditions (BCs) are applied. This loosely coupled technique is suitable because in this case the deformations predicted in the structural model do not have a significant effect on heat transfer responses. In the case of transient analysis, temperature distributions from each time-step are mapped to separate load cases in static structural analysis. Dynamic structural effects are not considered. The commercial software MD Nastran is utilized [20].

### 2.1.2 Heat Transfer Model

The thermal conditions on the EEWs model vary throughout different segments of the mission profile. Since initially it was unclear as to how quickly the EEWs system would respond to changes in thermal conditions and during which time periods critical structural responses may occur, the entire mission was analyzed. This was done using a nonlinear transient heat transfer solution in MD Nastran. The thermal effects captured in the heat transfer model include:

- high temperature exhaust gases
- aerodynamic effects on skins due to external airflow
- ventilation inside internal bays
- radiative heat loss to the surrounding environment
- radiation within internal bays/enclosures

The true heating effect from high temperature exhaust gases is a product of propulsion emissions and the thermal-fluid characteristics of the resulting exhaust plume. As an alternative to performing high fidelity engine cycle and computational fluid dynamics analysis, the effect of the exhaust gases is approximated using transient temperature boundary conditions applied to the finite element nodes in the nozzle structure. The specified temperatures are based on expected exhaust temperature at different levels of engine power, which vary in between mission segments. The exhaust temperature for a 350 minute mission is given in Figure 8a.

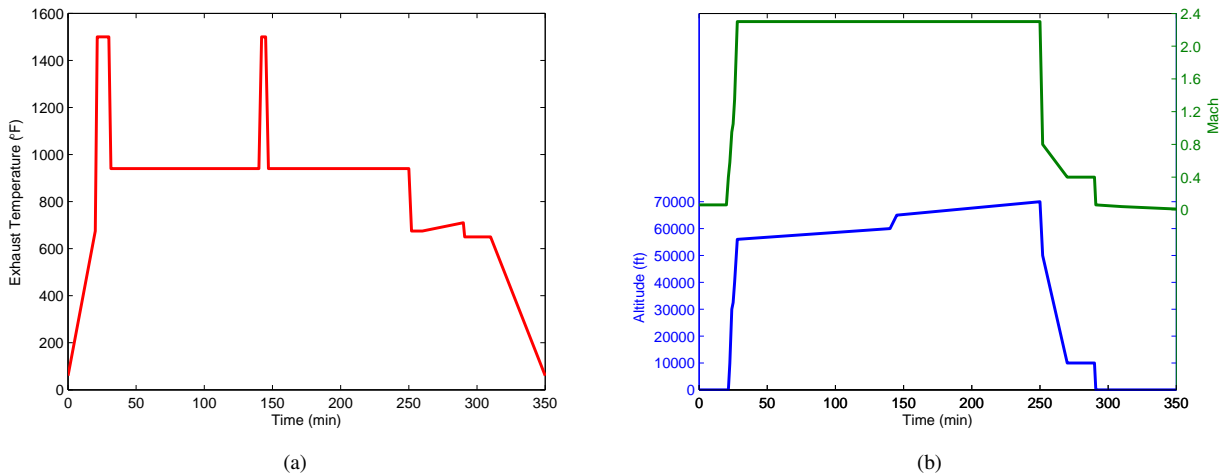


Figure 8: (a) Exhaust temperature, (b) altitude and Mach for a 350 minute ESAV mission

The effect of aerodynamic heating on skin panels, neglecting effects of localized shocks or stagnation (which are not expected in the EEWs region of the aircraft), is approximated using a convection boundary condition, with heat

flux into the surface of element  $i$  expressed as

$$q_i = h(T_{aw} - T_i) \quad (1)$$

where  $q$  is the local heat flux,  $h$  is the convection film coefficient,  $T_{aw}$  is the adiabatic wall temperature, and  $T_i$  is the temperature of element  $i$  (taken as the average of nodal values). The adiabatic wall temperature is the temperature a moving fluid across a surface obtains assuming no heat transfer into the wall. In this study, approximations for  $h$  and  $T_{aw}$ , which are typically local quantities on an aircraft, are obtained from the classical boundary layer solution to flow over a flat plate. Studies of this problem [21] indicate the adiabatic wall temperature can be obtained with good accuracy from

$$T_{aw} = T_\infty \left[ 1 + r \frac{\gamma - 1}{2} M_\infty^2 \right] \quad (2)$$

where  $\gamma$  is the ratio of fluid specific heat,  $r$  is the recovery factor, and  $T_\infty$  and  $M_\infty$  are the temperature and Mach number of the free stream flow. The recovery factor is determined from the Prandtl number for turbulent flow as  $r = Pr^{1/3}$ . In this study, constant values of  $\gamma = 1.4$  and  $Pr = 0.71$  are assumed.  $M_\infty$  is taken as the aircraft Mach and  $T_\infty$  is taken as the temperature of the standard atmosphere at a given altitude. The values of altitude and Mach are given in Figure 8b throughout the mission. The convection coefficient can be determined from the Stanton number given by

$$C_H = \frac{h}{\rho_\infty u_\infty C_p}. \quad (3)$$

Using Eckert's reference temperature method [22], the Stanton number for turbulent flow is computed from

$$C_H = \frac{0.185}{(\log_{10} Re_x^*)^{2.584}} (Pr^*)^{-2/3} \quad (4)$$

where  $Re_x^*$  and  $Pr^*$  are evaluated at the reference temperature  $T^*$ ; that is,

$$Re_x^* = \frac{\rho^* u_\infty x}{\mu^*} \quad Pr^* = \frac{\mu^* C_p^*}{k^*} \quad (5)$$

are evaluated at  $T^*$ . The reference temperature is computed as

$$T^* = T_\infty \left[ 1 + 0.032 M_\infty^2 + 0.58 (T_w/T_\infty - 1) \right] \quad (6)$$

where the wall temperature  $T_w$  is assumed to be 300°F in the model. The  $x$  station along the plate is approximated as the distance from the center of the top/bottom skin in the EWS to the leading edge of the EAV conceptual configuration. As such, different convection coefficients for the top and bottom skins are computed, but are assumed constant over the entire surface of each region. As computed from Equations (2)-(6) and data in Figure 8b, the temporal variation of

the free stream and adiabatic wall temperatures and convection coefficients for the top/bottom skins are computed and shown in Figures 9a and 9b.

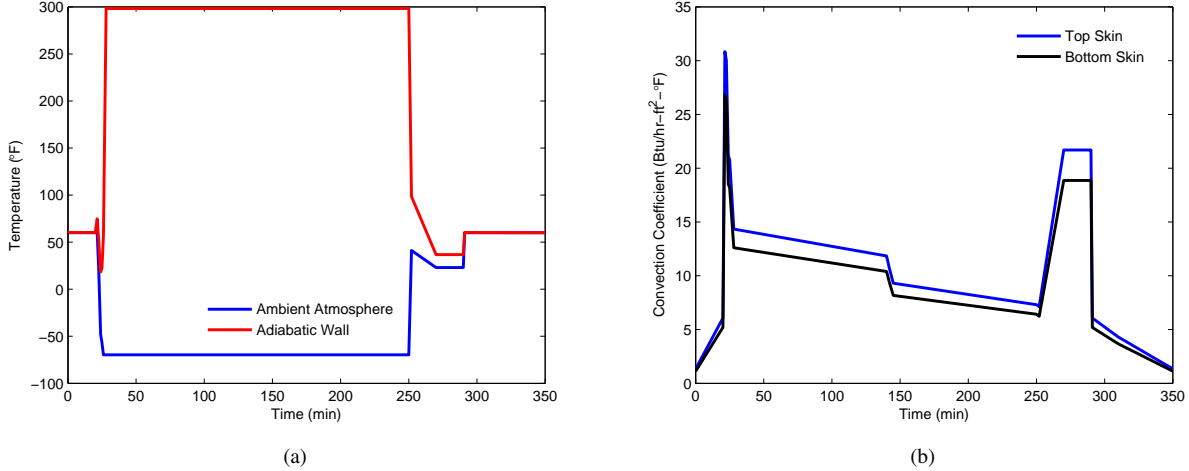


Figure 9: (a) Ambient and adiabatic wall temperatures and (b) convection coefficients for the top and bottom skin for a 350 minute ESAVE mission

The effect of ventilation on the internal bays of the structure, by using external air for cooling, is also approximated using a convection boundary condition of the form in Equation (1). In this case, the convection coefficient  $h$  is assumed to be constant throughout the mission with a value of 1.0 Btu/hr · ft<sup>2</sup> · °F and the ambient temperature for convection is again taken as the adiabatic wall temperature.

Radiative heat loss to the environment is modeled using a radiation boundary condition. This condition represents radiation exchange between a surface element  $i$  and a black body sink and is given by

$$q_i = \sigma(\varepsilon_i T_i^4 - \alpha_i T_{amb}^4) \quad (7)$$

where  $\sigma$  is Boltzmann constant,  $T_i$  is the temperature of element  $i$ ,  $T_{amb}$  is the temperature of the ambient sink, and  $\varepsilon_i$  and  $\alpha_i$  are the emissivity and absorptivity of element  $i$ , respectively. In this study, we assume that  $\varepsilon_i = \alpha_i$  for all surfaces. The ambient sink for external radiation from the top and bottom skins is assumed to be outer space at -60.0°F and earth at 60.0°F, respectively. In addition, internal radiation exchange between surfaces is included in the model as boundary conditions. View factor computations are performed internally by Nastran after specifying the appropriate radiation enclosures.

The thermal properties of the materials and surfaces for the heat transfer analysis are given in Table 1 and are assumed constant with respect to temperature. For the honeycomb panels a homogenization method was utilized to determine composite-level properties using the laminate ply and core properties. Finally, transient analysis was conducted using a time step of 10 seconds.

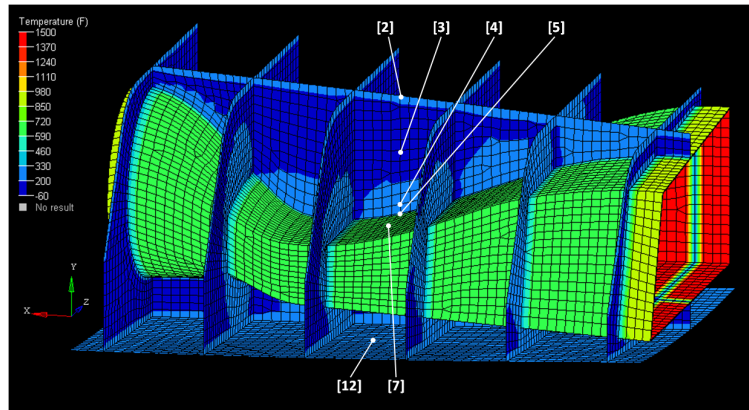
<b>CMC Material</b>		<b>Aerogel Insulation</b>		<b>Radiation Emissivity</b>	
$k$ (Btu/hr · ft · °F)	0.91	$k$ (Btu/hr · ft · °F)	0.0375	External Skins	0.70
$\rho$ (lbm/ft <sup>3</sup> )	155.5	$\rho$ (lbm/ft <sup>3</sup> )	12.5	Internal Bays	0.85
$C_p$ (Btu/lbm)	0.3	$C_p$ (Btu/lbm)	0.25	Insulation	0.20
<b>Laminate Facesheets</b>		<b>Honeycomb Core</b>			
$k_1$ (Btu/hr · ft · °F)	6.5	$k_1$ (Btu/hr · ft · °F)	0.5		
$k_2$ (Btu/hr · ft · °F)	0.5	$k_2$ (Btu/hr · ft · °F)	0.5		
$\rho$ (lbm/ft <sup>3</sup> )	88.1	$\rho$ (lbm/ft <sup>3</sup> )	9.5		
$C_p$ (Btu/lbm)	0.29	$C_p$ (Btu/lbm)	0.25		

Table 1: Material and surface properties for thermal analysis of the EEWs system.

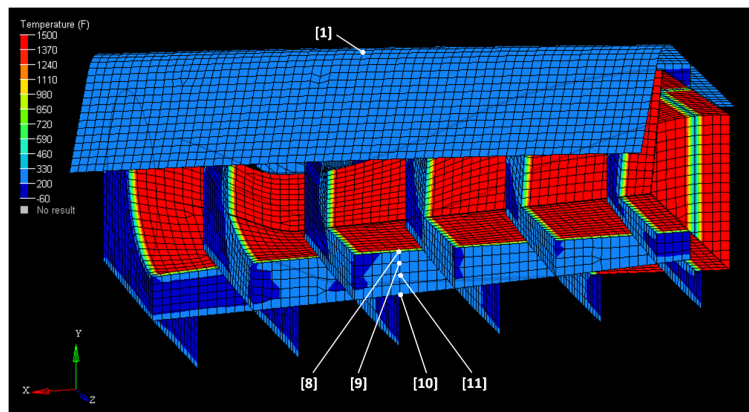
### 2.1.3 Heat Transfer Results

The temperature distribution in the EEWs system at 30 minutes into transient analysis is given in Figures 10a-c. Note that different portions of the structure are hidden in different sub-figures. At 30 minutes, which corresponds to a time frame of high exhaust temperature during aircraft climb, the spatial distribution of temperature is characterized by extremely high temperatures at the exhaust-washed nozzle surface that are dissipated outward into the attached substructures. The effects of convection and radiation sufficiently cool the substructure and aircraft skins such that temperature levels do not exceed material allowables. We also note that due to the relatively high conductivity of the composite substructure and amount of convective cooling, spatial temperature distributions within individual panels/plates of the built up system are not severe. This distribution of temperature is representative of large portions of the transient analysis time history, with the magnitude of temperatures scaled proportional to the exhaust temperature.

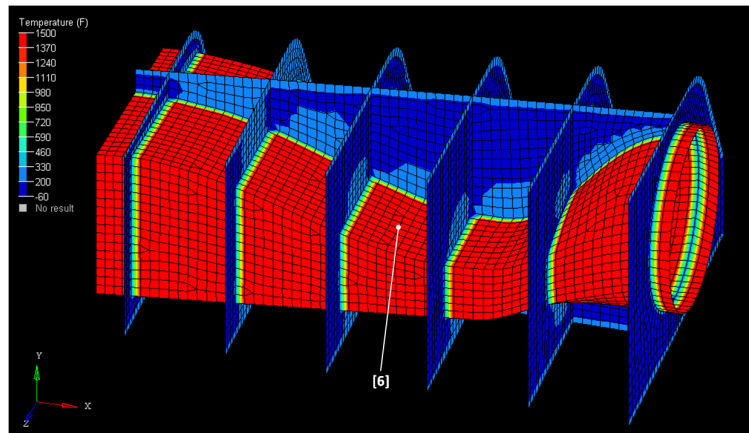
Several nodes are also indicated in Figures 10a-c at which transient temperatures are monitored. These locations are described in Figure 10d. The transient temperature history at these nodes is plotted in Figure 11 to demonstrate the variation of temperature in the structure throughout the entire analysis. In this figure, we note that the structure responds relatively quickly to changes in thermal conditions. This indicates that in future investigations, the temperature distributions at different parts of transient analysis may be captured with sufficient accuracy using steady-state analysis. If this is possible, the application of design optimization methods becomes much more feasible.



(a) Top Skin Hidden, Insulation Shown



(b) Bottom Skin Hidden, Insulation Hidden

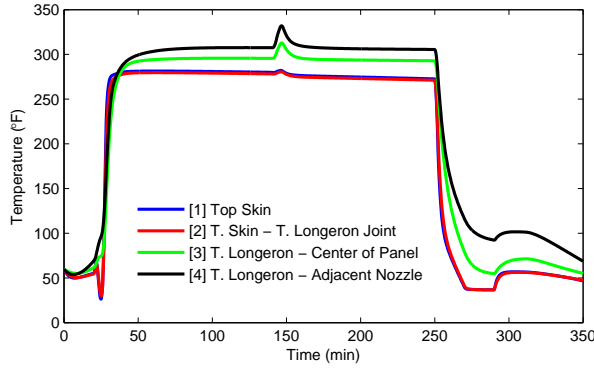


(c) Skins and Insulation Hidden

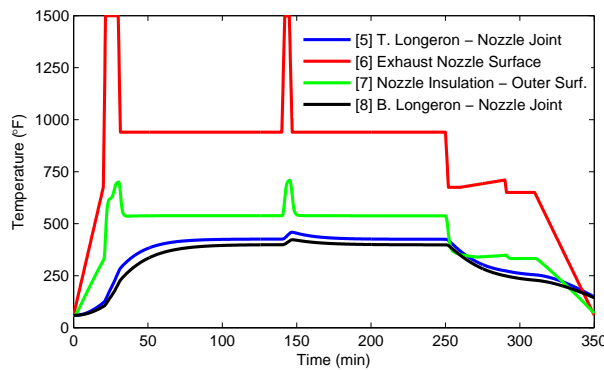
- |   |  |
|---|--|
| [1] Top Skin                            | [7] Outer Surface of Nozzle Insulation     |
| [2] Top Skin - Top Longeron Joint       | [8] Exhaust Nozzle - Bottom Longeron Joint |
| [3] Top Longeron - Center of Panel      | [9] Bottom Longeron - Adjacent Nozzle      |
| [4] Top Longeron - Adjacent Nozzle      | [10] Bottom Longeron - Center of Panel     |
| [5] Exhaust Nozzle - Top Longeron Joint | [11] Bottom Skin - Bottom Longeron Joint   |
| [6] Exhaust Nozzle Surface              | [12] Bottom Skin                           |

(d) Description of nodes where transient temperatures recorded (see Figure 11)

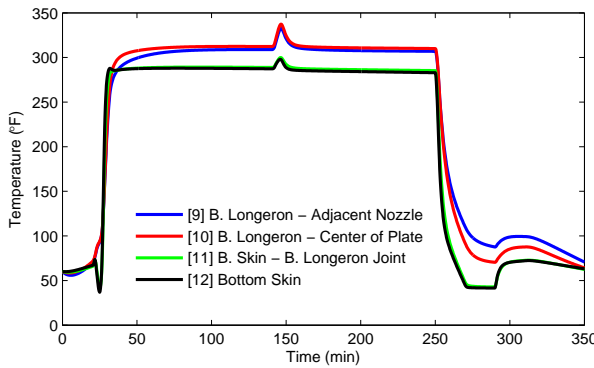
Figure 10: Temperature distribution in EEWS at 30 minutes in transient analysis.



(a)



(b)



(c)

Figure 11: Transient temperatures at nodes denoted in Figure 10: (a) top regions of model, (b) regions near exhaust nozzle, and (c) bottom regions of model.

#### 2.1.4 Structural Model

The primary loading and boundary condition considerations for the EEWS structural analysis are:

- Temperature loading from heat transfer analysis
- Pressure loads from exhaust flow

- Stiffness of adjoining structures

The nodal temperature distribution from the heat transfer analysis is mapped onto the structural model to contribute thermal loads. Quasi-steady behavior is assumed such that the distribution for each time step from heat transfer results is utilized in a separate static load case. In addition, pressure loads are applied normal to the inside of the exhaust nozzle surface to represent the forces due to the exhaust flow. The applied pressure load has both spatial and temporal variation. Spatially, the pressure decays linearly along the length of the nozzle from a high pressure value (engine exit) to near zero (atmospheric conditions). The temporal variation of pressure is related to engine power along the mission profile and takes a maximum value at the front of the nozzle of 30 psi during periods of high power, which is also accompanied by high temperature exhaust.

In thermoelasticity, boundary representation is important because it determines the amount of thermal expansion that is externally restrained. In this model, the primary regions of interest include the exhaust nozzle surface and substructures to which it is directly attached. To better capture the appropriate level of internal restraint on these areas, additional surrounding structure, such as the outer aircraft skins, is modeled. Fixed boundaries are applied to this additional structure, which is further from areas of interest. The structural boundary conditions for the model are shown in Figure 12 with blue denoting a symmetry condition and black denoting a clamped condition (all degrees of freedom fixed). An alternative would be to perform sub-component analysis to approximate the stiffness of the adjoining structure and apply elastic spring elements to structures of interest in the model. This alternative was investigated on reduced complexity models, but proved to give similar results.

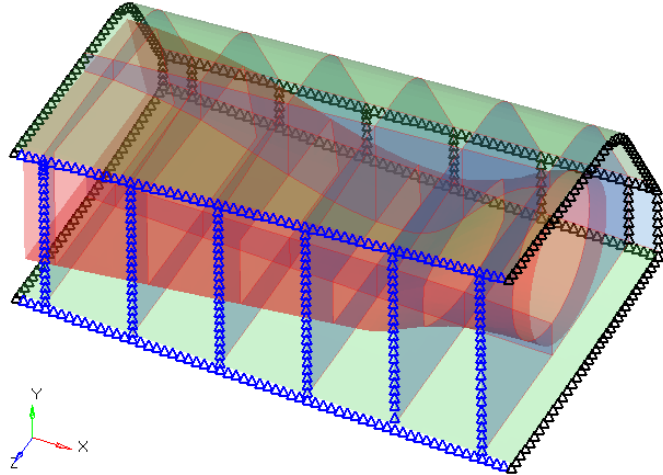


Figure 12: Boundary conditions on the EEWs structural model with blue denoting symmetry over the x-y plane and black representing a fixed condition in all nodal degrees of freedom.

In thermal stress analysis, the effect of temperature dependent material properties should be considered. In this study, rather than accounting for dependence at every temperature level, constant material properties, taken at the elevated temperature a particular material is at during the majority of heat transfer analysis, are utilized. This was

done due to the lack of a complete set of temperature dependent properties for all materials and the observation from Figures 10 and 11 that large regions of steady-state behavior exist with relatively uniform spatial gradients in the transient heat transfer results. The structural material properties and their reference temperatures are given in Table 2.

<b>CMC Material (1500°F)</b>		<b>Composite Pi-Joint</b>	
$E$ ( $10^6$ psi)	7.25	$E$ ( $10^6$ psi)	7.4
$v$	0.1	$G$ ( $10^6$ psi)	6.19
$\alpha$ ( $10^{-6}/^{\circ}\text{F}$ )	2.5	$\alpha$ ( $10^{-6}/^{\circ}\text{F}$ )	0.49
<b>Laminate Facesheets (300°F)</b>			<b>Honeycomb Core (300°F)</b>
$E_1$ ( $10^6$ psi)	23.5	$E_1$ ( $10^6$ psi)	N/A
$E_2$ ( $10^6$ psi)	1.5	$E_2$ ( $10^6$ psi)	N/A
$v_{12}$ (lbm/ft <sup>3</sup> )	0.38	$v_{12}$ (lbm/ft <sup>3</sup> )	0.3
$G_{12}$ ( $10^6$ psi)	0.37	$G_{12}$ ( $10^6$ psi)	N/A
$G_{1Z}, G_{2Z}$ ( $10^6$ psi)	0.247	$G_{1Z}, G_{2Z}$ ( $10^6$ psi)	0.0775
$\alpha_1$ ( $10^{-6}/^{\circ}\text{F}$ )	-0.9	$\alpha_1$ ( $10^{-6}/^{\circ}\text{F}$ )	0.1
$\alpha_2$ ( $10^{-6}/^{\circ}\text{F}$ )	16.7	$\alpha_2$ ( $10^{-6}/^{\circ}\text{F}$ )	0.1

Table 2: Structural material properties for the EEWs system.

Finally, since the potential for large displacements and follower forces does exist, a nonlinear solution sequence in MD Nastran is utilized to ensure that effects of geometric nonlinearity is captured. This solution utilizes incremental load stepping and includes differential terms in the stiffness matrix. Throughout analysis, no issues related to convergence in the solution sequence was observed.

### 2.1.5 Structural Results

The displacement and stress responses of the EEWs structure for the loading at 30 minutes into the mission (the temperatures of which where shown previously in Figure 10) are shown in Figure 13. Note that in Figures 13a and 13b the deformation has been magnified by a factor of 10 to more clearly demonstrate the displacement behavior. From Figure 13a it is evident that the regions of greatest overall displacement occur within the exhaust-washed nozzle structure, which we recall has attained a temperature of approximately 1500°F at the time shown. This produces a case where the thermal expansion of the inner nozzle structure is restrained by the cooler surrounding structures. This is demonstrated in Figure 13b, which shows the x-direction displacement in the structure. We see the magnitude of growth of the inner exhaust structure is much more significant when compared to adjoining substructures and the aircraft skins. The effect of this restrained expansion is the development of thermal stresses, which are shown in Figures 13c and 13d. In these figures, the outer skins have been hidden due to their relatively benign stress levels compared to the nozzle and substructure regions. In addition, stress values shown are those computed for the equivalent shell elements rather than individual composite layers that make up some of the structure. This is done to simply gain an appreciation for the basic structural response and overall stress levels without introducing the complexity of composite laminate failure criteria.

The areas of greatest von Mises stress in the model are observed in corners of the substructure components where they are attached to the nozzle. While these locations are likely the those of greatest stress in the substructure due to the bending deformation created by the expanding nozzle, the actual values shown in Figures 13c and 13d are only an approximation due to idealizations in the finite element model. The exact geometry of the composite pi-joints and fillets in these regions is not reflected in the shell element representation. Nonetheless, overall stress values away from these locations are more indicative of the true scenario. In fact, these stresses reach maximum values of approximately 35-40 ksi throughout the substructure components, which is within the design limits of the Gr/BMI material system [23].

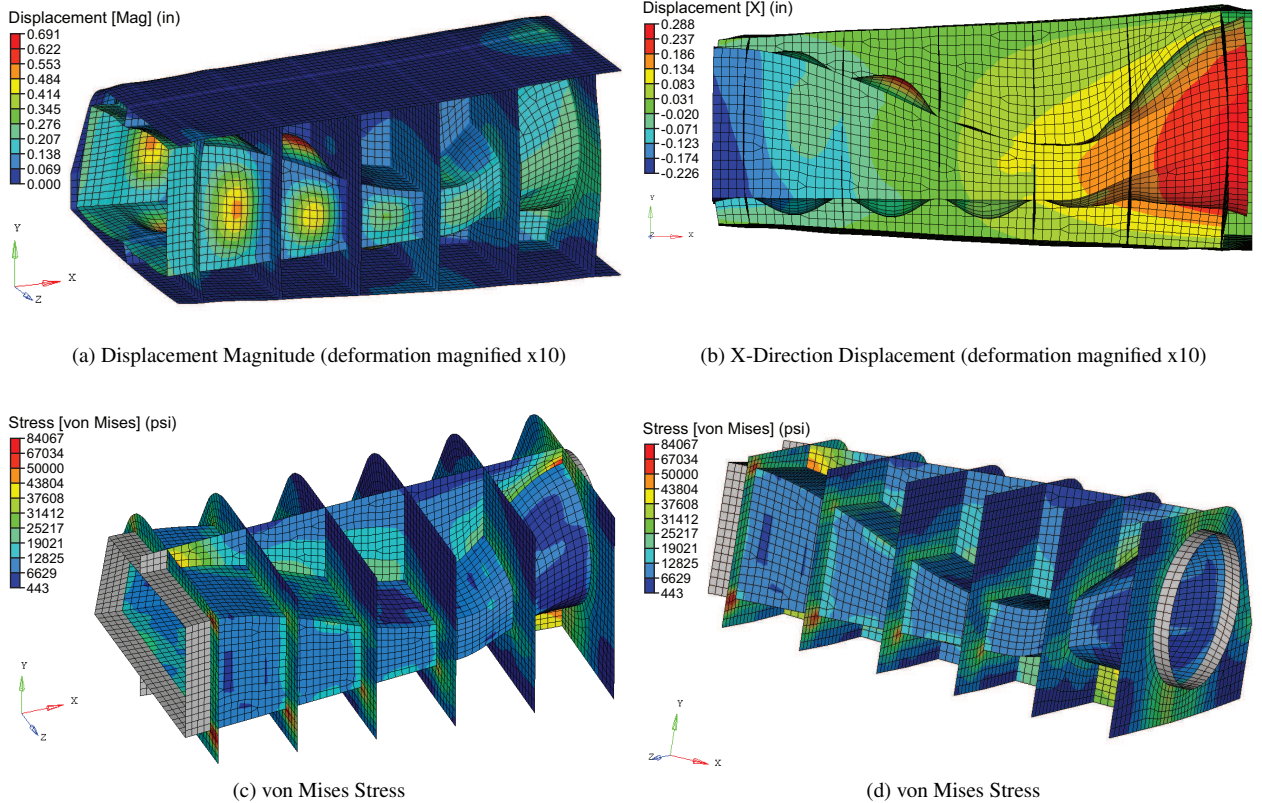


Figure 13: Displacement and stress distributions in EEWS system for loading at 30 minutes in the mission. Outer skins hidden in stress plots due to relatively benign stress levels.

The von Mises stresses in the nozzle structure reach maximum values of approximately 28 ksi, which far exceeds the proportional limit stress of roughly 10 ksi at temperature [24], which is commonly used as a design metric for CMC materials [25]. The origin of these excessive stresses is demonstrated in Figure 14, in which the contour indicates the first (max) principle stress in the isolated nozzle structure. Here we see the nozzle structure may be viewed as an assembly of individual panels separated by the supporting substructures to which they are attached. We see that the restraint placed on the nozzle structural panels by the surrounding substructures leads to out-of-plane deformation. In

some panels this deformation is nearly 0.7 inches across approximately a 30 inch span. This is similar behavior to the response of the previously mentioned exhaust-washed structure found on the B-2 Spirit stealth bomber known as the aft-deck [15]. In that instance, excessive out-of-plane deformation of thin exhaust-washed panels formed cracks that eventually caused in service structural failures.

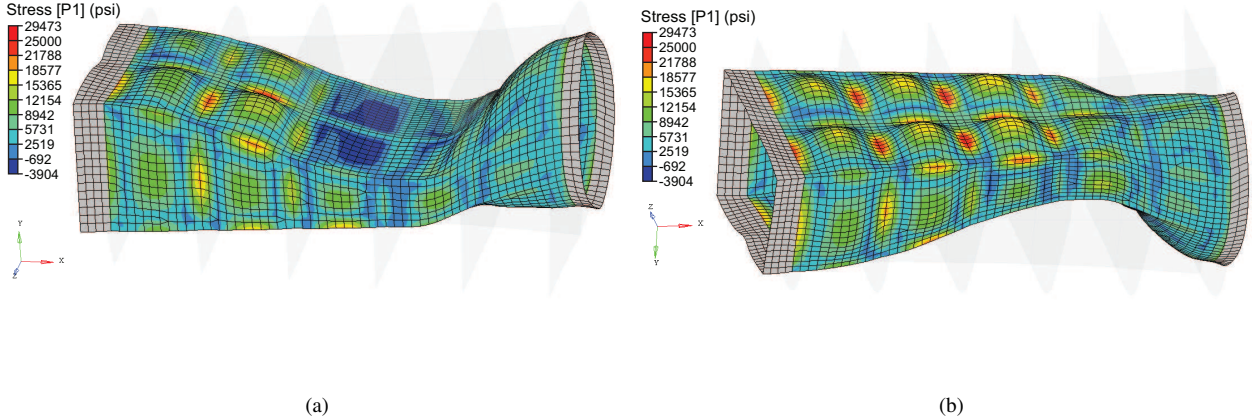


Figure 14: First principle stress (maximum of either inner or outer shell) for nozzle structure in EEWs system. Note deformation is magnified 10 times.

The stress response generated by the out-of-plane displacement of the nozzle structure is characterized predominately by bending stresses. In each panel/shell, stresses are greatest along the edges at connections to the substructure, which yields a stress profile similar to a beam or plate undergoing cylindrical bending. The slope of deformation along these regions also indicates that the substructure and adjacent plate boundaries do not create a fully clamped condition, but rather that of finite stiffness in both the in-plane direction and rotation over the edges. To more clearly illustrate the stress distribution in some of the panels, Figure 15a shows principle stress plotted with respect to a section line across the center of each panel as indicated in Figure 15b.

We observe again in each panel a stress response that is consistent with a plate or shell undergoing bending. In each case, the greatest stresses occur along panel boundaries on the side opposite the out-of-plane deformation. From these observations, it may be presumed that some of the mechanisms for reducing the stress levels in a panel that is bowing out-of-plane may be effective in the design of built-up EEWs structures. One way to accomplish this stress reduction is to somehow reduce the magnitude of the out-of-plane deformation response. In fact, this idea will be explored in later sections of this document.

Finally, the stresses in various panels in the EEWs system, in addition to its first linear buckling factor, are plotted as a function of time in Figure 16a. The locations for the panels in Figure 16a are given in Figure 16b. From these results, it is clear that the most severe thermoelastic responses in each part of the built-up system coincide with periods of highest temperature. This is intuitive because the greatest temperatures naturally lead to the greatest magnitude

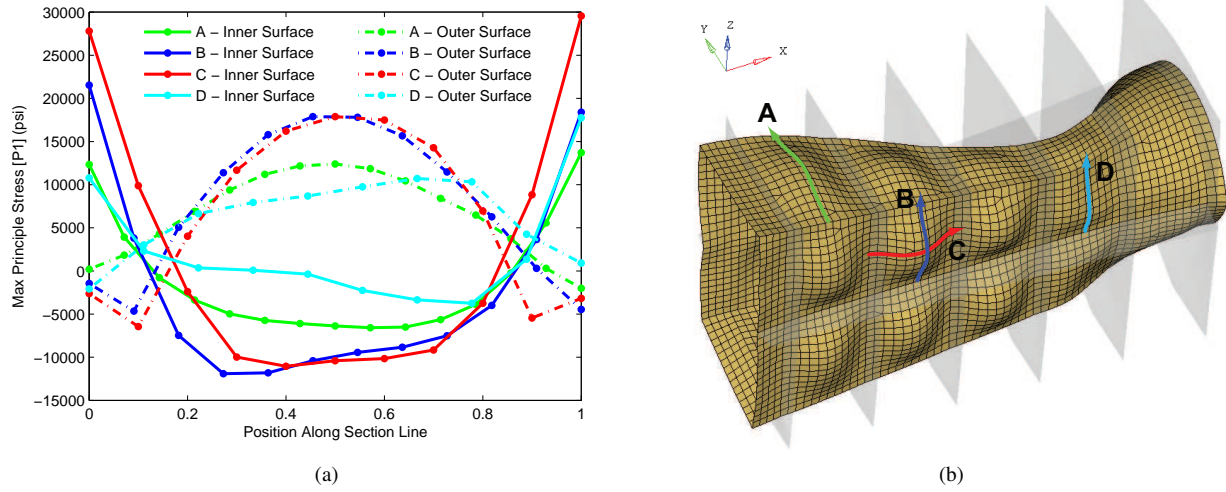


Figure 15: (a) Maximum principle stresses in nozzle structure along section lines shown in (b).

of thermal expansion. We note that similar to the transient temperature results in Figure 11, the responses reach a steady-state relatively quickly after a change in overall temperature state. This is due in large part to the relatively high diffusion properties of the composite materials being utilized. This also indicates that in future studies, with the proper application of loading and boundary conditions, the most severe thermal environment experienced throughout the transient mission may be readily captured using only steady-state heat transfer analysis. In addition, we note from Figure 16a that the linear buckling load factor dips below 1.0 during periods of high nozzle temperature. This indicates that buckling is predicted in the structure; however, the accuracy of linear predictions in this environment is subject to question for cases of restrained thermal expansion. During further investigations using a nonlinear buckling analysis procedure outlined by Cook et al [26], no buckling is observed when the effects of geometric nonlinearity are approximated in the linear buckling analysis. This assertion coincides with the results from geometric nonlinear analysis used to predict stresses here. As the structure heats up, smooth equilibrium paths are observed and bifurcation or snap-through is not evident, which would likely be uncovered in the nonlinear solution process.

### 2.1.6 Summary

In this section, the heat transfer and structural responses of a conceptual EEWs configuration have been investigated. Some important conclusions regarding the basic thermoelastic response of this system are as follows:

- The most severe structural responses coincide with periods of highest exhaust nozzle temperature. During other time periods, stress levels are generally proportional to nozzle temperature levels.
- The EEWs system responds relatively quickly to temporal changes in thermal conditions. This indicates that the important structural responses may be captured using temperature predictions from only steady-state heat

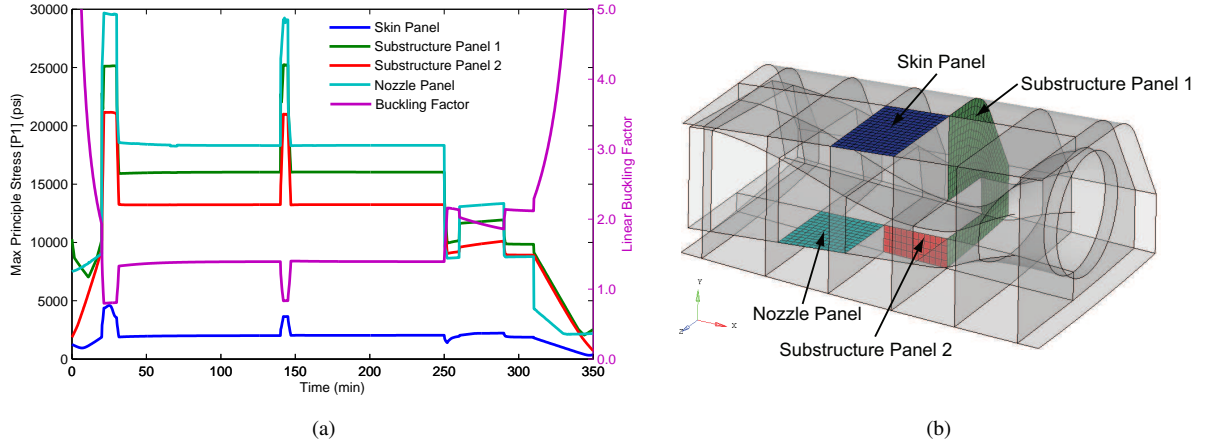


Figure 16: (a) Maximum principle stress in panels in different regions of EEWs structure as a function of time. (b) Location of panels for query.

transfer.

- Critical stresses in the exhaust-washed nozzle structure occur near its attachment to substructure and are due to the out-of-plane deformation of the thin shell-like components.

Finally, the nonlinear analysis techniques employed in this section are not desirable when attempting to design structures. Thus, with the findings in mind regarding the behavior of the entire built-up exhaust-washed structure, attention is now focused on the basic physics of the thin shell-like structures from which it is assembled and the necessary analysis capabilities that are required to accurately study them.

## 2.2 Significance of Geometric Nonlinearity

There are two types of nonlinearity involved in structural analysis: (1) material and (2) geometric. The effects of material nonlinearity, which occurs when a linear relationship does not exist between stress and strain, are readily realized in cases of thermal loading. First, the properties of most engineering materials are a function of temperature. However, this behavior is easily accommodated in structural analysis by taking material properties at the appropriate temperature. Other primary sources of material nonlinearity, including yielding and creep effects, are outside the scope of the proposed work, but do play an important role in some thermal structures design studies.

Geometric nonlinearity is generally related to large deformations, follower forces, and contact problems. In fact, geometric nonlinearity can play a significant role in the thermoelastic response of the types of structures considered in this work. The engine exhaust-washed structure presented in the preceding section, as well as other aerospace thermal structures such as thermal protection systems (TPS), can be idealized as a built up assembly of many plate- and shell-like components. When these types of thin-shell structures are subjected to elevated temperatures with sufficient

fixivity at their boundaries, they undergo either buckling or bowing due to thermal expansion. Both behaviors lead to out-of-plane deformation with respect to the original geometry. It is this out-of-plane deformation that in some cases can exhibit significant nonlinear behavior.

The presence of this nonlinearity is of particular concern as we consider the application of optimization methods for the design of thermal structures as additional challenges arise when applying structural optimization to nonlinear responses. These challenges are related to the nonlinear solution procedure utilized in the physics-based model, which due to iteration can be costly and may not be robust in convergence. In addition, the computational requirements of nonlinear sensitivity analysis are much greater when compared to linear cases, often to the point of making standard procedures impractical [27].

Thus, before proposing design solutions for exhaust-washed structures, a better understanding of the significance of geometric nonlinearity in these components is required. In order to obtain this, characteristic geometry of exhaust-washed structures is studied. In doing so, some particular geometric properties in characteristic models are identified for which geometric nonlinearity is important. This knowledge lends insight into the analysis fidelity (linear or nonlinear) that is necessary to capture critical physics in different cases and which ultimately must be transitioned into any structural optimization process.

### 2.2.1 Beam Strip Model

A parameterized curved beam strip model is first used to demonstrate the significance of geometric nonlinearity induced by thermal loads. This simple 2D model directly represents a semi-infinite cylindrical shell, but also serves as a suitable idealization of the basic components of more complex exhaust-washed structures among other thin-shell thermal structures. A schematic of the model is shown in Figure 17. Here,  $L$  denotes the span covered by the strip,  $\delta$  is a measure of curvature (which is circular), and  $t$  is the thickness of the strip. A rectangular cross section with unit width into the page is also assumed. Since boundary conditions are extremely important in cases of thermal expansion, linear elastic boundaries are utilized. By varying  $K_a$  (axial) and  $K_r$  (rotational) stiffness, all cases from fully clamped and simply supported to free expansion can be modeled. Loading consists of a spatially uniform temperature increase  $T$ .

In thermal structures, often the magnitude of temperature load is misleading with respect the severity of its structural consequences because it does not reflect material properties. A more suitable indicator of the severity of a given temperature level for a material is the product of its elastic modulus  $E$ , coefficient of thermal expansion (CTE)  $\alpha$ , and the elevated temperature  $T$ . Examples for various materials at common operational temperatures are given in Table 3. We note that with respect to the overall effect of temperature loading, a CMC component with extremely low CTE may experience nearly the same thermoelastic effects as a titanium alloy due to increased operational temperature. In

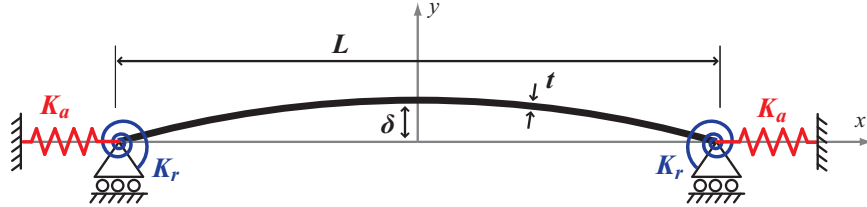


Figure 17: Parameterized curved beam strip model (note: curvature is of a circular profile)

this section, properties and loading given for Ti-6-2-4-2 are utilized, but attempting to retain generality, it is noted here that results in this section scale rather proportionally with  $E\alpha T$ .

Material	$T$ (°F)	$E$ ( $10^6$ psi)	$\alpha$ ( $10^{-6}/^{\circ}\text{F}$ )	$E\alpha T$ ( $10^3$ psi)
Ti-6-2-4-2	900.0	12.5	5.5	61.86
Inconel 718	1300.0	24.0	14.5	764.4
Gr-BMI (0/90)	400.0	8.0	12.0	38.40
CMC	2000.0	26.2	2.5	131.0

Table 3: Comparison of various engineering material properties at high operating temperature

The curved strip is modeled in MD Nastran using 250 2-node beam elements, which is a sufficient discretization based on mesh convergence. Analysis is performed using both linear and nonlinear solvers. In the nonlinear solution, effects of large displacement, strain stiffening, and follower forces are capturing using an incremental solution and differential stiffness terms. These effects are absent in linear analysis. Finally, the model inputs are parameterized using a thickness to span length ratio ( $\frac{t}{L}$ ) and a curvature to span length ratio ( $\frac{\delta}{L}$ ).  $\frac{t}{L}$  ranges from 0.005 to 0.05 and  $\frac{\delta}{L}$  ranges from 0.0 to 0.5 in practical applications.

## 2.2.2 Deformation

The deformation response of the strip model predicted by both linear and nonlinear analysis is given in Figure 18. Three  $E\alpha T$  and two  $\frac{\delta}{L}$  values using clamped (a,c) and simply supported (b,d) boundaries are given. Curvature measures of 0.01 (a,b) and 0.05 (c,d) are indicated in the figure. Here  $\frac{t}{L} = 0.013$  and the black curve denotes the undeformed strip, and dashed and solid curves denote linear and nonlinear deformed shapes, respectively.

From Figure 18 it is evident that the effects of geometric nonlinearity in the deformation response (which is observed as the difference between the linear and nonlinear response curves) increase with  $E\alpha T$  for both sets of boundaries and for both low and high curvature. However, when comparing Figure 18 (a,b) to Figure 18 (c,d) we see that the beam of greater curvature shows much less discrepancy between linear and nonlinear predictions. We also note that when using linear analysis, in which it is assumed that loading acts only on the undeformed configuration, the magnitude of deformation simply increases monotonically with increased  $E\alpha T$ . This is not observed in nonlinear

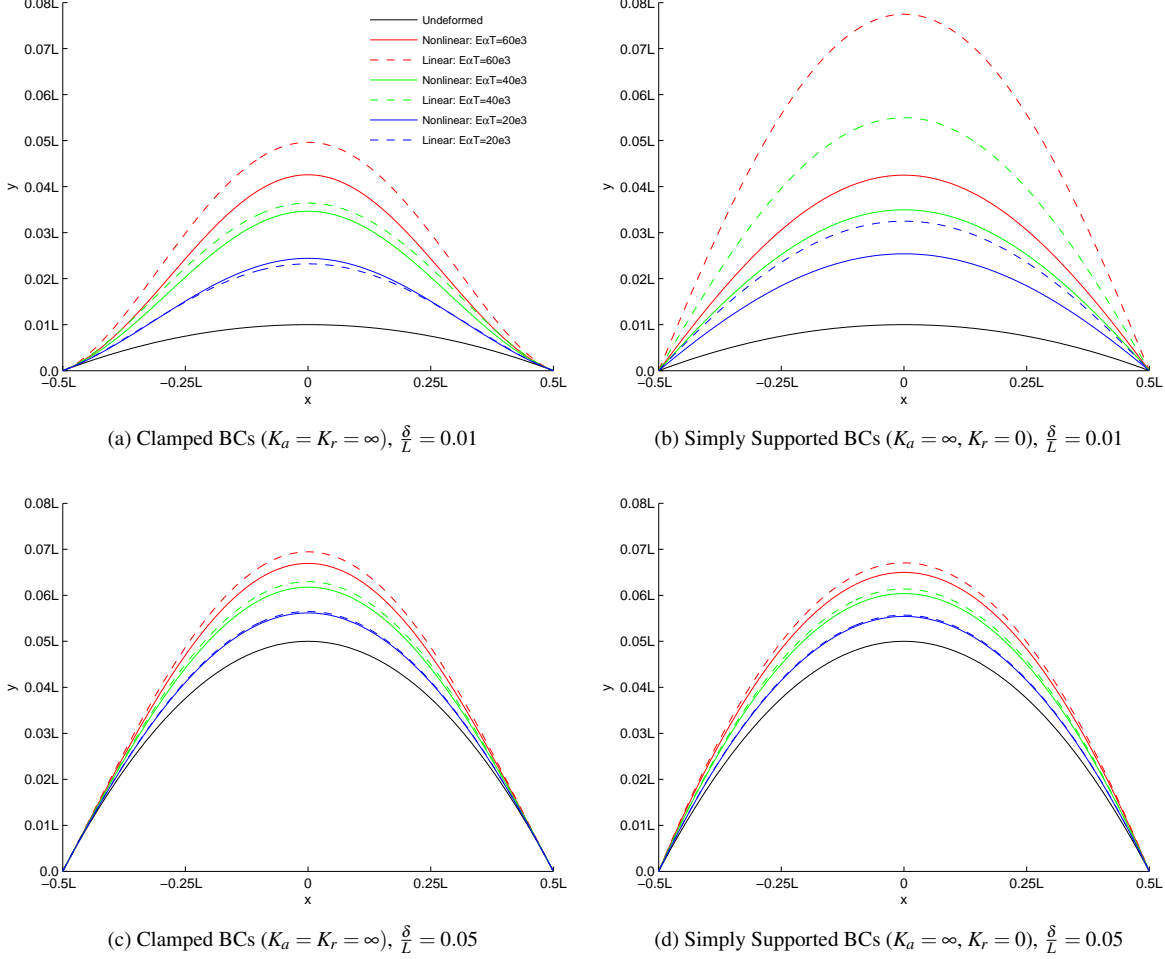


Figure 18: Deformation of curved beam strip for (a,c) clamped and (b,d) simply supported boundaries. Curvature ratios are (a,b)  $\frac{\delta}{L} = 0.01$  and (c,d)  $\frac{\delta}{L} = 0.05$ .

analysis, where the effects of stress stiffening preclude this behavior. This is especially evident in the curved strips of low curvature in Figures 18a and 18b.

### 2.2.3 Parametric Contributions

To understand the effect of dimensional parameters on the significance of geometric nonlinearity, we now perform a parametric study by varying the thickness of the strip for various values of curvature. Figure 19a shows the vertical displacement at the center of the strip and Figure 19c shows the maximum stress as function of thickness ratio  $\frac{t}{L}$  for four different values of curvature measure  $\frac{\delta}{L}$  and clamped boundaries. Figures 19b and 19d show the same results for simply supported boundaries. Here  $E\alpha T = 60 \times 10^3$  based on the deformation plots, which indicated that the difference between linear and nonlinear analysis increased with  $E\alpha T$ . As mentioned prior, this value represents typical conditions for a high temperature titanium alloy.

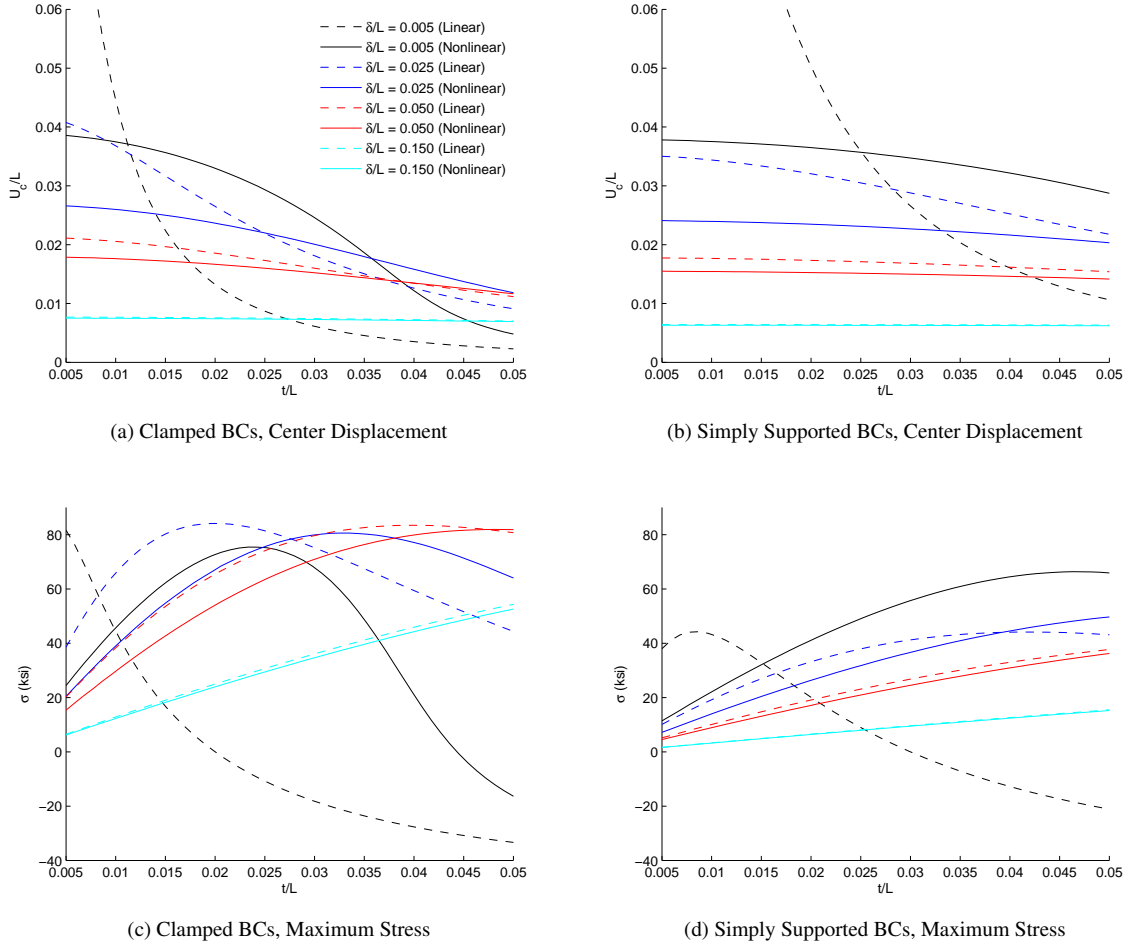


Figure 19: (a,b) Center displacement and (c,d) maximum stress as functions of thickness ratio for multiple curvature ratios ( $E\alpha T = 60 \times 10^3$ ) (a,c) Clamped boundaries and (b,d) simply supported conditions.

In any plot in Figure 19 we see that increasing the curvature reduces the difference between linear and nonlinear analysis predictions, as noted previously. However, more interesting than simply the difference between the analyses is the trends that result for varying thickness. In each plot, we see that for strips of larger curvature (blue, red, and cyan curves), the general trend for increasing the thickness is similar for both linear and nonlinear analyses. In fact, for the highest values of curvature shown here, nearly the same predictions are obtained. This observation is valuable because it indicates that in the design optimization of structures with sufficient curvature a linear analysis with an error factor or factor of safety may be sufficient to accommodate nonlinearity in design. On the other hand, for a curvature ratio  $\delta/L = 0.005$  (black curve), which corresponds to a nearly flat strip, this practice would not be effective. In this case, linear and nonlinear analyses respond completely different to variations in thickness. This indicates that the linear analysis fails to capture the fundamental physics governing the displacement and stress response, which we may now attribute to nonlinear effects. The scale of this discrepancy is also remarkable. For greater curvature ratios, increasing the thickness appears to reduce the discrepancy between linear and nonlinear analysis; however, for nearly

flat geometry, the differences persist over an entire order of magnitude of thickness variation ( $t/L$  from 0.005 to 0.05).

#### 2.2.4 Boundary Contributions

To this point, we have only studied strips with either clamped or simply supported boundaries, which are both extreme cases of rigid fixivity for thermal expansion. In reality, the true boundary conditions of a thermally restrained structure are dependent upon the stiffness of surrounding components as well as the type of joints utilize. To understand the implications of boundaries with finite stiffness, we now employ the elastic spring conditions initially shown on the schematic in Figure 17. A parametric study similar to the previous one, again with varying thickness ratio and multiple curvature ratios, is performed. However, rather than rigid clamped or simply supported boundaries, multiple finite values of rotational ( $K_r$ ) and axial ( $K_a$ ) stiffness are systematically prescribed. To provide some relational context to the magnitude of stiffness boundaries that are applied in each case, the spring stiffness values  $K_r$  and  $K_a$  are parameterized using the following relationships

$$K_a = k_a \frac{AE}{L}, \quad (8)$$

$$K_r = k_r \frac{EI}{L^2}. \quad (9)$$

Here, we note two quantities provide rough estimations for the stiffness of the beam strip itself. In Equation (8),  $AE/L$  is analogous to the stiffness of an axial bar, and in Equation (9),  $EI/L^2$  is analogous to the bending stiffness of a cantilever beam, both of length  $L$ . If  $K_a$  and  $K_r$  correspond to the stiffness of adjoining structures, the parameters  $k_a$  and  $k_r$  represent a rough approximation for the ratio between the stiffness of adjoining structure (or boundary stiffness) to the stiffness of the beam strip itself in the axial and rotational directions, respectively. It is noted that a truly axial dimension exists only for a perfectly flat strip; however, the concept of stiffness roughly in the *in-plane* direction is an appropriate consideration for curved beams. For clarity, a unit value of  $k_a$  or  $k_r$  indicates the boundary condition has approximately equal stiffness to the beam strip while a large value asserts that the boundary is much stiffer than the strip in that dimension.

Figure 20 shows the maximum stress in the strip as a function of thickness for multiple values of finite rotational stiffness, which are indicated with different colors. In the axial direction, zero displacement at the boundaries is prescribed ( $K_a = \infty$ ). In the figure, 20a shows results for  $\delta/L = 0.005$  (nearly flat) and 20b for  $\delta/L = 0.050$  (modest curvature). Comparing the trends with increasing thickness we again see that in the case of greater curvature, linear analysis is able to capture the correct trend in stress response while nonlinear effects dominate the behavior strips with less curvature. This statement holds regardless of the rotational stiffness values; however, it does appear in Figure 20b that increasing the rotational boundary stiffness leads to a larger magnitude discrepancy between analysis predictions.

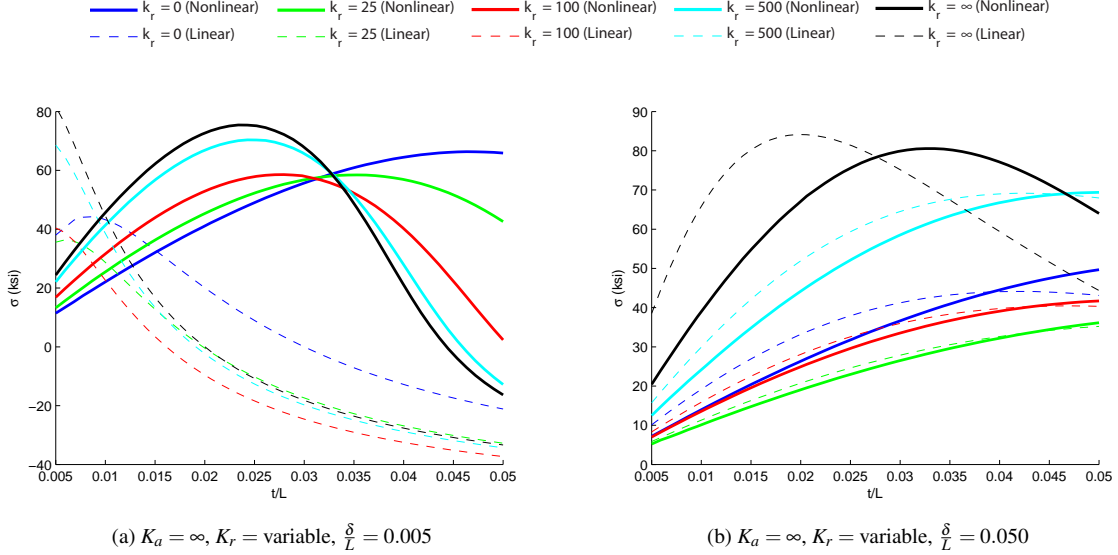


Figure 20: Maximum stress in the beam strip as a function of thickness with finite values of rotational stiffness at boundaries and curvature ratios of (a) 0.005 and (b) 0.050.

This implies that to some extent, rotational stiffness may activate some nonlinear effects likely due to its influence on the out-of-plane displacement of the strip.

Figure 21 shows the maximum stress results as a function of thickness for multiple values of axial/in-plane stiffness. This time, zero rotational displacement is prescribed at the boundaries ( $K_r = \infty$ ) and results shown are for curvatures of  $\delta/L$  or 0.005 and 0.050 in 21a and 21b, respectively. Again, we observe that with the greater curvature

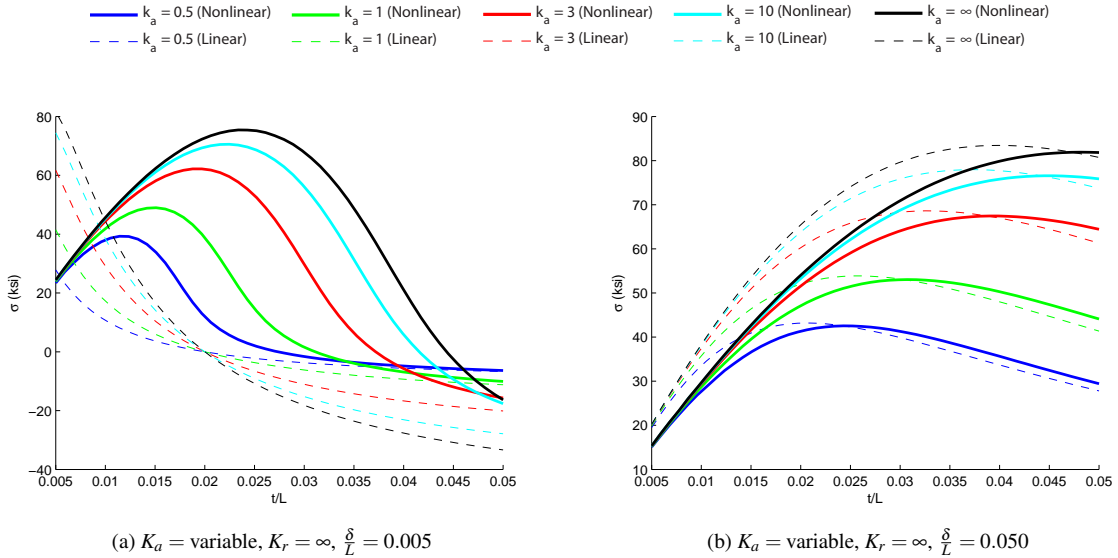


Figure 21: Maximum stress in the beam strip as a function of thickness with finite values of axial stiffness at boundaries and curvature ratios of (a) 0.005 and (b) 0.050.

in Figure 21b, the linear analysis is better able to capture the variation in stress. On first inspection, it may appear

that in Figure 21a, linear analysis correctly captures a trend of decreasing stress with increasing thickness for strips of thickness ratio greater than approximately  $t/L = 0.025$ , but noting the state of stress (indicated by its sign) we conclude otherwise. Here, linear analysis predicts a state of purely compressive stress at much lower thickness ratios, which again alludes to the dominance of nonlinear effects in the out-of-plane (bending) deformation behavior. Similar to the cases of rotational stiffness, from 21b increasing axial stiffness appears to increase the difference in analysis predictions, which is again related to the contribution of boundary stiffness to the out-of-plane deformation that results.

### 2.2.5 Summary

In summary, several notable conclusions may be drawn regarding the significance of nonlinearity for thermally restrained structures and the ability of linear analysis to predict thermoelastic behavior. These conclusions have important implications when considering the application of design optimization methodologies, which are generally based on linear analysis models due to computational cost and convenient sensitivity analysis. The basic observations are

- increasing temperatures (or increasing  $E\alpha T$ ) increases the effect of geometric nonlinearity,
- increasing curvature reduces the effect of geometric nonlinearity,
- and increasing both rotational and axial stiffness increases the effect of geometric nonlinearity.

Finally, from a structural mechanics point of view, the significant nonlinear effects in strips of low curvature are (i) stress stiffening in thin structures and (ii) follower forces in thick structures.

## 2.3 Challenging Design Response

In the previous section, results of a characteristic thermal structure were explored to identify regions within the design domain where geometric nonlinearity is most significant. With this understanding, we now investigate the behavior of the thermoelastic response itself, rather than comparisons between different analysis types. Here, we regard the nonlinear response as the true behavior at all regions within the design space and explore the non-intuitive effects of parametric variation on thermoelastic deformation and stress responses.

### 2.3.1 Observations from Beam Strip Model

We begin by investigating the results obtained for the parameterized beam strip model shown in Figure 17 with elastic boundary conditions. The results shown in Figures 20 and 21, which give the maximum stress in the strip as a function of the thickness, contain interesting parametric stress behavior across a wide variety of geometries and boundary conditions. Remarkably, in each plot we observe *increases* in the maximum stress with increases in thickness, especially

beginning at low  $t/L$  values. This behavior is unique to structures with so called design-dependent loading, which includes temperature loads, and is counter-intuitive when compared to mechanically loaded structures. One of the most common techniques for reducing stresses in mechanically loaded structures is to increasing their stiffness by increasing the thickness. However, in this case, the design-dependency of temperature loading results in additional thermal loading from the added material that also undergoes thermal expansion. Thus, in some circumstances represented in Figures 20 and 21, the proper prescription for reducing thermal stresses is actually to *reduce* the thickness. In practice, this may not always be possible when considering other design requirements related to vibration and dynamic stability. In some cases shown in the same figures, we do see that for higher values of  $t/L$  that increasing thickness can lead to stress reduction, particularly in cases with high (or infinite) stiffness in the rotational direction at boundaries. However, we note that if considering an initially thin structure, significant increases in thickness (exceeding 3-5 times the original thickness) are required to realize a reduction in stress. This translates to significant increases in structural weight and also when comparing Figure 20a to 20b and Figure 21a to 21b, the effectiveness of this treatment diminishes with added curvature in the geometry.

A final observation of the beam strip results in Figures 20 and 21 is that with the exception of strips with thickness greater than approximately  $t/L = 0.035$ , higher curvature translates to lower stress levels for a variety of boundary conditions. This indicates that if the functional design space of a thermal structure includes the possibility for shape changes, while size optimization may not be effective, structural shape optimization may be possible to satisfy stress constraints. Unfortunately, in the design of engine exhaust-washed structures, the geometric shape of many parts of the structure are typically fixed by exhaust fluid flow and observability design requirements.

### 2.3.2 Curved Shell Model

To validate the general observations from the beam strip model, we now briefly investigate the stress response of a curved thin shell subjected to thermal loads. The parameterized model of the shell, which is assumed to have spherical curvature, is given in Figure 22a. The blue region denotes the quarter symmetric section of the structure that is utilized for finite element analysis. The finite element model, discretized with 2500 quadrilateral plane stress elements, is shown in Figure 22b. The boundary conditions explored here are analogous to the axial/in-plane stiffness beam strip study with results in Figure 21. Zero rotation and vertical displacement along the edges indicated by red is specified and symmetry conditions are prescribed on the edges highlighted with blue in Figure 22b. The in-plane stiffness is again parameterized according to Equation 8, but here  $A$  is computed for the entire cross-section along the edges of the shell. Once obtained, the total spring stiffness is divided equally among spring elements at each node on the edges denoted by red. The deformed shape and stress response of an example model is shown in Figure 23 for both curvatures of  $\delta/L$  of 0.005 and 0.050. In this case,  $E\alpha T = 18.25$ , which corresponds closely to a CMC material at

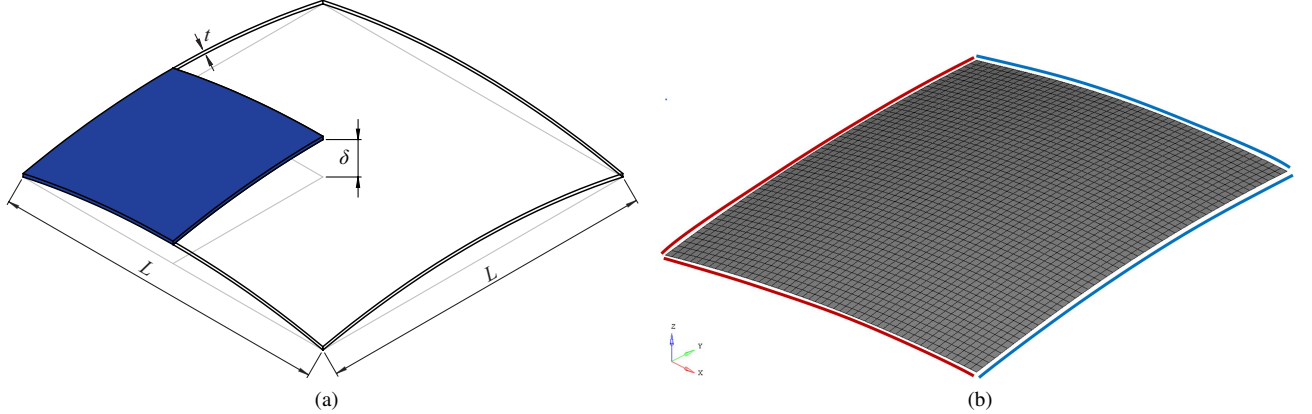


Figure 22: (a) Schematic of curved shell model where blue region denotes quarter symmetric section used for analysis and (b) quarter symmetric finite element model.

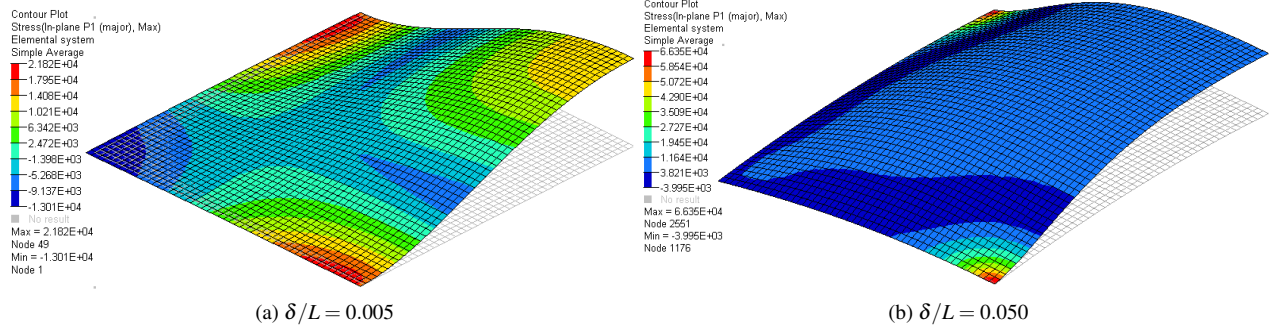


Figure 23: (a) Maximum principle stress in quarter symmetry shell model for  $t/L = 0.02$  and  $k_a = 1.0$ . Note deformation shape is magnified by 10.

1000°F,  $t/L = 0.02$ , and  $k_a = 1.0$ . We note the characteristic out-of-plane deformation response with respect to the original geometry. This deformation leads to maximum principle stresses located along the edges of the panel, which corresponds to the strip model where maximum stresses occurred at the root of the beam. In practice, this location represents the attachment points of a panel to substructure and is prone to both static failure and fatigue issues related to excessive thermal stresses.

Figures 24a and 24b show the parametric stress response of the shell as a function of thickness for curvature measures of  $\delta/L = 0.005$  and  $0.050$ , respectively. Here, in three-dimensions, identical observations to those in the previous section may be made. For the low curvature shell (Figure 24a) an increase in thickness again leads to an increase in stress for lower thickness values across a range of boundary stiffnesses. For greater thickness shells, stress reduction via thickness increase is possible, but again when beginning with a relatively low thickness shell, increasing the thickness by factors greater than two is required. For the case of higher curvature in Figure 24b, we observe no cases where increasing thickness leads to a reduction in maximum tensile stresses.

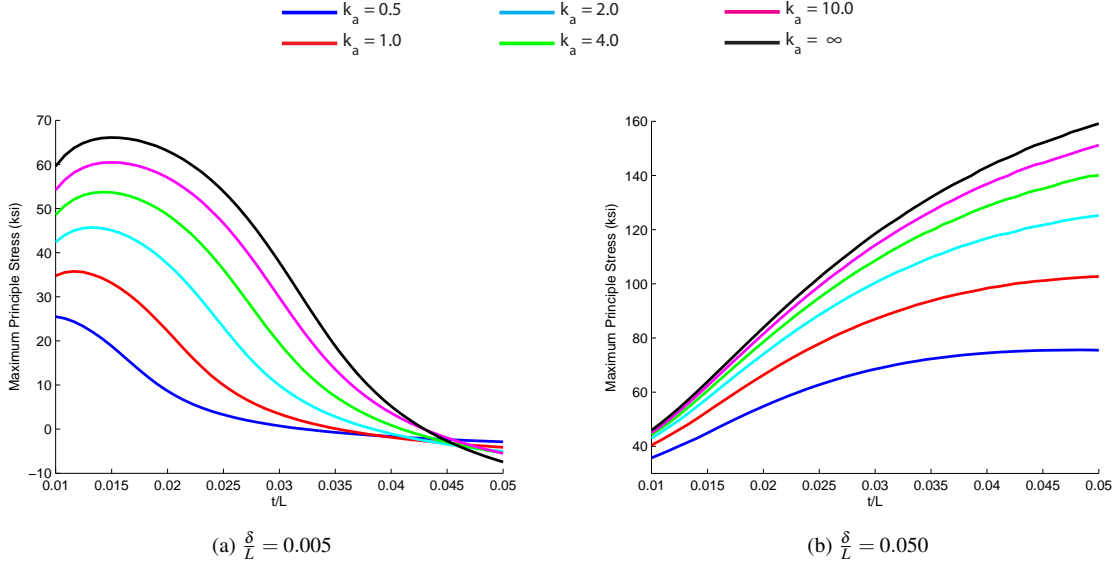


Figure 24: Maximum principle stress in shell model as a function of thickness with finite values of axial stiffness at boundaries and curvature ratios (a) 0.005 and (b) 0.050.

## 2.4 Chapter Summary

In this chapter, the characteristic response of engine exhaust-washed structures, along with the broader class of thin thermal structures with restrained expansion, has been explored. The fundamental out-of-plane deformation of thin structures, which has been shown to lead to damaging thermal stresses in practical applications, was observed in a conceptual exhaust-washed structure configuration subjected to a transient mission profile. The implications of geometric nonlinearity were also explored and some particular geometric features were identified that help to determine when nonlinear effects will be significant. Finally, the challenging and non-intuitive design space related to thermal stresses was investigated. From this exercise it may be concluded that when attempting to apply design optimization methodologies to EEWs that size optimization may not be effective due to design dependency of thermal loads. The stress responses did appear to be influenced by varying the shape (curvature), but within the context of the exhaust-washed structure design space, such a design modification may not be possible. As a result, the design domain for a candidate exhaust-washed structure must be expanded past modifying size and shape variables of a predefined configuration to include the material layout. Within the methods of design optimization, this expanded design parameterization can only be achieved using structural topology optimization, which is detailed in the next chapter.

### 3 Topology Optimization

#### 3.1 Background

Topology optimization is the process of determining the connectivity, shape, and location of voids inside a given solid design domain and is often understood as determining the best material distribution [28]. This allows for greater design freedom when compared to size and shape optimization, which deal with variables such as thicknesses or cross-sectional areas of structural members (sizing) and geometric features (shape) of predefined structural configurations. This is shown in Figure 25. As such, topology optimization has great benefit in early conceptual and preliminary design phases where changes have a significant impact on final component performance. Due in large part to its material layout capabilities, topology optimization is also a promising tool for thermoelastic design, which is fundamentally a problem of determining optimum structural layout to satisfy functional requirements while properly managing thermal expansion. It is also important to note that there are two types of topology optimization: discrete and continuum [29, 30]. In this document, we investigate only continuum formulations as the discrete methods are not appropriate for the problems of interest.

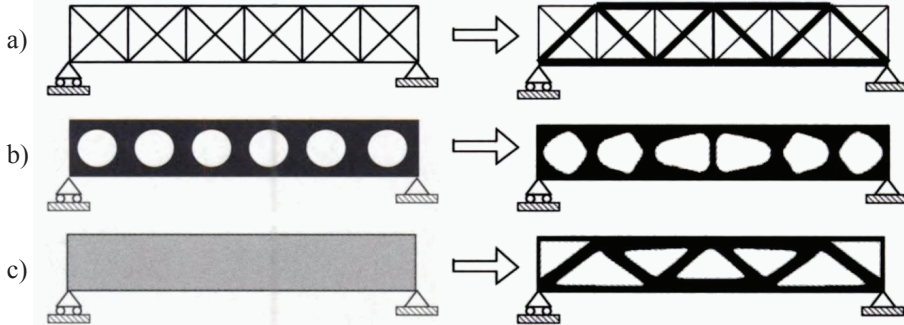


Figure 25: Three categories of structural optimization. a) Sizing optimization, b) shape optimization, and c) topology optimization. The initial design parameterizations are shown on the left with the resulting optimal solutions on the right [28].

#### 3.2 Methods

Several different methods exist for finite element-based topology optimization of continuum structures, but the common goal is to determine the existence or absence of material within a given region of a design domain. Usually, “solid/void” designs are desired because they can be physically realized using isotropic materials. Here, solid implies existence of material and void implies absence of material. The differences among methodologies lie in the parameterization of the design space. For example, some methods explicitly define the design directly on the finite element domain while others define a design implicitly using a separate function from which the structure is interpreted. The

following subsections outline some the current methods for topology optimization.

### 3.2.1 Homogenization

Practical finite element-based topology optimization of continuum structures began with the landmark work by Bendsøe and Kikuchi, who posed a structural layout problem within the context of homogenization theory [31]. This early technique of the explicit type, known now as the *homogenization method*, is based on the ability to model porous materials, and their associated macro-scale material properties, from a periodic microstructure defined within a unit cell. Two potential microstructures (among many alternatives), a square cell with a rectangular hole and a layered microstructure with two isotropic constituents, along with the relationship to the macro-scale discretized finite element model are shown in Figure 26. With the appropriate microstructure definition, and under the assumption of infinitesimally small periodic unit cells, any anisotropic macro-scale material representation can be achieved, including pure solid, pure void, and intermediate (composite/porous) material.

In practice, the parameters corresponding to the microstructure, for example  $\mu_1$ ,  $\mu_2$ , and  $\theta$  in Figure 26a, are taken as free variables for design. A single set of microstructure variables may be used for each finite element or a sub-mesh may be utilized for fine structures. The topology optimization problem then becomes to determine the combination of microstructure variables corresponding to the optimal macro-scale distribution of properties that minimizes an objective function. This formulation was successfully applied to various problems throughout the 1990s, but has fallen out of favor in the literature in the last decade due to the development of more efficient methods. These newer methods, which are described in the following sections, can capture the same design features with fewer design variables when compared to homogenization. In addition, many of the common numerical issues found in explicit types of topology parameterizations are more easily circumvented with alternative formulations.

### 3.2.2 Density-based Methods

Currently, the most widely used methods for structural topology optimization are explicit parameterizations that are broadly classified as *density-based methods*. As with homogenization, these techniques operate on fixed domain of finite elements; however, rather than a set of microstructure properties, each finite element contains only a single design variable. This variable is often understood as the element material density,  $\rho_e$ . The material properties of each element, for example the elastic modulus or thermal conductivity, are made functions of density design variables by way of an interpolation function. Penalty methods are then utilized to force solutions to suitable “solid/void” designs. The most well known density-based method is the SIMP method (Solid Isotropic Material with Penalization) and nearly all commercial topology optimization tools utilize a density-based method to the author’s best knowledge.

The fundamental mathematical statement of a density-based topology optimization problem contains and objective

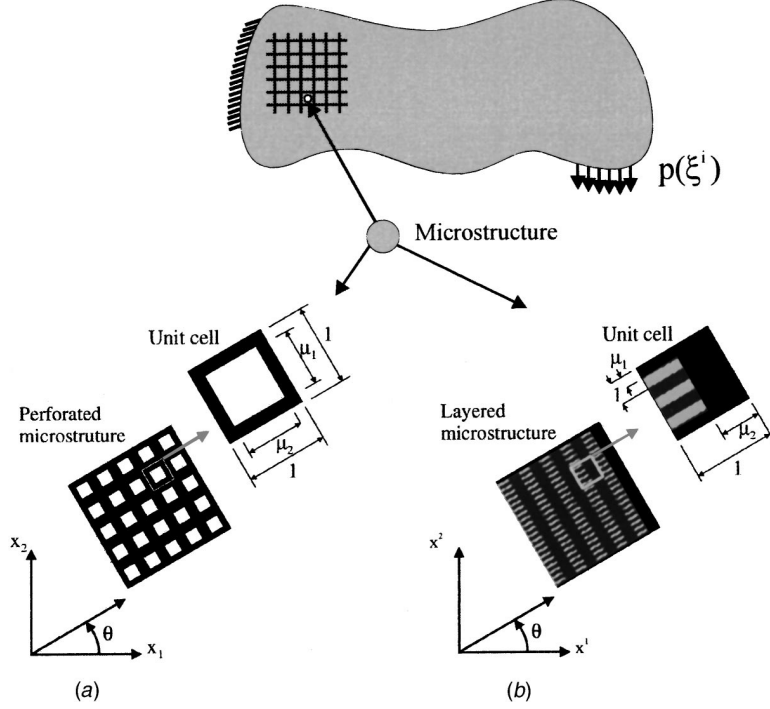


Figure 26: Microstructures for 2D continuum topology optimization with the homogenization. (a) Square unit cell with rectangular holes, and (b) layered microstructure with two different isotropic materials [29].

function, set of constraints (that generally includes an upper limit on material usage), and a discretized representation of the physical system. A general formulation based on linear static finite element analysis may be given as

$$\begin{aligned}
 \min : & f(\mathbf{x}, \mathbf{U}) \\
 \text{subject to : } & \mathbf{K}(\mathbf{x})\mathbf{U} = \mathbf{F}(\mathbf{x}) \\
 & g_i(\mathbf{x}, \mathbf{U}) \leq 0 \\
 & 0 \leq x_e \leq 1
 \end{aligned} \tag{10}$$

where  $f$  is the objective function,  $\mathbf{x}$  is the vector of density design variables that are related to  $\rho_e$ ,  $\mathbf{U}$  is the displacement vector,  $\mathbf{K}$  is the global stiffness matrix,  $\mathbf{F}$  is the force vector, and  $g_i$  are the constraints. We note that the stiffness matrix  $\mathbf{K}$ , and sometimes load vector  $\mathbf{F}$  are explicitly dependent upon the density design variables. Within this generalized statement, a number of problems can be formulated considering design responses including compliance, stresses, frequency, displacements, and alternative physics such as eigenvalue problems, fluid flow, and nonlinear systems.

**Density Interpolation/Penalization** A critical aspect of density-based methods is the selection of an appropriate interpolation function and penalization technique to relate the physical quantities of the problem with continuous

density design variables. As previously noted, the distributed function for design is interpreted as the physical density of each finite element,  $\rho_e$ . The values of density range as  $0 \leq \rho_e \leq 1$  or  $0 < \rho_{min} \leq \rho_e \leq 1$  where 0 corresponds to a void element, 1 to a solid element, and  $\rho_{min}$  is the minimum value of density, which is required with some formulations to prevent difficulties associated with zero values. These difficulties include singularity in finite element matrices and issues with the inability of material to reappear in an area with zero density. With the choice of this parameterization comes the need to steer the problem toward a solid/void solution. This is typically accomplished in density-based topology optimization using implicit penalization techniques, the most common of which is the Solid Isotropic Material (originally Microstructure) with Penalization (SIMP) method [32, 33]. In the SIMP method, also referred to as the power law or fictitious material model, density variables are penalized with a basic power law (whose value is finite) and multiplied onto physical quantities such as material stiffness, cost, or conductivity. This is demonstrated in Equation (11) where the SIMP method is applied to the elastic modulus of an element.

$$E(\rho_e) = \rho_e^p E_0 \quad (11)$$

Here,  $E(\rho_e)$  is the scaled modulus,  $E_0$  is the modulus of the solid material, and  $p$  is a finite penalty parameter. We note that for values of  $0 \leq \rho_e \leq 1$  and a positive  $p$  (commonly taken as 3),  $E$  is bounded between zero at zero density and its solid value  $E_0$  when  $\rho_e = 1$ .

Alternative interpolation schemes have been developed primarily to address deficiencies in the SIMP method for certain classes of problems. One of these is known as the Rational Approximation of Material Properties (RAMP) [34]. A desirable feature of the RAMP model is that, unlike SIMP, it has nonzero sensitivity at zero density. As a result, the RAMP material model has been shown to remedy some numerical difficulties in problems related to very low density values in the presence of design dependent loading. Another alternative is known as the SINH (pronounced “cinch”) method, which is based on a hyperbolic sine function [35]. This scheme differs from others in that usually material parameters are penalized, whereas in the SINH formulation the volume is penalized. As such, intermediate density material consumes more volume with respect to its load-carrying capability than solid or void material. A comparison of the SIMP, RAMP, and SINH penalization schemes is shown in Figure 27 where  $\rho$  is the physical density,  $p$  is the penalization parameter for SIMP and SINH,  $q$  is the penalization parameter for RAMP, and  $\eta$  is the value of the interpolation. The range of parameters shown is representative of those used in practice, with the actual value depending on the underlying physics of the problem.

**Regularization** With the introduction of interpolation functions as described above to parameterize the topology optimization domain, some associated numerical issues must be addressed. These issues are checkerboarding and mesh dependency. Checkerboarding, which refers to the formation of adjacent solid-void elements arranged in a

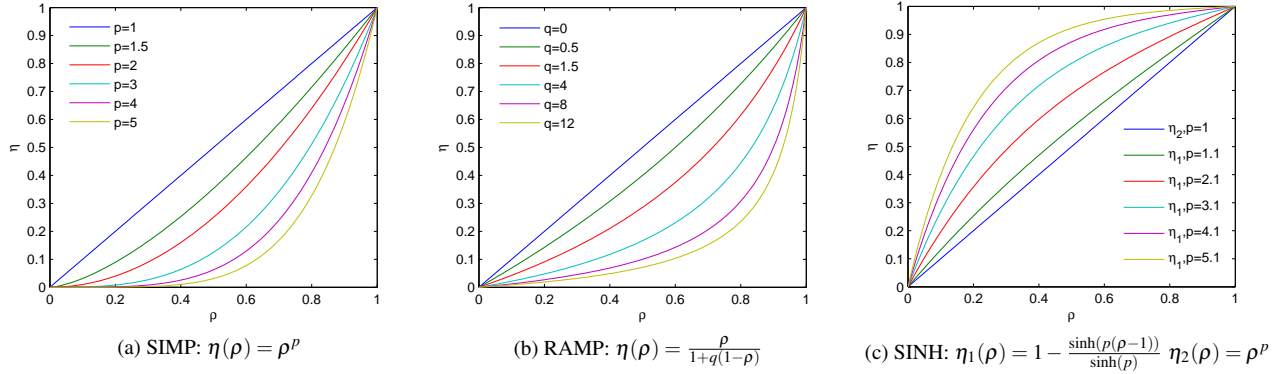


Figure 27: Interpolation functions for density-based topology optimization. a) SIMP, b) RAMP, and c) SINH.

checkerboard pattern, has been shown to be an issue related to common four noded bilinear quadrilateral and eight noded brick finite elements. Apart from dedicated techniques that will be highlighted, higher-order finite elements have been shown to remove checkerboarding in some cases. Mesh dependency, which concerns the fact that a smaller discretization allows for smaller features to develop in optimum results, must be alleviated to enforce minimum length scale. Examples of topology optimization results that exhibit checkerboarding and mesh dependency are shown in Figures 28 and 29, respectively. Among the techniques that have been developed to address these features, it is noted that those that prevent mesh dependency will generally also eliminate checkerboards; however, checkerboard-prevention algorithms may not necessarily alleviate mesh dependency.



Figure 28: Example of checkerboarding in topology optimization.

The removal of checkerboards and mesh dependency in topology optimization is known as domain regularization, of which there are two primary methods: constraint methods or filters. Constraint methods utilize localized or global-level constraints that are added to the optimization problem to control parameters such as the perimeter of structural boundaries. The main drawback of constraint methods is that their application is often problem dependent, with tuning required to achieve desired results. Filtering methods on the other hand are straightforward to implement and add only minor computational expense.

Filtering is applied via direct modification of density variables or sensitivities based on information from a neighborhood of surrounding elements. The basic sensitivity [36] and density filters [37, 38], in addition to more modern



Figure 29: Example of mesh dependency in topology optimization. Mesh sizes are a)  $60 \times 20$ , b)  $90 \times 30$ , c)  $150 \times 50$ , and d)  $300 \times 100$ .

projection methods [39, 40], are now highlighted. The sensitivity filter modifies the sensitivities  $\partial f / \partial x_e$  as

$$\widehat{\frac{\partial f}{\partial x_e}} = \frac{1}{x_e \sum_{i \in N_e} H_{ei}} \sum_{i \in N_d} H_{ei} x_i \frac{\partial f}{\partial x_e} \quad (12)$$

where  $N_d$  is the set of designable elements  $i$  for which the center-to-center distance  $\Delta(e, i)$  to element  $e$  is smaller than the filter radius  $r_{min}$  and  $H_{ei}$  is a weight factor defined as

$$H_{ei} = \max(0, r_{min} - \Delta(e, i)). \quad (13)$$

From this definition, we see that the filtered sensitivity,  $\widehat{\partial f} / \partial x_e$  is a weighted sum of sensitivities of surrounding elements. The weight for each contribution to the filtered sensitivity at element  $e$  decays linearly as the distance increases and is zero for elements whose centroid lies outside the filter radius. This is shown in Figure 30. Despite its widespread use, only recently has a rigorous physics-based analogy for the workings of the sensitivity filter been obtained [41]. Prior to this the sensitivity filter was utilized based largely on computational experience that demonstrated its effectiveness [28].

Rather than filtering the sensitivity information, the density filter specifies the element density based on a weighted average of the densities around it. This is given as

$$\rho_e = \frac{1}{\sum_{i \in N_d} H_{ei}} \sum_{i \in N_d} H_{ei} x_i \quad (14)$$

where we now note the important distinction between the physical density  $\rho$ , which defines the actual topology, and

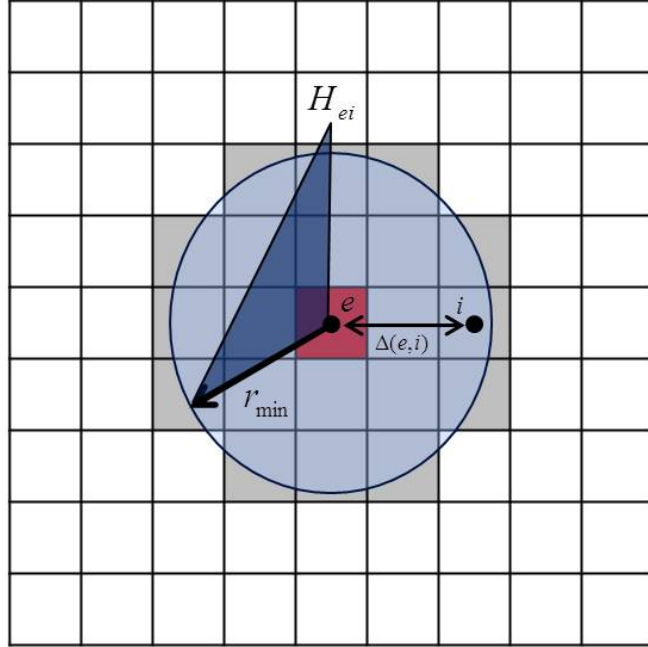


Figure 30: Neighborhood definition for the application of sensitivity and density filters.

the design variable densities  $x$  on which the optimization problem is defined. This distinction is important because after application, the sensitivity of a response  $f$  is explicitly found with respect to the physical density  $\rho_e$  and a chain rule is necessary to find the sensitivity with respect to the design variable density, now denoted as  $x_e$ . The required chain rule operation for sensitivity with respect to a density design variable  $x_j$  is given by Equation (15) and is easily implemented in practice using matrix operations.

$$\frac{\partial f}{\partial x_j} = \sum_{e \in N_j} \frac{\partial f}{\partial \rho_e} \frac{\partial \rho_e}{\partial x_j} = \sum_{e \in N_j} \frac{1}{\sum_{i \in N_e} H_{ei}} H_{je} \frac{\partial f}{\partial \rho_e} \quad (15)$$

This consideration is not necessary for the sensitivity filter because in that case the design variable and physical densities are equal to one another. Application of either the sensitivity filter or the density filter will prevent features smaller than the twice the filter radius  $r_{min}$  from occurring in the results. Naturally, this prevents checkerboard patterns since they are a small feature, and also allows the prescription of minimum size on structural features.

A basic consequence of sensitivity and density filtering is the formation of a gray transition material between solid and void regions. In many cases, this material cannot be physically realized in a manufactured component. Recent projection methods have been developed to address this in cases where crisp boundary definition is important. Both Heaviside functions [39] and morphology-based operators [40, 42] are utilized to project filtered densities into 0/1 space.

The Heaviside filter is a modification of the original density filter given by Equation (14) with a Heaviside step

function that projects the filtered density (from now on called the intermediate density and denoted as  $\tilde{x}_e$ ) to a physical density. The physical density  $\rho_e$  equals one if  $\tilde{x}_e > 0$  and zero if  $\tilde{x}_e = 0$ . To facilitate gradient-based optimization, which requires continuous functions, a smoothed Heaviside function is utilized as

$$\rho_e = 1 - e^{\gamma\tilde{x}_e} + \tilde{x}_e e^{-\gamma}. \quad (16)$$

The parameter  $\gamma \geq 0$  describes the curvature of the projection which is linear at  $\gamma = 0$  and approaches a Heaviside step as  $\gamma$  approaches infinity. In most applications, a continuation scheme is used where  $\gamma$  is initially equal to zero and gradually increased; however, recently a version that does not require continuation has been demonstrated [43]. In addition, since density variables are modified by the projection, a chain rule must be applied to obtain the sensitivity of a response to the intermediate density. This is given by

$$\frac{\partial f}{\partial \tilde{x}_e} = \frac{\partial f}{\partial \rho_e} \frac{\partial \rho_e}{\partial \tilde{x}_e} \quad (17)$$

where the derivative of the physical density  $\rho_e$  with respect to the intermediate density  $\tilde{x}_e$  is given by

$$\frac{\partial \rho_e}{\partial \tilde{x}_e} = \gamma e^{-\gamma\tilde{x}_e} + e^{-\gamma}. \quad (18)$$

Figure 31 shows characteristic results of filtering and projection. Here filtering has been used to prevent checkerboards and enforce minimum length scale. Note the gray transition material along structural boundaries for (a) sensitivity and (b) density filters. This region is eliminated using the (c) Heaviside projection.

### 3.2.3 Hard-kill Methods

In contrast to the homogenization and density-methods another class of explicit techniques, called *hard-kill methods*, for topology optimization do not relax the discrete finite-element design domain to a continuous form. They work by gradually removing (or adding) elements to the design domain. The choice of material to be removed or added is based on heuristic criteria, which may or may not be based on sensitivity information. As a result of these heuristic features, the technical rigor of these methods are sometimes called into question as a robust theoretical basis does not exist [44, 45]. The most well known hard-kill methods of topology optimization is Evolutionary Structural Optimization (ESO) [46] and, more recently, Bi-directional Evolutionary Structural Optimization (BESO) [47], which allows for addition of elements.

One of the most attractive features of hard-kill methods such as ESO is the simplicity with which they can be utilized with commercial finite element packages. Often times, the integration of the algorithms with FEA solvers

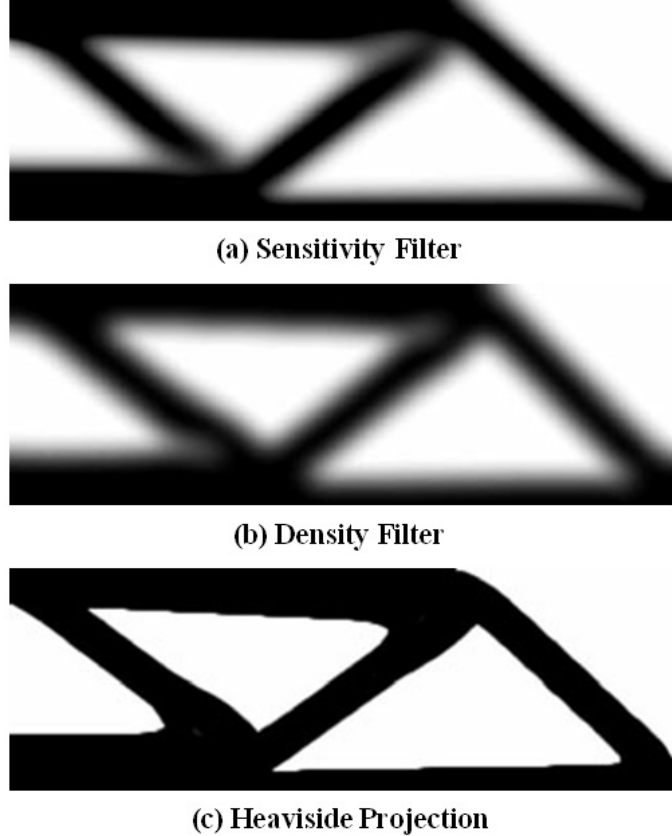


Figure 31: Characteristic topology optimization results using (a) sensitivity filtering, (b) density filtering, and (c) Heaviside projection.

requires only simple pre- or post-processing steps. In addition, hard-kill methods for topology optimization result in a design with crisply defined structural boundaries that are free of intermediate or gray material because finite elements are explicitly defined as existent or absent.

### 3.2.4 Boundary Variation Methods

*Boundary variation methods* are a most recent development in structural topology optimization with their roots lying in shape optimization techniques. In contrast to the previous methods, they are based on implicit functions that define structural boundaries rather than an explicit parameterization of the design domain. Figure 32a shows an explicit representation where the domain,  $\Omega$ , exists as an *explicit* parameterization of variables  $x$  between 0 and 1. The structural boundary  $d\Omega$  then exists at the interface of regions 0 and 1. Figure 32b demonstrates an *implicit* representation where the structural boundary is implicitly specified as a contour line of the field  $\Phi$ , which is a function of  $x$ .

Two current boundary variation methods are the level set and the phase-field methods. These methods produce results in the design domain with crisp and smooth edges that require little post-processing effort to interpret results.

In addition, these methods are fundamentally different than shape optimization techniques because they allow for not only the movement of structural boundaries, but also the formation, disappearance, and merger of void regions, which defines true topological design.

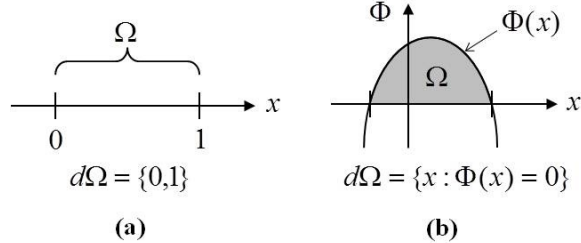


Figure 32: (a) Explicit versus (b) implicit representation of a design domain and boundaries.

**Level Set Method** In the level set method, boundaries are represented as the zero level curve (or contour) of a scalar function  $\Phi$  (the level set function) as shown simply for 2D topologies in Figure 33. Boundary motion and merging, as well as the formation of new holes, are performed on this the scalar function. The shape of the geometric boundary is modified by controlling the motion of the level set according to the physical problem and optimization conditions [48]. It is also important to note here that while a smooth boundary representation is realized in the design domain as shown in Figure 33, most level-set formulations rely on finite elements. Thus, boundaries are still represented by a discretized, likely unsMOOTH, mesh in the analysis domain unless alternative techniques are utilized to represent the geometry in the analysis model, for example extended finite elements [49].

Level sets for moving interface problems in physics were first developed by Osher and Sethian [50] with the fundamental goal of tracking the motion of curves and surfaces and have since been applied in a wide variety of research areas [51, 52]. The level set method was first applied to topology optimization in the early 2000s by Sethian and Wiegmann [53], where it was used to capture the free boundary of a structure in linear elasticity, and Osher and Santosa [54], who combined level sets with a shape sensitivity analysis framework for optimization of structural frequencies.

The modern level set method [56] begins with a structural boundary specified as a level set in implicit form as an iso-surface of a scalar function in 3D as Equation (19)

$$S = \{x : \Phi(x) = k\} \quad (19)$$

where  $k$  is the iso-value and is arbitrary, and  $x$  is a point in space on the iso-surface. Structural optimization can be performed by letting the level set model vary in time, yielding Equation (20).

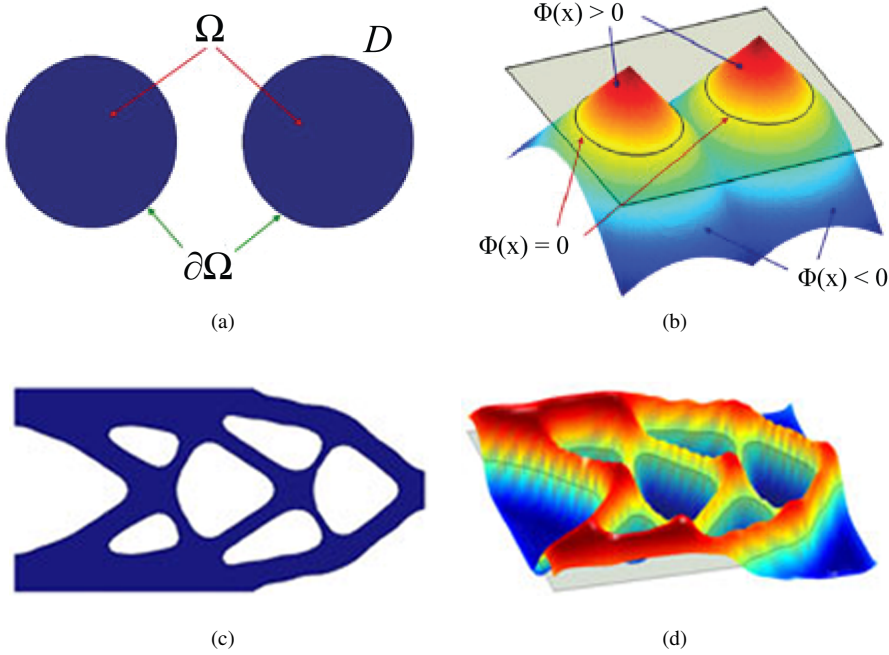


Figure 33: Level set representations: (a,c) 2D topologies and their (b,d) corresponding level set functions (from [55]).

$$S(t) = \{x(t) : \Phi(x(t), t) = k\} \quad (20)$$

Taking the time derivative of Equation (20) and applying the chain rule yields the following Hamilton-Jacobi equation

$$\frac{\partial \Phi(x, t)}{\partial t} + \nabla \Phi(x, t) \frac{dx}{dt} = 0, \quad \Phi(x, 0) = \Phi_0(x) \quad (21)$$

which defines an initial value problem for the time dependent function  $\Phi$ . In the solution process, let  $dx/dt$  be the movement of a point driven by the objective of optimization such that it can be expressed in terms of the position of  $x$  and the geometry of the surface at that point. The optimal structural boundary then becomes a solution of a partial differential equation on  $\Phi$  given by Equation (22)

$$\frac{\partial \Phi(x)}{\partial t} = -\nabla \Phi(x) \frac{dx}{dt} \equiv -\nabla \Phi(x) \Gamma(x, \Phi), \quad \Phi(x, 0) = \Phi_0(x) \quad (22)$$

where  $\Gamma(x, \Phi)$  is the “speed vector” of the level set and depends on the objective of optimization. This vector is obtained as the steepest descent direction of the objective obtained via analytical sensitivity analysis.

The level set method has obvious advantages over density methods because intermediate density material is not utilized in the design domain. However, one drawback of current level set formations is their dependency on the initial design, which is more severe than other methods. However, new developments have made strides to improve this

deficiency [57]. Also, level set methods also require reinitialization during the process when the level set function becomes too flat or too steep, which adds non-desirable computational complexity and additional tuning parameters to the algorithms.

**Phase Field Method** The phase-field method for topology optimization is based on theories originally developed as a way to represent the surface dynamics of phase-transition phenomena such as solid-liquid transitions [58]. The methods have also been utilized in a number of different surface dynamics simulations, especially in materials science, including diffusion, solidification, crack-propagation, and multiphase flow. In these theories, a phase field function  $\phi$  is specified over the design domain  $\Omega$  that is composed of two phases, A and B, which are represented by values  $\alpha$  and  $\beta$  of  $\phi$ , respectively, as shown in Figure 34. The boundary region between phases is a continuously varying region of thin finite thickness  $\xi$ .

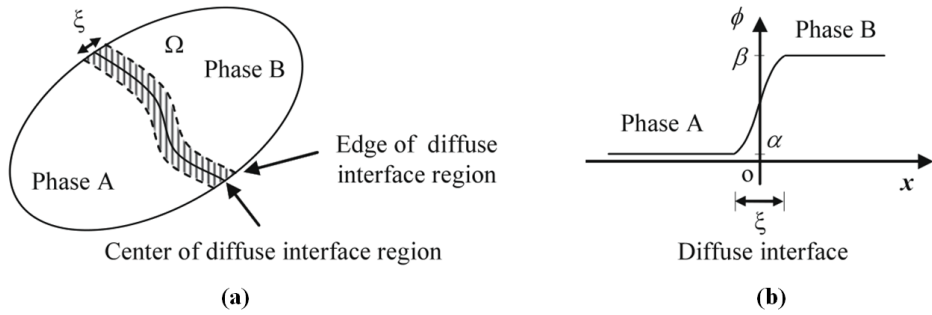


Figure 34: (a) A 2D domain represented by the phase field function and (b) a 1D illustration of the phase field function (from [59]).

In phase-field topology optimization [59, 60, 61] this region defines structural boundaries and is modified via dynamic evolution of the phase field function  $\phi$ . A primary difference between the level set and phase-field methods lies in the fact that in the phase-field method the boundary interface between phases is not tracked throughout optimization as is done when using level sets. That is, the governing equations of phase transition are solved over the complete design domain without prior information about the location of the phase interface. In addition, phase-field methods do not require the reinitialization step of level set functions.

### 3.2.5 A Biologically-inspired Method

One of the most recent methods for topology optimization is an innovative *biologically-inspired layout technique* that is capable of generating both discrete and continuum-like structures [62]. In this method, which is based on the cellular division processes of living organisms, topological layout is implicitly governed by a developmental program that when executed completes a sequence of tasks that develop the topology in stages. When driven by a genetic algorithm (GA), the set of rules, called a Lindenmayer or map-L system [63], that defines the tasks of the developmental program

become the design variables in the optimization problem. With control over these developmental rules, a diverse set of topological designs can be generated with relatively few design variables.

The key to this method is the *L* system, which is a type of grammar system originally introduced by biologist Aristid Lindenmayer to model the branched topology in plants. A map is defined as finite set of regions with each region bounded by a sequence of edges that intersect at vertices. The maps are analogous to cellular layers, where the regions represent the cells and the edges their walls. By using a series of production rules, an example of which is given in Equation (23), which govern the processes that construct the map, interpretations of complex topology can be obtained.

$$\begin{aligned}
 A &\rightarrow B[+A]x[-A]B \\
 B &\rightarrow A \\
 x &\rightarrow x
 \end{aligned} \tag{23}$$

Execution of the production rules in Equation (23) and the axiom  $\omega = ABAB$ , which indicates the initial edge labeling, for the first four steps in the process are shown by Figure 35.

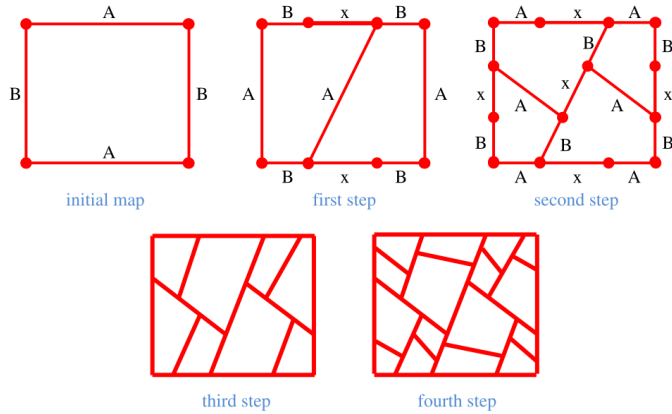


Figure 35: First four steps in a cellular division process (from [64]).

By utilizing additional rules apart from the simple division process demonstrated in the figure, more complex features, for example adding radii to edges, can be obtained. In addition, the geometry can be superimposed or stretched onto non-rectangular domains that can also change shape. It is also important to note that the topological layout generated by the map-*L* system in itself has no physical or structural meaning attached to it. Thus, the geometry must be interpreted into structural elements, which can often be done in a pre-processing step to a finite element analysis.

### 3.3 Literature Formulations & Applications

Topology optimization has been the most active area of research in structural optimization with the number of applications using various methods exploding over the last decade. However, the vast majority of topology optimization applications have been restricted to mechanical design problems concerning stiffness-based design criteria [65, 66]. The following subsections include a review of the most common topology optimization problem in addition to alternative and multiphysics topics that are relevant to the work demonstrated and proposed in the remainder of this document.

#### 3.3.1 Minimum Compliance

A well behaved topology optimization problem is best obtained when its objective function is computed as the integral over the designable domain. For purely structural problems, a convenient objective of this form is to minimize the compliance subject to volume constraint. For linear structures, this corresponds to determining the optimal stiffness tensor  $E_{ijkl}(x)$ , which is assumed to vary spatially. The statement of the minimum compliance problem follows [28].

Introducing the energy bilinear form (i.e., the internal virtual work of an elastic body at the equilibrium  $u$  and for an arbitrary virtual displacement  $v$ )

$$a(u, v) = \int_{\Omega} E_{ijkl}(x) \varepsilon_{ij}(u) \varepsilon_{kl}(v) d\Omega, \quad (24)$$

with linearized strains

$$\varepsilon_{ij}(u) = \frac{1}{2} \left( \frac{\partial u_i}{\partial x_j} + \frac{\partial u_j}{\partial x_i} \right), \quad (25)$$

and the load linear form

$$c(u) = \int_{\Omega} f u d\Omega + \int_{\Gamma} t u d\Gamma, \quad (26)$$

the minimum compliance problem takes the form

$$\begin{aligned} \min_{u \in U, E} : & c(u) \\ \text{subject to : } & a_E(u, v) = l(v), \text{ for all } v \in U. \end{aligned} \quad (27)$$

Here, the equilibrium equation is written in its weak, variational form, with  $U$  denoting the space of kinematically admissible displacement fields,  $f$  are the body forces, and  $t$  the boundary tractions.

Solution of the problem defined in (27) by any of the topology optimization methods discussed previously yields a structural topology characterized by maximum global stiffness. Most often, (27) is discretized by finite elements and thus fits the general topology optimization problem statement given previously in Equation (10). It may be con-

servatively estimated that greater than 85% of topology optimization work is related to solving this problem. This widespread acceptance is due in large part to two characteristics of the compliance objective: (i) it is self-adjoint and (ii) its sensitivity to material addition is strictly negative. These beneficial characteristics make the problem particularly easy to implement and solve. In engineering practice, the implementation of this problem setup in commercial packages has proven widely successful for purely mechanical applications.

### 3.3.2 Thermoelastic Structures

In most implementations of compliance-based topology optimization, the body force term in Equation (27) is neglected such that the design problem depends only on externally applied, design independent forces. Rodrigues and Hernandes [67] first retained this term by including the effects of a temperature difference in the compliance formulation using the homogenization method of [31]. Using homogenization parameters  $\mu$  and  $\theta$ , the compliance objective takes the form

$$\min_{(0 \leq \mu(\mathbf{x}) \leq 1, \theta(\mathbf{x}))} : \int_{\Omega} bud\Omega + \int_{\Omega} \beta_{ij}^H(\mu, \theta) \varepsilon_{ij}(u) \Delta T + \int_{\Gamma} tud\Gamma \quad (28)$$

where we note that both the elastic modulus and the coefficient of thermal expansion have been made functions of  $\mu$  and  $\theta$  by  $\beta_{ij} = E_{ijkl} \alpha_{kl}$ . The problem is subjected to the isoperimetric volume constraint

$$\int_{\Omega} \mu(\mathbf{x}) d\Omega \leq \bar{V} \quad (29)$$

where  $\bar{V}$  is the allowable amount of volume. One observation from this paper is the dependence of topological results upon the magnitude of the prescribed temperature difference. Figure 36 shows results from [67] for the minimum compliance problem of a simple 2D structure subjected to both an externally applied point load and a uniform temperature difference  $\Delta T$ . We observe that as the uniform temperature is increased, the resulting topology begins to differ. In addition, as temperature is increased, the compliance of the designs also increases. This is driven by the design dependency of the temperature load contribution in the objective function (28).

In fact, it was also observed in [67] that for higher temperatures, not all of the available material is utilized. This behavior is consistent with both observations in Chapter 2 of this document, where it was observed that material addition may increase the severity of some structural responses, in addition to more recent topology optimization work using the level set method [68]. In the case of minimum compliance topology optimization, depending on the level of temperature loading, adding material may increase compliance.

Jog [69] extended the compliance objective function in (28) to the general case of nonlinear thermoelasticity using a density-method with linear penalization and a perimeter constraint for regularization. It was also noted that the compliance objective function would not reduce peak stresses because in the presence of thermal loading stress is not

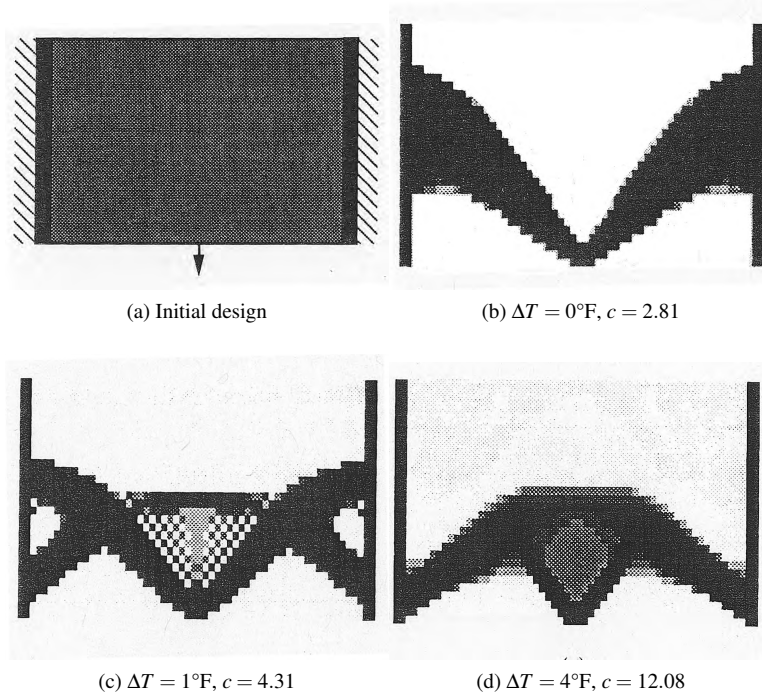


Figure 36: Minimum compliance results from Rodrigues and Hernandes [67] for various magnitudes of temperature loading.

proportional to strain. It is suggested that to do so, another functional would be required that would yield a more uniform (magnitude wise) stress distribution in the structure. Along these lines, recently Pedersen and Pedersen [70] proposed an alternative problem based on recursive iteration to obtain uniform energy density. They properly argue that compliance is a questionable objective for thermoelastic problems, but due so under the incorrect assertion that “with less material that will improve the compliance the strength will normally not be as desirable, i.e., the maximum von Mises stress is increased” and furthermore argue that it is beneficial for strength design to fully utilize all available material. As was clearly demonstrated in Chapter 2, this is not true in many cases. This aspect was not investigated in the paper; as benchmark problems were used to simply demonstrate the effectiveness of the recursive scheme for obtaining a topology. The resulting topologies were not objectively evaluated from a design point of view. In a later publication, this work was expanded by its authors to 3D domains with alternative interpolation schemes [71].

In many of the topology optimization results reported in the previous publications using both homogenization and density-based methods, large regions of intermediate gray material are evident. In fact, these regions are difficult to physically realize in problems of practical importance. In the minimum compliance problem, the material usage constraint in the general formulation must be active to force a crisp black/white design. Thus, without special treatment, it is impossible to ensure that the optimal topology will not contain gray material when using the homogenization or any density-based approach. Gao and Zhang recently investigated this issue and demonstrated that in some cases the

RAMP interpolation scheme was able to alleviate many of the issues related to the formation of gray material when compared to the SIMP scheme [72]. This was attributed to fact that the RAMP interpolation, unlike SIMP, has nonzero sensitivity at zero density as was previously shown in Figure 27. Figure 37 demonstrates the alleviation of gray material by using RAMP for a benchmark problem from [72]. While this prescription seems effective in the cases presented in the paper, additional numerical tests seem to indicate that while RAMP does provide improved performance, it is not guaranteed to alleviate all gray material many objectives. This problem appears much more dependent upon the relative magnitude of mechanical and thermal loading rather than the interpolation scheme that is utilized.

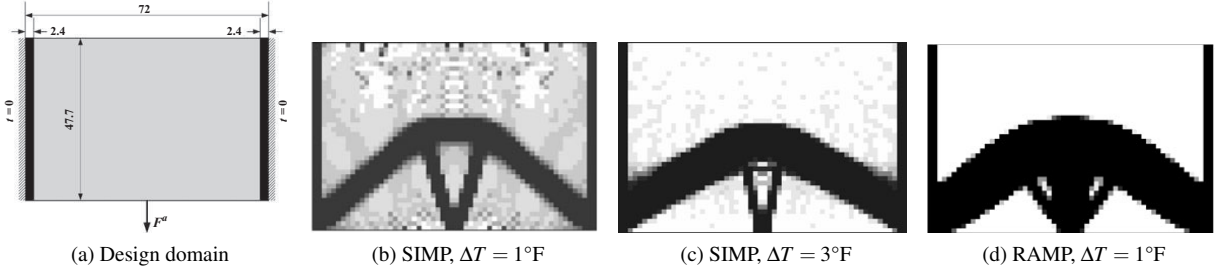


Figure 37: Thermoelastic minimum compliance results from Gao and Zhang [72] where SIMP methods exhibit gray material that is eliminated when using RAMP.

Li et al. demonstrate a variety of thermoelastic topology optimization problems using the ESO method including design of shell structures [73] and displacement minimization [74]. More recently, Kim et al. used ESO for the design of thermal protection system (TPS) panels for both thermal stress and frequency criteria [75]. It is of merit to note that in their results, intermediate material is not an issue due to the discrete nature of the ESO method, but its heuristic operation and inability to conveniently handle multiple constraints make it an unattractive option for the scope of problems pursued in the proposed work.

In recent years, successful applications of topology optimization with thermal loading in the literature have relied on problems apart from the usual minimum compliance formulation or specific procedures to generate good designs for specific problems of interest. Wang et al. [76] proposed a bi-objective problem for designing thermoelastic structures that have both high stiffness and low thermal expansion in particular directions. The problem statement takes the form:

$$\begin{aligned}
 \min : \quad & F(\mathbf{x}) = wF_1(\mathbf{x}) + (1-w)F_2(\mathbf{x}) \\
 \text{subject to :} \quad & \text{material usage constraints} \\
 & \mathbf{KU}^S = \mathbf{F}^S \\
 & \mathbf{KU}^{Tem} = \mathbf{F}^{Tem}
 \end{aligned} \tag{30}$$

where a simple multi-objective setup is utilized with  $w$  being a weight factor between 0 and 1. We note the presence

of two finite element systems denoted by superscripts  $S$  and  $Tem$ , which correspond to cases of purely structural and purely temperature load, respectively. The first objective in the problem is taken as the compliance of the structure subjected to only structural loading given by

$$F_1(\mathbf{x}) = \frac{(\mathbf{F}^S)^T \mathbf{U}^S}{(\mathbf{F}_0^S)^T \mathbf{U}_0^S} \quad (31)$$

where  $(\mathbf{F}_0^S)^T \mathbf{U}_0^S$  is the compliance of the initial design and is simply used for normalization. The second objective consists of the magnitude of the summation of nodal displacement components for which displacement should be minimized and is given by

$$F_2(\mathbf{x}) = \frac{\sum_{i=1}^n \left( u_{\lambda(i)}^{Tem} \right)^2}{\sum_{i=1}^n \left( \left( u_{\lambda(i)}^{Tem} \right)_0 \right)^2} \quad (32)$$

where again the term in the denominator is the response at the initial design for normalization. By using the displacement vector from the purely temperature loaded analysis, and selecting degrees of freedom corresponding globally to a particular direction, this objective serves to reduce the thermal expansion of the structure in that direction. A similar formulation was demonstrated by Deng et al. [77] who utilized homogeneous and periodic microstructure design rather than the bi-material formulation of [76].

Yang and Li included temperature loading into the topology optimization for minimum dynamic compliance of bi-material plates [78]. In their implementation, the thermal stress distribution in the structure is first computed via static analysis with a prescribed uniform temperature field. This thermal stress is then taken as a pre-stress by formulating the corresponding differential stiffness and including it in a subsequent transient dynamic analysis with harmonic loading at specified frequencies. Later, they modified the algorithm to include a normal modes analysis, which also includes differential stiffness terms due to thermal stress, to compute resonant frequencies. The dynamic analysis is then performed at frequencies corresponding to resonance behavior [79]. In a more advanced implementation Stanford and Beran used a similar prescription to include the effects of temperature loading in the topology optimization of plates for buckling and flutter speed [80].

Finally in an early yet interesting application, Sigmund and Torquato utilized topology optimization to develop material microstructures with extremal thermal expansion properties [81]. That is, the microstructures developed exhibited large directional expansion, zero isotropic expansion, and even negative isotropic expansion at the macro-scale.

### 3.3.3 Heat Transfer

Topology optimization techniques have also been applied to a number of generalized scalar field problems including heat transfer. In fact, for the simplest case of steady-state heat conduction, it is straightforward to formulate a design problem that is analogous to minimum structural compliance. For a given design domain  $\Omega$ , the steady-state heat

equation with homogeneous boundary conditions is given by

$$\begin{aligned}
 \nabla \cdot (k \nabla T) + f &= 0 \text{ in } \Omega \\
 T &= 0 \text{ on } \Gamma_D \\
 (k \nabla T) \cdot \mathbf{n} &= 0 \text{ on } \Gamma_N
 \end{aligned} \tag{33}$$

where  $T$  is the temperature,  $k$  is the heat conduction coefficient,  $f$  a volumetric heat source,  $\mathbf{n}$  an outward normal unit vector, and  $\Gamma_D$  and  $\Gamma_N$  surfaces upon which Dirichlet and Neumann boundary conditions are applied, respectively. Upon investigation, it becomes obvious that the temperature and volumetric heat source are analogous to displacement and mechanical forces, respectively, in structural mechanics, and the mechanical compliance inspired objective can be conveniently stated as

$$\int_{\Omega} f T d\Omega. \tag{34}$$

Minimizing this functional by varying the conductivity under a material usage constraint physically corresponds to finding the optimal conductivity distribution that produces the least heat when the amount of high conductivity material is limited. This formulation, or slight variations of it, have been extensively studied in the literature (likely due to its well-posed nature like the mechanical compliance formulation) and are claimed to represent the design of an optimal conductive device. It has been demonstrated using density methods (using both finite element [28] and finite difference [82] solution schemes), ESO [83, 84, 85], and level-sets [86, 87]. An example of a problem of this class is given in Figure 38. The branched conduction paths to the fixed temperature sink are characteristic of the results obtained using all of the different methods.

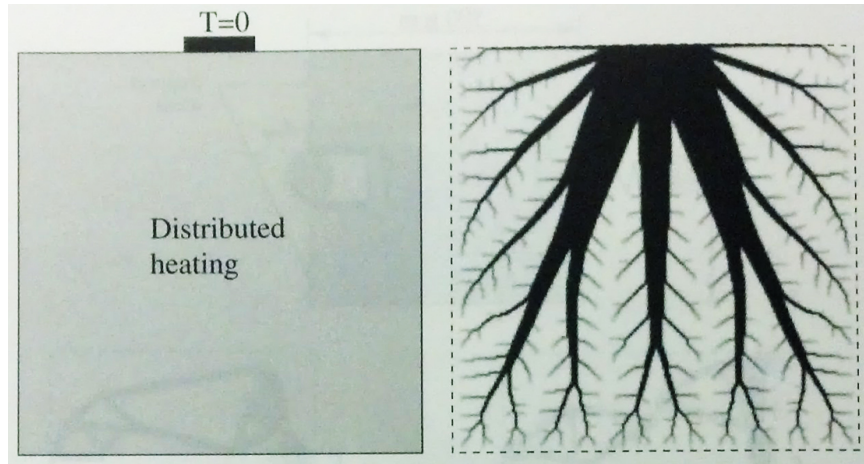


Figure 38: Topology optimization for an optimal heat conductor. The design domain has adiabatic boundaries all around and is subjected to uniform volumetric heat generation and the temperature condition shown. (from [28])

Of much greater interest than the simple heat conduction literature is the work by Bruns [88] who introduced the

physics of free convection for density-based topology optimization. Mathematically, this corresponds to allowing the boundary conditions of the problem in Equation (33) to become non-homogeneous as given by

$$(k\nabla T) \cdot \mathbf{n} = h(T - T_\infty) \text{ on } \Gamma_h \quad (35)$$

where  $h$  is the convective film coefficient,  $T_\infty$  is the ambient temperature, and  $\Gamma_h$  are the surfaces upon which convection acts. In topology optimization, applying these conditions is challenging because the structural geometry, including the convection surfaces, constantly varies. To overcome this, Bruns demonstrated that with a finite element-based implementation, the convection conditions can be applied to all elements, including both the faces and edges of 2D elements and all faces of 3D elements. After doing so, both the conductivity  $k$  and convective film coefficient  $h$  are parameterized according to density design variables via interpolation schemes. With this implementation, the convection boundary conditions can be continuously varied from states of existence or absence according to the state of surrounding elements. Bruns also notes that special treatment is required to prevent numerical instabilities at the boundaries between regions of high and low conductivity elements in the presence of convection effects. An example of this phenomena is shown in Figure 39. In Figure 39a, the finite element model of a cooling fin is shown with black elements representing the high conductivity solid material and white elements representing low conductivity void regions where  $k_2 \ll k_1$ . This representation of the domain is consistent with that found during topology optimization. The entire domain is subjected to uniform surface convection to an ambient temperature of 0.0 and a heat flux boundary is applied to the left edge of the solid fin region.

Figure 39b shows the temperature contour plot of the fin examined by FEA using the usual *consistent* formulation of convection matrices. Note that the temperature denoted in the black region falls below the ambient fluid temperature. The nonphysical oscillations are quite apparent in the temperature profiles plotted at discrete intervals along the fin length in Figure 39d. By using a *lumped* form of the convection matrices, these oscillations are removed in the results as indicated in Figures 39c 39e. In similar work, Iga et. al. also included the effects of design dependent convection using a homogenization approach, but employed a computationally challenging boundary searching algorithm [89]. We also note that in these works, the motion of fluid in the void region is not modeled and convection. Doing so would require the solution of different governing equations in the solid and void regions and an improved representation of the boundary. While algorithms that are capable of doing this do exist, they are very much in their infancy in the literature [65]. Thus, for practical purposes the representation of convection can only be done as a flux-type boundary condition.

Finally, it is of merit to note that while the effects of radiation to or from an ambient condition is possible using formulation similar to the treatment of convection in [88], no instances of radiation within cavities or enclosures are found in the topology optimization literature. Doing so would likely require a discrete method for topology

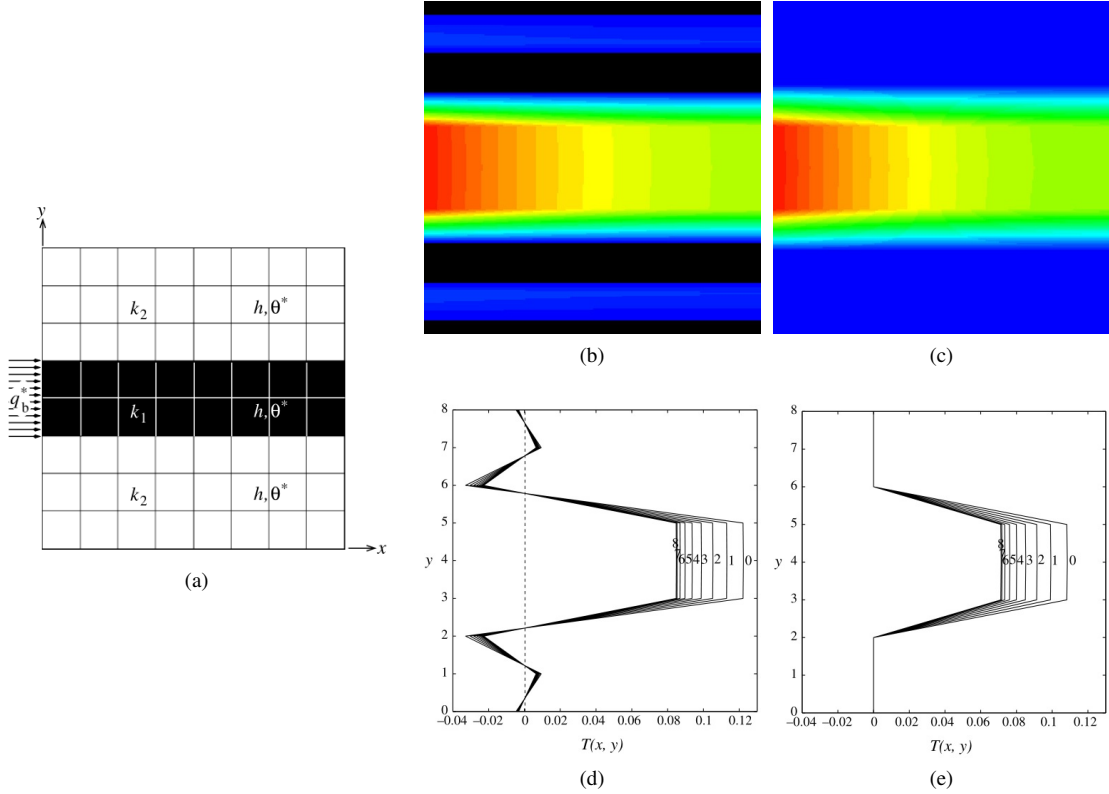


Figure 39: (a) Cooling fin embedded in a fixed domain. Temperature contour plots of the fin by FEA using (b) consistent and (c) lumped convection matrices. Corresponding temperature response profile plots along the length of the the fin for (d) consistent and (e) lumped convection matrices.

optimization to properly identify the cavities formed inside the design domain. Computing the necessary view factors would also likely be extremely computationally expensive because the number and shape of radiation cavities would change every design iteration.

### 3.3.4 Coupled Thermal-Structures

With examples of thermoelastic topology optimization with prescribed temperature loading and topology optimization of heat transfer problems that yield a temperature distribution, a natural extension is to combine the two. In [90], Cho and Choi formulate such a method using coupled adjoint sensitivities to account for the dependence of temperature loading in the structural analysis on the results of a heat transfer analysis. Li et. al. also demonstrate the coupled solution using the ESO method where coupled sensitivity numbers are derived to drive the evolutionary optimization process [91, 92]. The concept of combining heat transfer and structural topology optimization as is done in these works lends itself well to the design of exhaust-washed structures. With such a capability, topologies may be obtained with efficient conduction pathways and convective cooling to reduce their overall temperature levels. This would lead to reduced thermal expansion and thermal stresses, perhaps with more effect than any pure structurally motivated

modification.

A more common application of a coupled thermal-structural topology optimization is the design of thermally compliant mechanisms or microactuators. These components are microscale structures whose thermal expansion characteristics are designed to produce controllable actuation forces or displacement at a particular location. Formulations for density-based topology optimization of these components for one material and two material systems are detailed by Sigmund [93, 94]. An example from [93] is given in Figure 40. Here, the design problem is to find the optimal topology in the designable region that when subjected to an elevated temperature maximizes the work done in the spring. We see that for different stiffness springs, alternative topologies are developed that provide different magnitudes of force and displacement. Other examples are also given in the articles where topology is obtained that directly drives the displacement of a control point or causes its location to pass through prescribed way-points for different temperature loads.

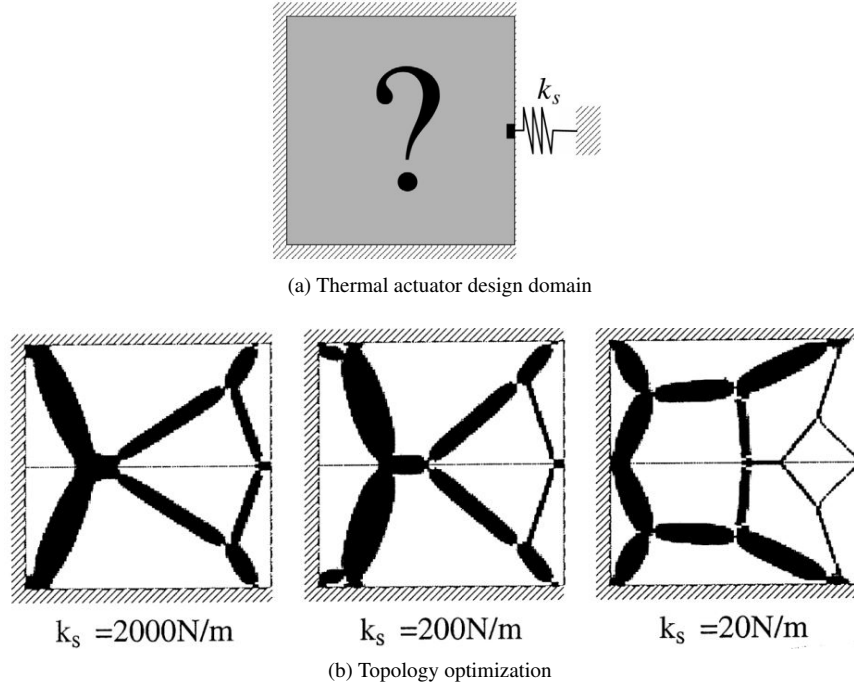


Figure 40: (a) Initial design domain for a thermally actuated compliant mechanism along with (b) optimal topologies.

In recent years, similar problems related to thermal microactuator design have been performed using the ESO method [95] and level sets [96]. Time transient effects in heat-transfer analysis have also been considered in the topology optimization for the homogenization of thermally actuated snap-fit mechanisms [97]. In this application, elevated temperature causes thermal expansion in such a way so as to release fixity between components, which provides for rapid disassembly of recyclable components.

### 3.3.5 Stress-based Topology Optimization

Ultimately, identifying how to reduce excessive thermal stresses is the most important consideration in most thermal structures design problems. To investigate the feasibility of directly addressing this consideration, the literature related to structural topology optimization using stress-based design criteria is now surveyed.

The treatment of stresses in topology optimization for continuum structures was first investigated in the late 1990s by Duysinx and Bendsøe [98]. Since then, three primary challenges related to the introduction of stress-criteria in topology optimization have been identified. These are (i) the so called “singularity” phenomenon, (ii) the highly non-linear behavior of stresses with topology variation, and (iii) the local nature of stresses [28]. After early investigations, stress-based criteria were seemingly abandoned in favor of the well-posed compliance problems in topology optimization literature. However, in the last 4-5 years, stress considerations have enjoyed a resurgence and are currently one of the most active research areas in the field. In addition, a much more conventional structural optimization problem formulation based on minimizing material usage subject to stress constraints in the domain has been adopted in stress-based publications.

The “singularity” problem relates to the fact that an  $n$ -dimensional feasible design space contains degenerate subspaces of dimension less than  $n$  [99], that is, where some of the  $n$  design variables vanish from the problem. Further, the globally optimal design often lies in one of these degenerate subspaces. This is evidenced, for example, in density-based topology optimization for minimum compliance where a majority of elements have density design variable values equal to zero. However, for a number of design responses, asymptotic behavior as variables approach zero prevent a nonlinear programming algorithm from reaching the degenerate subspaces and leads to convergence to undesirable local minima. This occurs in density-based topology optimization where local element stresses increase without bound as density design variables approach zero. When constraints are placed on an element stress, it then becomes impossible to fully remove that element from the design domain because of constraint violations. This problem was first addressed using an  $\varepsilon$ -relaxation [98], which is derived from an analogous problem in truss optimization where the stress in a truss element (given simply by  $\sigma = P/A$ ) becomes singular as the cross-section area nears zero [100]. In general, a stress constraint in topology optimization may be written as

$$g(\rho) = \sigma(\rho) \leq \bar{\sigma} \text{ for } \rho > 0 \quad (36)$$

where  $\sigma$  is an elemental stress measure (for example, von Mises stress),  $\bar{\sigma}$  is the allowable stress, and the condition  $\rho > 0$  indicates the existence of the element. To eliminate the condition  $\rho > 0$  from the constraint, the following modified formulation is considered

$$g(\rho) = \rho \left( \frac{\sigma(\rho)}{\bar{\sigma}} - 1 \right) \leq 0. \quad (37)$$

Also, to prevent singularity using  $\varepsilon$ -relaxation, the constraint is replaced by

$$g(\rho) = \rho \left( \frac{\sigma(\rho)}{\bar{\sigma}} - 1 \right) \leq \varepsilon \quad (38)$$

where the  $\varepsilon$  parameter is given. For  $\varepsilon = 0$ , the original problem with stress constraints arises; however, for any  $\varepsilon > 0$ , the  $\varepsilon$ -relaxed problem is characterized by a design space that is no longer degenerate, that is, the optima are now placed in regions of the design space with a non-zero constraint measure and it becomes possible to reach them using the usual structural optimization algorithms based on the Karush-Kuhn-Tucker (KKT) conditions. To return the problem to its original form, a continuation approach is used to gradually reduce the value of  $\varepsilon$  during the optimization process as described in [98]. More recently, variants of this approach have been applied successfully by other authors [101, 102, 103, 104, 105, 106].

Recently, Le et. al. [107] introduced another method to address the singularity phenomena by simply penalizing the stress measure with an interpolation function. Using the stress interpolation function  $\eta_\sigma(\rho)$ , the stress constraint can be relaxed as

$$g(\rho) = \eta_\sigma(\rho) \sigma(\rho) \leq \sigma_{all} \quad (39)$$

where the relaxed stress is  $\sigma_r(\rho) = \eta_\sigma(\rho) \sigma(\rho)$ . In the paper, it is demonstrated that by using a SIMP interpolation (i.e.  $\eta = \rho^p$ ) and appropriate selection of penalization parameters for interpolation of stress, stiffness, and volume, degenerate regions of the design space can be reached efficiently. In their work, SIMP parameters of 1/2, 3, and 1 are suggested for stress, stiffness, and volume, respectively, but also note other selections that satisfy a set of necessary criteria are viable.

The highly nonlinear nature of stress constraints occurs because of the high sensitivity of elemental stress values to surrounding variations in topology. This is addressed by ensuring that sensitivity information that is given to the optimization algorithm is numerically consistent with the design problem that is being solved. In [107] it is advised that when applying filtering that only numerically consistent schemes should be employed, such as the density and Heaviside filters, and that those that smear sensitivity information, such as the sensitivity filter should be avoided.

The local nature of stress constraints is the focus of much of the stress-based topology optimization literature in the past 5 years. In a design problem, stresses should satisfy limits at every point in the structure. In sizing and shape optimization, this is easily accomplished using intuition to enforce constraints in critical locations (i.e. in critical elements) based on the geometry of the structure or by using active-set strategies to dynamically select critical stresses throughout the optimization process. However, in topology optimization, it is impossible to identify which elements will have critical stress because the geometrical configuration is not initially known. Thus, a potential solution is to

place stress constraints on all elements  $e$  such that

$$g_e(\rho) = \sigma_e(\rho) \leq \bar{\sigma} \text{ for } e = 1, 2, \dots, n. \quad (40)$$

While this prescription, known as the *local* method, has been demonstrated in the literature [28, 101, 102, 104], it is not applicable in practical implementation (problems with  $> 10,000$  elements and multiple load cases) because the computation of local sensitivities by either the direct or adjoint method is computationally prohibitive. Reducing the computational cost corresponds to reducing the number of constraints and upon first consideration an attractive option is to collect the element stresses into a single maximum stress constraint as:

$$g(\rho) = \max_{e=1..n} (\sigma_e(\rho)) \leq \bar{\sigma}. \quad (41)$$

However, the *maximum* operator is not differentiable, which prevents the derivation of analytical sensitivities, and must be smoothed. For this purpose, continuous aggregation functions have been adopted in the literature [28, 105, 106, 108, 109] to combine the local stresses into a single quantity. These techniques are known as *global* methods and variations of the *Kresselmeier-Steinhauser* (KS) function given by

$$\sigma_{KS} = \frac{1}{p} \ln \left[ \sum_{e=1}^{N_e} \exp \left( \frac{F(\sigma_e)}{\bar{\sigma}} \right) \right] \quad (42)$$

or a basic  $p$ -norm measure

$$\sigma_{PN} = \left[ \sum_{e=1}^{N_e} \left( \frac{F(\sigma_e)}{\bar{\sigma}} \right)^p \right]^{1/p} \quad (43)$$

are commonly utilized. A drawback to using a *global* method is that the aggregation functions serve as only an approximation to the maximum value in a set and the quality of the approximation generally degrades as the set size is increased. As a result, in an optimization setting, while the global formulations streamline the problem, they cannot guarantee that the maximum stresses are maintained locally.

Recently, a number of researchers have investigated so called *regional* (also called *block* or *clustered*) stress measures [107, 110, 111, 112]. These techniques operate identically to *global* measures using aggregation functions, but rather than grouping the entire global domain, they aggregate multiple regions that canvas the entire domain. This results in multiple regionalized constraints that operate on sets of reduced size, and thus benefit from better approximation, at a fraction of the computational expense of local methods (tens of constraints versus tens or hundreds of thousands). A visual comparison of the local, global, and regionalized/block methods for stress constraints is given in Figure 41.

Building on the basic regional methods, a number of researchers have proposed techniques to further improve the

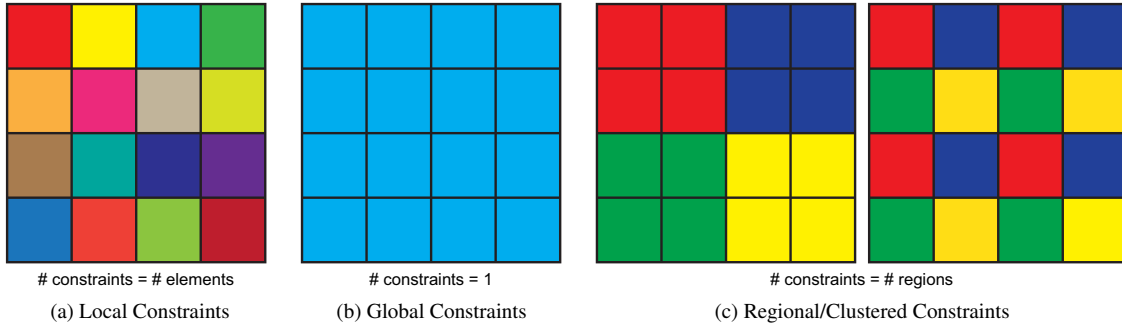


Figure 41: Three methods to apply stress constraints in structural topology optimization.

approximation of stress constraints with respect to the actual local values. In [107], maximum stress information from previous design iterations is used to scale stresses at the current iteration, [112] adaptively sorts the sets of elements to improve the accuracy of each regional measure, and [113] treats potentially active and non-active local constraints separately while updating aggregation metrics throughout optimization. In each of these works, their adaptive mechanisms actually modify the basic optimization problem at various points. As a result, an entirely new mathematical optimization problem is being solved after these variations occur, which can result in convergence difficulties for many optimization algorithms.

As previously noted, interest in stress-based criteria for topology optimization of late has been high. This has resulted in a number of applications using the methods described previously. Stress-based design criteria are found for functionally graded materials [114], Drucker-Prager stresses that account for different material strength in tension and compression [115], design-dependent self weight loads [116], cases of both compliance and stress [117], and even fatigue [118]. Boundary variation methods have also been demonstrated for stress-based topology optimization including both level set [119] [120] [121] [?] and phase field [122] methods.

### 3.4 Chapter Summary

From the preceding review, it is a clear that a variety of topology optimization methods exist in the literature, with the density-based formulations being the most common and most mature. Limited work related to the topology optimization of thermoelastic problems exists, but a widely accepted objective function and problem setup has yet to be identified as is observed with minimum compliance for mechanical problems. Ultimately, several works question the validity of compliance when considering thermal loads and remark that an alternative formulation is necessary. When considering the exhaust-washed structure design cases of interest in this document, we recall that thermal stresses are a primary design consideration. In the literature, methods to treat stress-based criteria have been developed for mechanical loading and may present an effective formulation for thermal structures; however, these techniques have yet to be explored for thermal stresses. Finally, the possibility of addressing the combined thermal-structural environment

with coupled heat transfer and structural analysis appears feasible based on literature examples. The method to do so can likely be inspired by the existing work related to the topology optimization of thermal microactuators.

In conclusion, it is evident that topology optimization may be an effective design tool for thermal structures design, but a suitable formulation for application to the problem of exhaust-washed structures design has yet to be developed. In the next chapters, research in the direction of this need is presented and later, future work is detailed to accomplish this task.

## 4 Thermoelastic Stiffening via Topology Optimization

Two unique applications are possible when considering the application of topology optimization to thermal structures and EEWs design problems. They are the design of stiffening concepts for a predefined structure, such as the B-2 aft deck, or a complete structural design of all material that is needed to support an exhaust-washed surface. In this chapter, the case of stiffening of an existing configuration is investigated.

### 4.1 Introduction

From the findings in Section 2.2.1, it is obvious that changing only the size of thermally loaded structures may not provide a suitable design solution for thermal stresses. While it was observed that reducing the thickness of a thin thermally restrained shell may decrease thermal stresses, this likely is not possible in practice due to the detrimental effect on other design criteria such as natural frequency. In this chapter, the application of *density-based* topology optimization techniques to stiffening thin structures subjected to restrained thermal expansion are investigated. First, the desired structural behavior for achieving a reduction in thermal stresses is demonstrated. Next, three formulations of topology optimization are presented. The first formulation is the basic minimum compliance formulation, which exhibits severe deficiencies in the design cases presented here. The second two formulations are developed with the specific goal of generating topological designs with desirable thermoelastic behavior. For ease of demonstration, a simple example case based on the beam strip geometry investigated previously is utilized to formulate the topology optimization problems.

#### 4.1.1 Displacement-stress Relationship

In Section 2.2.1, it was demonstrated that simply adding structural material in an attempt to stiffen a restrained thermal structure is not only ineffective, but can actually be detrimental to both the primary component and any structures it is affixed to. It was also identified that the tensile stresses in critical locations of the model are a result of the out-of-plane displacement of the structure. We now focus on the relationship between the magnitude of this displacement and the resulting stress levels to identify the necessary criteria of an effective stiffening technique.

Since the fully clamped edge scenario, or an infinite stiffness parameter  $k$ , seemed to place an upper bound on the detrimental effects of material addition, we select the fully clamped boundary condition with a thickness of  $t = 0.16$  inches, span of  $L = 12$  inches and curvature measure of  $\delta = 0.5$  inches (corresponding to radius of 144 inches). These parameters correspond to a thickness and curvature ratio of 0.0133 and 0.0417 for reference to geometry in Section 2.2.1. The thermal load is applied to the model by specifying  $E\alpha T = 60 \times 10^3$  and the equilibrium state is determined. A series of enforced displacement conditions are then imposed on the structure so as to incrementally return it to the undeformed state. At each step of this process the stress in the beam and the boundary reaction loads are measured

and plotted in Figures 42 and 43, respectively.

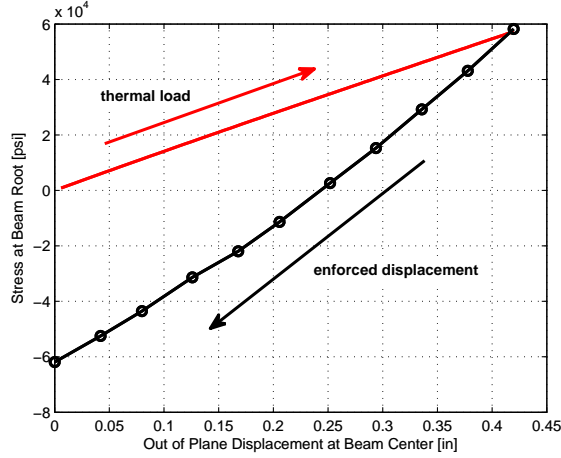


Figure 42: Stress at root of beam as a function of out-of-plane displacement at the center of beam strip.

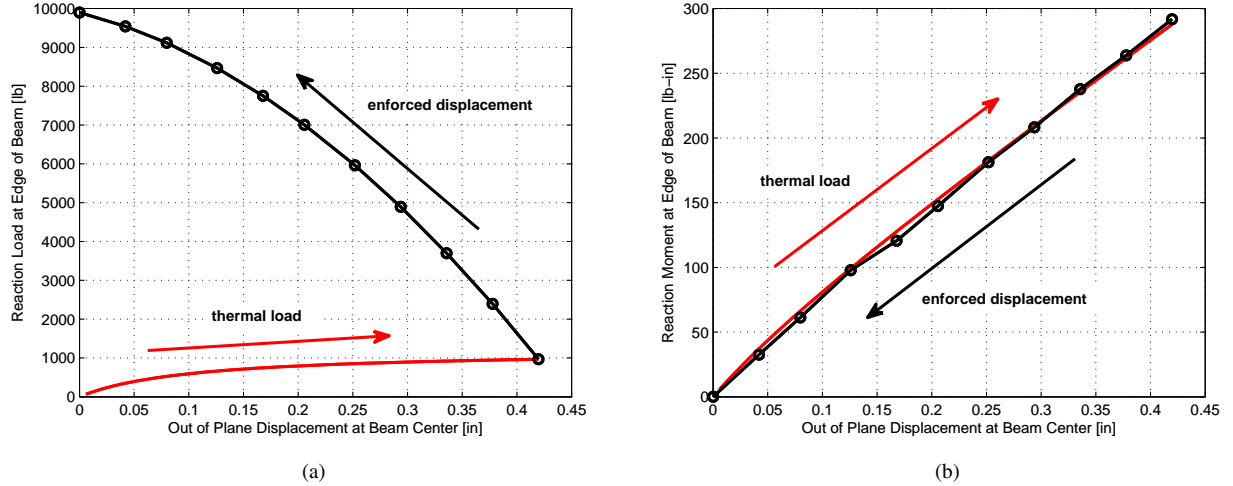


Figure 43: (a) Boundary reaction load in horizontal direction and (b) reaction moment as a function of out-of-plane displacement at the center of beam strip.

In the plots, the displacement is measured at the center of the curved strip model, which corresponds to the location of maximum out-of-plane displacement. From Figure 42, we observe that significant gains in stress reduction can be obtained by reducing the out-of-plane displacement. For example, from the deformed state with a center displacement of approximately 0.42 inches a 50% reduction in stress can be achieved by reducing the displacement to between 0.30 and 0.35 inches. Based on further investigations of varying geometry, this general observation can be extended to geometries with any curvature, thickness, and length in addition to responses at different stress levels. However, physically it is impossible to reduce the displacement as is done here, but through this exercise it is readily evident that one mechanism that can reduce thermal stresses induced by restrained thermal expansion is to reduce out-of-plane

deformation.

One challenge associated with attempting to reduce stress by displacement reduction is observed in Figure 43a. In this plot we note that reducing deformation increases the boundary reaction load significantly. This stems from the reorientation of the thermal loads generated via restrained expansion by the enforced displacement conditions. This reorientation can be thought of as a transition from significant bending effects at greater deformation to significant axial (or “in-plane” type) effects as deformation disappears. This behavior is supported by Figure 43b, which shows a reduction in reaction bending moment at the root of the strip as deformation is decreased. In a physical application, this increase in reaction loads corresponds directly to increases in shear loading into fasteners at structural joints and significantly higher loads that are exerted on adjoining sub- and supporting structures.

With these observations in mind, it becomes clear that to achieve the desired stress reduction without significant reaction increases, the design space must be expanded past modification of the properties of the thin structure itself, which in design optimization would be considered simple sizing optimization. Thus, the application of structural topology optimization is proposed to generate a stiffening structure that can simultaneously reduce stress in critical locations and limit reaction loading. Such a solution requires the satisfaction of several competing design criteria and managing both the amount and direction of thermal expansion within the structure.

#### 4.1.2 Functional Topology Design Space

Figure 44 shows a section of representative exhaust structure from which the beam strip in the previous demonstration was extracted. Here we see the beam strip structure subjected to thermal loading from hot exhaust gases and its fixivity to substructure. In this configuration, the underside of the exhaust-washed structure consists of open bays that are absent any obstructing substructure or other subsystems. Thus, it is assumed that in this region a stiffening structure can be designed that is affixed to the underside of the exhaust-washed structure to reduce thermal stresses. The proposed design domain for this case is shown in Figure 45.

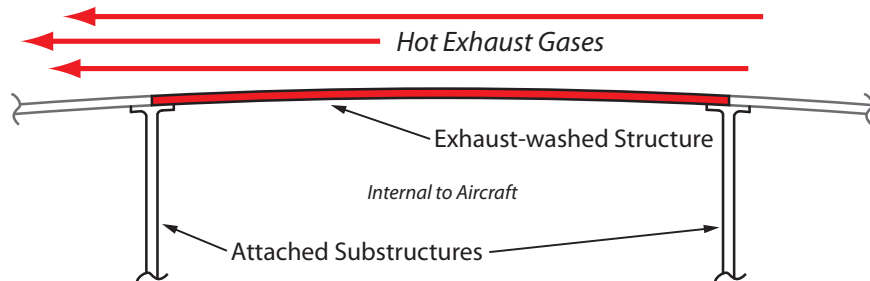


Figure 44: Two-dimensional schematic of exhaust-washed structure and substructure region.

This design concept can be envisioned in three-dimensions by referring to the EEWs concept configuration previously shown in Figure 4. In practice, any open region (or open internal bay) between the exhaust-washed nozzle surface

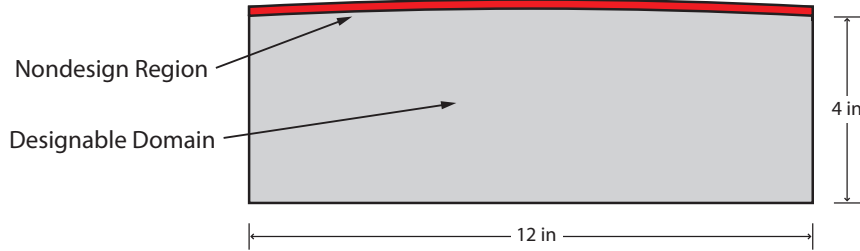


Figure 45: Topology optimization design space for stiffened strip example including designable and nondesign domains.

and the outer aircraft skins could be utilized as a topology design space in which to develop a stiffening structure. In fact, topology optimization could potentially be utilized to design all of the structure, including integral supporting and sub-structures, in this region with the appropriate design responses related to the overall aircraft configuration. In the following, we outline the topology optimization methods using the two-dimensional strip example. With the topology optimization design domain in mind, the computational details of the problem setup are first described for the proposed density-based methods.

## 4.2 Finite Element Parameterization

The density method for topology optimization is selected. Thus, the finite element system must first be parameterized to accommodate the density-based design variables applied on designable finite elements. Here we develop the parameterization based on a generalized thermoelastic design domain. This domain  $\Omega$  is shown for two dimensions in Figure 46 and contains fixed displacement boundary conditions, externally applied surface tractions, and a temperature change that may be uniform or spatially varying. The domain consists of regions of fixed void material, fixed solid material (non-designable), and designable areas whose topology is determined from optimization.

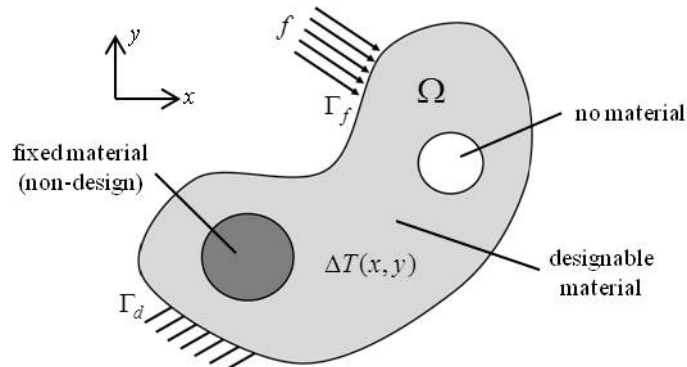


Figure 46: Generalized thermoelastic structural design domain.

The design domain is discretized using  $N$  finite elements with  $N_d$  designable and  $N_{nd}$  nondesign elements. Each

designable element is assigned a design variable  $x_e$  ranging from  $0 < x_e \leq 1$  with  $e = 1, 2, \dots, N_d$ . Together these variables form the design variable vector  $\mathbf{x}$ . Linear static equilibrium for a finite element representation of the domain, including both mechanical and temperature loading, is given by

$$\mathbf{K}(\mathbf{x})\mathbf{U} = \mathbf{F}(\mathbf{x}). \quad (44)$$

where  $\mathbf{K}(\mathbf{x})$  is the global stiffness matrix,  $\mathbf{U}$  is the nodal displacement vector, and  $\mathbf{F}(\mathbf{x})$  is the nodal load vector. Depending on the problem,  $\mathbf{F}$  consists of either design-independent mechanical loading  $\mathbf{F}^m$ , design-dependent thermal loads  $\mathbf{F}^{th}(\mathbf{x})$ , or a combination of both as

$$\mathbf{F}(\mathbf{x}) = \mathbf{F}^m + \mathbf{F}^{th}(\mathbf{x}). \quad (45)$$

The stiffness matrix  $\mathbf{K}(\mathbf{x})$  is assembled as the summation of element stiffnesses by

$$\mathbf{K}(\mathbf{x}) = \sum_{e=1}^{N_d} \mathbf{k}_e(x_e) \quad (46)$$

where

$$\mathbf{k}_e(x_e) = \int_{\Omega_e} \mathbf{B}_e^T \mathbf{C}_e(x_e) \mathbf{B}_e d\Omega. \quad (47)$$

Here,  $\mathbf{B}_e$  is the element strain-displacement matrix, which consists of derivatives of the element shape functions that are independent of topology design variables.  $\mathbf{C}_e$  is the element elasticity matrix, which for isotropic materials can be written as a linear function of elastic modulus as

$$\mathbf{C}_e(x_e) = E(x_e) \bar{\mathbf{C}}_e \quad (48)$$

where  $\bar{\mathbf{C}}_e$  consists of constant terms related to the material constitutive matrix and  $E(x_e)$  is the elastic modulus of element  $e$  that is dependent on design variables. For nondesign elements, the previous equations can be utilized by simply assuming  $x_e = 1$ . The mechanical load vector  $\mathbf{F}^m$  is assembled from externally applied forces on specific degrees of freedom, and the thermal load vector  $\mathbf{F}^{th}(\mathbf{x})$  is parameterized using the thermal stress coefficient (TSC) [67, 72] for topology optimization and described as follows.

The nodal load vector for a designable element  $e$  is given as

$$\mathbf{f}_e^{th}(x_e) = \int_{\Omega_e} \mathbf{B}_e^T \mathbf{C}_e(x_e) \boldsymbol{\varepsilon}_e^{th}(x_e) d\Omega. \quad (49)$$

$\boldsymbol{\varepsilon}_e^{th}(x_e)$  is the thermal strain vector for the element given by

$$\boldsymbol{\varepsilon}_e^{th}(x_e) = \alpha(x_e) \Delta T_e \boldsymbol{\phi}^T. \quad (50)$$

Here,  $\alpha(x_e)$  is the thermal expansion coefficient that is also dependent on element density,  $\Delta T_e$  is the temperature change of element  $e$  (taken here as the average of nodal temperatures), and  $\boldsymbol{\phi}$  is simply the vector  $[110]$  or  $[111000]$  for two and three dimensional problems, respectively. Substitution of Equations (48) and (50) into (49) yields

$$\mathbf{f}_e^{th}(x_e) = E(x_e) \alpha(x_e) \int_{\Omega_e} \mathbf{B}_e^T \bar{\mathbf{C}}_e \Delta T_e \boldsymbol{\phi}^T d\Omega \quad (51)$$

in which we note that both  $E(x_e)$  and  $\alpha(x_e)$  are dependent on density design variables and thus both necessitate material interpolation. To simplify, we combine these parameters into a single thermal stress coefficient as

$$\beta(x_e) = E(x_e) \alpha(x_e). \quad (52)$$

The TSC is then treated as an inherent material property and  $\mathbf{f}_e^{th}(x_e)$  can be rewritten as

$$\mathbf{f}_e^{th}(x_e) = \beta(x_e) \int_{\Omega_e} \mathbf{B}_e^T \bar{\mathbf{C}} \Delta T_e \boldsymbol{\phi}^T d\Omega. \quad (53)$$

Finally, the global thermal load vector is assembled by summing element contributions

$$\mathbf{F}^{th}(\mathbf{x}) = \sum_{e=1}^N \mathbf{f}_e^{th}(x_e). \quad (54)$$

Again, the element thermal load vector for nondesign elements can be obtained from the previous relations by taking  $x_e = 1$ .

### 4.3 Topology Optimization Formulations

#### 4.3.1 Minimum Compliance with Thermal Loading

The first formulation investigated is the basic minimum compliance (maximum stiffness) objective with a volume fraction constraint. As discussed in the literature review in Section 3.3.2, the validity of the compliance objective for topology optimization with thermal loads has been questioned. It is nonetheless investigated here to gain further insights into why it fails to yield useful results for the problems of interest. The mathematical statement of the topology

problem for minimum compliance is given as:

$$\begin{aligned}
\min : \quad & c(\mathbf{x}) = \mathbf{F}^T \mathbf{U} = \mathbf{U}^T \mathbf{K}(\mathbf{x}) \mathbf{U} \\
\text{subject to :} \quad & g(\mathbf{x}) = \sum_{e=1}^{N_d} (\rho_e v_e - V_f v_e) \leq 0 \\
& \mathbf{K}(\mathbf{x}) \mathbf{U} = \mathbf{F}^{th}(\mathbf{x}) \\
& 0 < x_{min} \leq x_e \leq 1
\end{aligned} \tag{55}$$

where  $c$  is the compliance,  $\rho_e$  is the physical density of element  $e$  (related to the design variable density  $x_e$  through a filter),  $v_e$  is the volume of element  $e$ ,  $V_f$  is the allowable volume fraction, and  $x_{min}$  is the minimum allowable value of design variables. The sensitivity of the compliance objective to the physical density  $\rho_j$  is derived from the definition of compliance  $c = \mathbf{F}^T \mathbf{U}$  and the adjoint method as

$$\frac{dc}{d\rho_j} = \frac{d}{d\rho_j} (\mathbf{F}^T \mathbf{U}) = \frac{d\mathbf{F}^T}{d\rho_j} \mathbf{U} + \mathbf{F}^T \frac{d\mathbf{U}}{d\rho_j}. \tag{56}$$

The derivative of the displacement vector  $\frac{d\mathbf{U}}{d\rho_j}$  is obtained by taking the derivative of Equation (44) with respect to  $\rho_j$  (note that only the thermal load vector is dependent upon density variables)

$$\begin{aligned}
\frac{d}{d\rho_j} (\mathbf{K} \mathbf{U}) &= \frac{d}{d\rho_j} (\mathbf{F}) \\
\frac{d\mathbf{K}}{d\rho_j} \mathbf{U} + \mathbf{K} \frac{d\mathbf{U}}{d\rho_j} &= \frac{d\mathbf{F}^{th}}{d\rho_j} \\
\frac{d\mathbf{U}}{d\rho_j} &= \mathbf{K}^{-1} \left( \frac{d\mathbf{F}^{th}}{d\rho_j} - \frac{d\mathbf{K}}{d\rho_j} \mathbf{U} \right).
\end{aligned} \tag{57}$$

Substituting (58) into (56) yields,

$$\frac{dc}{d\rho_j} = \frac{d\mathbf{F}^T}{d\rho_j} \mathbf{U} + \mathbf{F}^T \mathbf{K}^{-1} \left( \frac{d\mathbf{F}^{th}}{d\rho_j} - \frac{d\mathbf{K}}{d\rho_j} \mathbf{U} \right) \tag{58}$$

where we note the compliance problem is self-adjoint such that  $\mathbf{F}^T \mathbf{K}^{-1} = \mathbf{U}^T$ . Equation (58) then simplifies to

$$\frac{dc}{d\rho_j} = \mathbf{U}^T \left( 2 \frac{d\mathbf{F}^{th}}{d\rho_j} - \frac{d\mathbf{K}}{d\rho_j} \mathbf{U} \right). \tag{59}$$

The sensitivity of the volume constraint is given by

$$\frac{dg}{d\rho_j} = \frac{d}{d\rho_j} \left( \sum_{e=1}^N (\rho_e v_e - V_f v_e) \right) = \frac{d}{d\rho_j} \left( \sum_{e=1}^N \rho_e v_e \right). \tag{60}$$

Finally, we note that the sensitivity equations in (59) and (60) are given with respect to physical densities  $\rho_j$ . In the optimization, the sensitivity with respect to design variable densities  $x_j$  are required, which take into account the effects of filtering and projection. Thus, the appropriate chain rule modifications from Section 3.2.2 for the density filter (Equation (15)) and Heaviside projection (Equations (17) and (18)) are used to obtain the sensitivity of the previous design responses to the density design variables.

Figure 47 shows the design domain with thermal loading for the beam strip demonstration case. Here we note loading consists of only a prescribed temperature distribution that may be spatially varying in the general case.

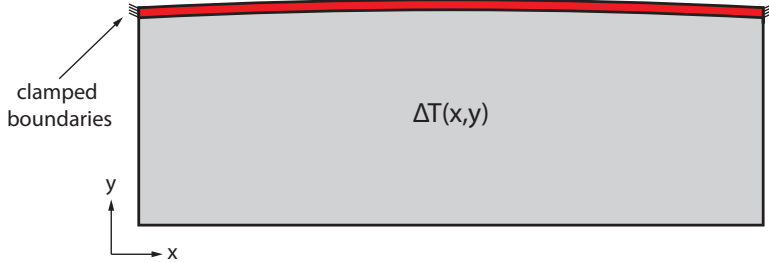


Figure 47: Beam strip stiffening topology optimization domain with loading and boundary conditions for the minimum compliance with thermal loading formulation.

#### 4.3.2 Artificial Mechanical Load Method

The second topology optimization formulation takes a different approach to stiffness design for restrained expansion. It was first demonstrated by Haney [16] and attempts to derive a structure using only mechanical loading that behaves favorably in a thermal environment. The mathematical statement here takes the form of a basic minimum compliance case with mechanical loading:

$$\begin{aligned}
 \min : \quad & c(\mathbf{x}) = \mathbf{F}^T \mathbf{U} = \mathbf{U}^T \mathbf{K}(\mathbf{x}) \mathbf{U} \\
 \text{subject to :} \quad & g(\mathbf{x}) = \sum_{e=1}^N (\rho_e v_e - V_f v_e) \leq 0 \\
 & \mathbf{K}(\mathbf{x}) \mathbf{U} = \mathbf{F}^a \\
 & 0 < x_{min} \leq x_e \leq 1
 \end{aligned} \tag{61}$$

We note that there is no thermal load and  $\mathbf{F}^a$  is an externally applied artificial mechanical load. To determine the application of this load, we recognize the fact that the optimum structure resulting from a problem of the form in (61) has a material distribution to best resist the applied load  $\mathbf{F}^a$ . Simply put, a structure is developed that is resistant to deformation in the direction of the applied load, but has very little stiffness in any other direction. Recalling the original design goal of this chapter, which was to reduce out-of-plane deformation of a thin component with restrained expansion, it follows that this may be accomplished by applying an artificial mechanical load (in the absence of any

thermal loading) in the direction we wish to reduce displacement. Logically, it also follows that since the mechanically derived structure has little stiffness in off-load directions, it is rendered incapable of generating large reaction forces because the added stiffening material is not aligned in a path to do so. This is in perfect contrast to the case of a pure thickness increase, where added material contributes directly to reaction loads.

While intuitively suitable designs may be generated if the artificial loads are applied in the proper direction, in practice the thermoelastic performance of the resulting designs is sensitive to how the artificial loads are applied to the design model. This limitation was not discussed in prior work regarding this technique [16]. In the beam strip stiffening demonstration example, one may choose to apply artificial loading as a uniform distributed load or fewer discrete loads as shown in Figure 48. While it will be demonstrated that different artificial load configurations yield varying thermoelastic performance this method is still attractive because of its simplicity. In fact, since thermal loading is not taken directly in the topology optimization, commercial software could be utilized for this formulation.

Finally, the sensitivity computations in this problem are identical to those in Equations (56) to (60) when the load vector terms are neglected (externally applied loading is independent of topological variation).

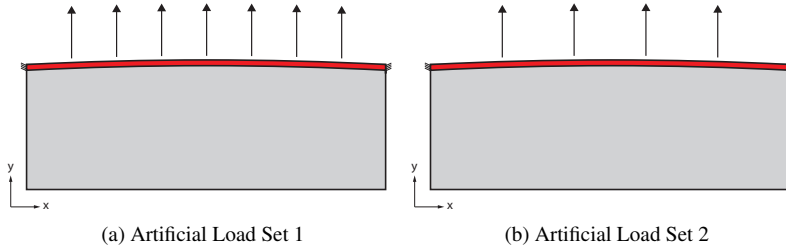


Figure 48: Beam strip stiffening topology optimization domain with two different load sets for the artificial mechanical load formulation.

#### 4.3.3 Thermoelastic Combination Method

The final technique to solve the stiffening problem is a proposed extension of the previous artificial mechanical load method. While the previous problem setup exploits the fundamental mechanics of minimum compliance topology optimization, it does not directly address the boundary reaction increases that usually result from adding material in a thermal environment. In addition, the resulting designs are dependent upon the application of artificial load cases. In an effort to both remove this dependency and to control the boundary reaction loading, additional constraints are added to the optimization problem. These constraint limit the reaction loading at the boundaries of the structure that are generated by the restrained thermal expansion expansion.

In formulating the optimization problem, the minimum compliance objective function is retained, where the compliance is determined from an artificial load case. In addition, a separate thermoelastic analysis is performed where loading consists of the original temperature field. The reaction loads from this analysis are utilized to directly enforce

the new constraints in the topology optimization problem. Thus, the mathematical statement of this problem is:

$$\begin{aligned}
\min : \quad & c(\mathbf{x}) = \mathbf{U}_1^T \mathbf{K}(\mathbf{x}) \mathbf{U}_1 \\
\text{subject to :} \quad & g_v(\mathbf{x}) = \sum_{e=1}^N (\rho_e v_e - V_f v_e) \leq 0 \\
& g_{r,k}(\mathbf{x}) = S_k - R_o \leq 0 \\
& \mathbf{K}(\mathbf{x}) \mathbf{U}_1 = \mathbf{F}^a \\
& \mathbf{K}(\mathbf{x}) \mathbf{U}_2 = \mathbf{F}^{th}(\mathbf{x}) \\
& 0 < x_{min} \leq x_e \leq 1
\end{aligned} \tag{62}$$

In (62), we note the presence of two finite element analyses with  $\mathbf{U}_1$  being the displacement vector for the system with artificial load set  $\mathbf{F}^a$  and  $\mathbf{U}_2$  being the displacement vector for the system with thermal load  $\mathbf{F}^{th}(\mathbf{x})$ . The compliance  $c$  is computed using  $\mathbf{U}_1$  and is only dependent upon the artificial load.  $S_k$  is the reaction load for the  $k$ th set of degrees of freedom (DOF) for the thermal load system and  $R_o$  is the allowable reaction.  $S_k$  may be determined from the vector of reaction loads obtained following the solution of the second finite element problem using:

$$\mathbf{R} = \mathbf{K}(\mathbf{x}) \mathbf{U}_2 - \mathbf{F}^{th}(\mathbf{x}) \tag{63}$$

$$S_k = \sum_{i \in D_k} R_i \tag{64}$$

Here  $\mathbf{R}$  is a vector that contains reaction forces at degrees of freedom on which boundary conditions are applied and zeros elsewhere.  $\mathbf{F}^{th}(\mathbf{x})$  in this case is the load vector before boundary condition application in the finite element solution process. The total reaction load  $S_k$  is determined as the summation of individual reactions  $R_i$  on degrees of freedom  $i$  in the set  $D_k$ . The subscript  $k$  indicates that multiple sets can be defined to enforce reaction constraints at various attachment points in a model. Alternatively, if a reaction is to be enforced on a single DOF, the same relations apply assuming that the set  $D_k$  consists of only a single value  $i$  equal to the DOF of interest. The sensitivity of the reaction  $S_k$  to physical density  $j$  is obtained from

$$\frac{dS_k}{d\rho_j} = \sum_{i \in D} \frac{dR_i}{d\rho_j} \tag{65}$$

where the sensitivity of the resultant load at a particular degree of freedom is developed as follows. We begin by differentiating

$$\frac{d\mathbf{R}}{d\rho_j} = \frac{d\mathbf{K}}{d\rho_j} \mathbf{U}_2 + \mathbf{K} \frac{d\mathbf{U}_2}{d\rho_j} - \frac{d\mathbf{F}^{th}}{d\rho_j} \tag{66}$$

and obtain the derivative of the displacement vector  $\mathbf{U}_2$  from the equilibrium equation as in Equation (57). Substitution

into the preceding relationship yields

$$\frac{d\mathbf{R}}{d\rho_j} = \frac{d\mathbf{K}}{d\rho_j} \mathbf{U}_2 + \mathbf{K} \mathbf{K}^{-1} \left( \frac{d\mathbf{F}^{th}}{d\rho_j} - \frac{d\mathbf{K}}{d\rho_j} \mathbf{U}_2 \right) - \frac{d\mathbf{F}^{th}}{d\rho_j} \quad (67)$$

which yields the sensitivity for the *entire* reaction load vector. Unfortunately, for even moderately sized systems the computation of the adjoint vectors by solving  $\mathbf{K} \mathbf{K}^{-1}$  is computationally prohibitive. In practice, it has been found that computing the sensitivity for individual induces  $i$  in the reaction vector, given as  $dR_i/d\rho_j$ , is efficient. This process is given by

$$\frac{dR_i}{d\rho_j} = \frac{d\mathbf{K}_i}{d\rho_j} \mathbf{U}_2 + \lambda_i^T \left( \frac{d\mathbf{F}^{th}}{d\rho_j} - \frac{d\mathbf{K}}{d\rho_j} \mathbf{U}_2 \right) - \frac{dF_i^{th}}{d\rho_j} \quad (68)$$

where the adjoint vector  $\lambda_i$  is found from the solution of the adjoint system

$$\mathbf{K} \lambda_i = \mathbf{K}_i. \quad (69)$$

In the previous relations,  $\mathbf{K}_i$  is the column of the global stiffness matrix and  $F_i^{th}$  is the global thermal load entry that corresponds to degree of freedom  $i$ .

To summarize, Figure 49 shows the topology optimization domain for the beam strip stiffening problem with both the artificial load system and the thermoelastic system. Here the arrangement of artificial load is arbitrary and multiple configurations will be tested in the results section.

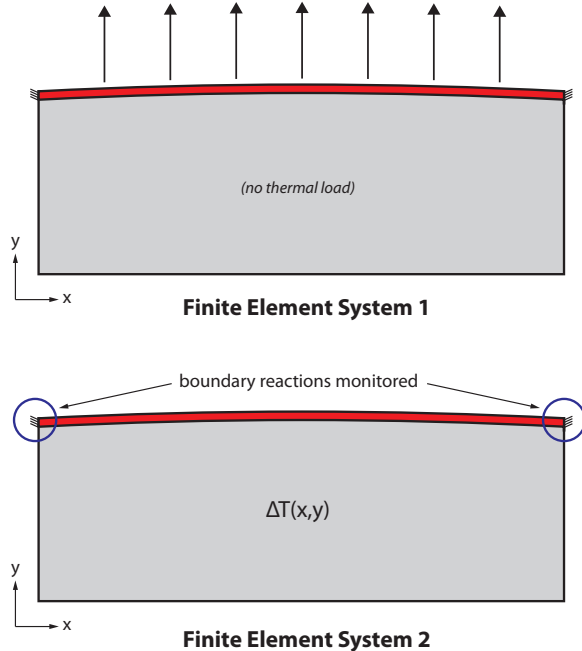


Figure 49: Beam strip stiffening topology optimization domain with two separate finite element analysis required to obtain design responses.

## 4.4 Computational Implementation

It is known that in the presence of design dependent loading, which includes thermal loads, the SIMP interpolation scheme presents numerical difficulties as discussed in Section 3.3.2. As a result, the RAMP model is adopted. Thus, the stiffness and TSC are interpolated according to

$$E(\rho_e) = \frac{\rho_e}{1 + R_E(1 - \rho_e)} E_o \quad (70)$$

$$\beta(\rho_e) = \frac{\rho_e}{1 + R_\beta(1 - \rho_e)} E_o \alpha_o \quad (71)$$

where  $R_E$  and  $R_\beta$  are RAMP parameters. In addition,  $E_o$  and  $\alpha_o$  are baseline material properties for the elastic modulus and coefficient of thermal expansion, respectively. Also, recall here that  $\rho_e = f(x_e)$  through the applied filters.

To prevent checkerboarding and enforce length scale, the density filter is utilized. In addition, to eliminate transition areas of gray material along structural boundaries that accompany the density filter, the Heaviside filter is applied. The criteria of black/white design is desirable because while intermediate density material may result in superior thermoelastic performance (as evidenced by the usage of bi-material structures in other works [94, 76]) in practical application it is difficult to physically realize these structural characteristics when using high temperature aerospace metals or even composites. In the following examples, a continuation scheme is used to increase the Heaviside projection parameter  $\gamma$  from zero up to a maximum of 32 at a specified interval of iterations that is generally application specific and dependent upon the number of designable elements. In some cases the parameter is also doubled if the change in design variables between iterations is less than 0.001.

Finally, since commercial topology optimization software is unable to directly address thermal loads, a custom implementation of the formulations have been developed in MATLAB. This includes the topology optimization algorithms, finite element analysis, and analytical sensitivity analysis using the adjoint method.

## 4.5 Example 1: Stiffened Beam Strip

### 4.5.1 Design Problem Setup

The discretized finite element model for the beam strip demonstration problem corresponding to the design domain shown in Figure 45 is given in Figure 50. Both the non-design and designable regions are meshed using four-node bilinear quadrilateral elements (in plane stress). A total of 7800 elements are utilized (total 7500 designable). The elements are assumed to have unit depth in the plane. Their dimensions are approximately 0.08 x 0.08 inches, but due to the curvature of the top of the design domain they are not perfectly square/rectangular. Finally, boundary conditions consist of clamped conditions applied at the edge of the non-design domain represented by fixed nodal translations.

Any boundary that forms inside the the designable region as the topology evolves is assumed to remain traction free. Finally, a filter radius of 0.16 inches is used.

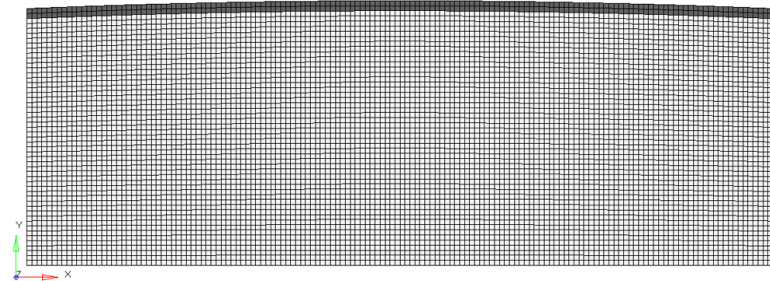


Figure 50: Finite element mesh for the beam strip stiffening example problem with non-design elements (dark gray) and designable elements (white).

#### 4.5.2 Topology Optimization Results

**Minimum Compliance with Thermal Load** The result for the minimum compliance topology optimization problem with purely thermal loading outlined in Equation (55) is shown in Figure 51a, where the dotted line indicates the boundary of the designable region. In this case, the RAMP parameters are  $R_E = 8$  and  $R_\beta = 0$  and the allowable volume fraction is taken as 0.20. We observe that the optimum structure contains only trace amounts of added material near the application of the boundary conditions. This occurs due to the participation of thermal loading directly in the compliance objective. In this scenario, where thermal loads heavily dominate mechanical effects, any material addition with the exception of in localized regions that may reduce deformation in the non-design domain actually increases the compliance of the entire structure. This becomes obvious in the iteration history of the compliance and volume shown in Figure 51b. It is readily apparent that to achieve a minimum compliance design, as little material as possible should be utilized. This parallels the conclusions of the demonstration case where it was observed material addition isn't always beneficial in a thermal environment.

To further demonstrate, the sensitivity of the compliance objective to element density design variables is shown in Figure 52. Sensitivities for a design variable field with all elements equal to 0.001, 0.10, and 0.20 are provided. We see in each the majority of elements, with the exception of small localized regions which were retained in the optimum structure in Figure 52, have positive gradients. This indicates that the existence of the elements, and the accompanying increased thermal load, serves to only increase compliance.

From these results it becomes evident that in cases with significant thermal loads and an absence of mechanical effects, the minimum compliance topology optimization formulation is unable to produce suitable designs. In fact, the majority of thermoelastic topology optimization literature only investigates cases where the amount of thermal loading is benign compared with mechanical loading and thus these effects go largely unnoticed. With the fictitious

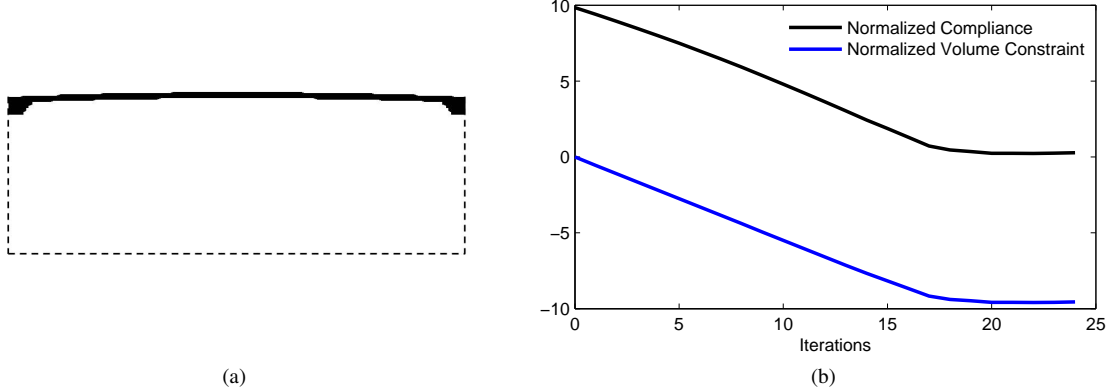


Figure 51: (a) Resulting topology and (b) iteration history for the minimum compliance with thermal load problem formulation.

mechanical load and thermoelastic combination results that follow, we demonstrate that alternative approaches to the thermoelastic problem can lead to usable results.

**Artificial Mechanical Load** Figure 53 shows the optimum topology designs obtained via the artificial mechanical load method of Equation (61) for the two load sets in Figure 48. Two volume fractions, 0.20 and 0.30, are given. The RAMP parameter for all cases of this method is taken as  $R_E = 8$ .

In contrast to the previous method, it is obvious that potentially useful stiffening structures are obtained. This is expected because a well posed minimum compliance with purely mechanical loading problem was utilized. We note that in each case, optimum structures span the entire depth of the designable region and contain a lower inverted arch structure. This inverted arch is connected to the upper non-design region at locations where the fictitious mechanical loads are applied. We also note that increasing the allowable volume fraction results in an identical design with thicker members. These results are characteristic of the particular type of topology optimization problem that was solved. The iteration history for the compliance objective and volume fraction constraint is given in Figure 54 (results shown for volume fraction of 0.20 only). Note the sharp jumps in responses correspond to iterations when the  $\beta$  parameter in the Heaviside filter was increased.

To investigate the thermoelastic performance of each structure, a separate analysis was performed wherein the fictitious loads were removed, and the structures were subjected to a uniform elevated temperature of  $\Delta T = 900^{\circ}\text{F}$ . The reaction ratio  $R/R_o$ , which here is taken as the reaction load for a particular design divided by that of the unstiffened non-design domain (i.e., the original strip), was obtained to assess the designs from a reaction increase perspective.  $R/R_o$  for the designs in Figure 53 are (a) 2.18, (b) 2.32, (c) 1.73, and (d) 1.81. From these results, we observe that in these cases, allowing more material utilization will increase the reactions. It is also apparent that some load configurations of fictitious loading may lead to superior designs from a thermoelastic point-of-view. The results

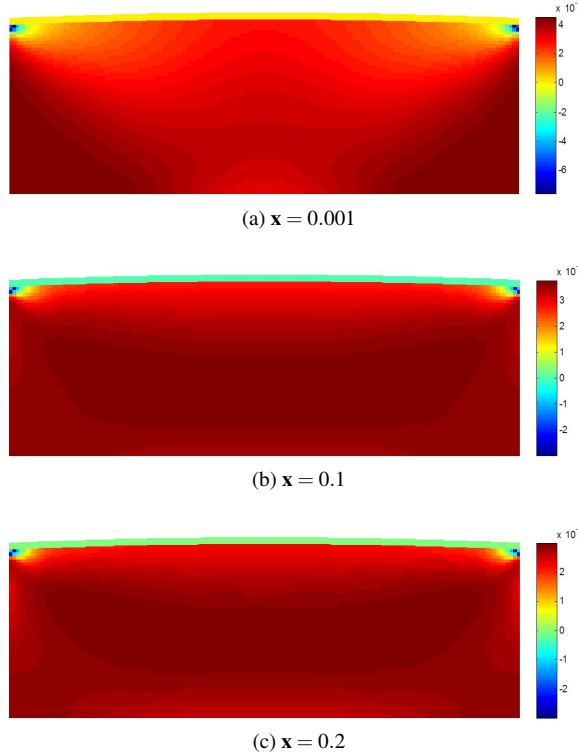


Figure 52: Compliance sensitivity for each element at (a)  $x = 0.001$ , (b)  $x = 0.1$ , and (c)  $x = 0.2$ .

obtained from the thermoelastic combination method presented in the next method further investigate this conclusion.

**Thermoelastic Combination** Figure 55 gives the results for the thermoelastic combination method problem formulation from Equation (62) for reaction constraints corresponding to reaction ratios of  $R/R_o$  of 1.25, 1.50, and 1.75. The topological designs using both of the fictitious load cases from the previous section are presented. The allowable volume fraction is taken as 0.2 and the RAMP parameters are  $R_E = 16$  and  $R_B = 2$ .

It is observed that for low allowable reaction loading ( $R/R_o = 1.25$ ) in Figure 55a and 55b that nearly identical designs are obtained for both fictitious load cases. This indicates that by including direct consideration of reaction loading in the design problem, the sensitivity of the results to the application of the fictitious load cases can be removed. It also appears that a structure has been generated in which the in-plane expansion of the upper non-design domain and the lower arch-like structure, which is now more rounded when compared to previous designs in Figure 53, is counteracted by the mechanics of the internal connecting members. This apparent tailoring of thermal expansion allows for the satisfaction of tighter limits on reaction load.

If the reaction constraint is relaxed such that  $R/R_o$  is 1.50, we observe from Figure 55b and 55c that the resulting structures still resemble fundamentally the same configuration. The designs now contain less complex internal connecting members that in fact, begin to resemble those in Figure 53c. Continuing to relax the reaction constraint to

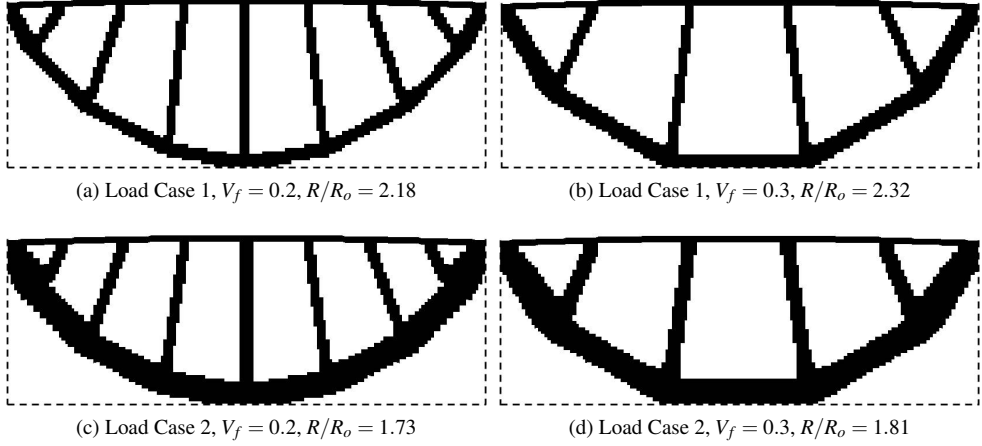


Figure 53: Topology optimization results for volume fractions of 0.20 (left column) and 0.30 (right column) for fictitious load case 1 (a,b) and case 2 (c,d).

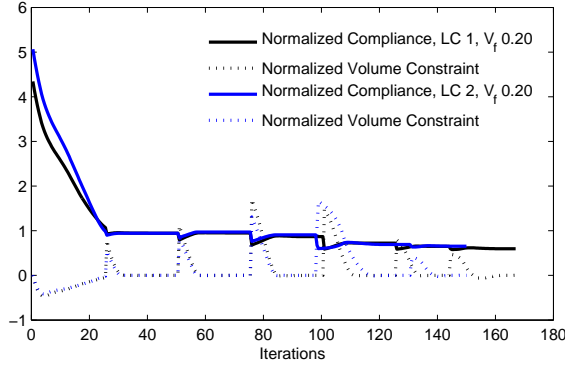


Figure 54: Iteration histories for the artificial mechanical load method with load cases 1 and 2 and volume fraction of 0.20.

allow  $R/R_o$  of 1.75 in Figure 55e and 55f leads to structures that differ for each fictitious load case and begin to resemble those in the previous section. This is to be expected as the allowable reactions are now close to the values observed previously and the significance of reactions to the design problem has been reduced. The primary differences in these results when compared to those in Figure 53 is that the internal connecting members appear to be angled slightly more towards the horizontal and the structures do not span the entire depth of the designable region. This demonstrates that as one seeks to obtain stiffening structures that lead to more benign reaction loading, additional information must be directly included in the design problem because it is difficult, if not impossible, to identify which load case will lead to suitable results a priori.

The iteration history of the compliance, volume constraint, and reaction constraint for each case is given in Figure 56. Again, large jumps in the plots that occur roughly every 50 iterations are a result of continuation in the Heaviside filter. It is notable from this figure that by introducing thermal loading into the problem by way of the reaction constraint, rather than directly in the compliance objective (as was done with the minimum compliance with thermal

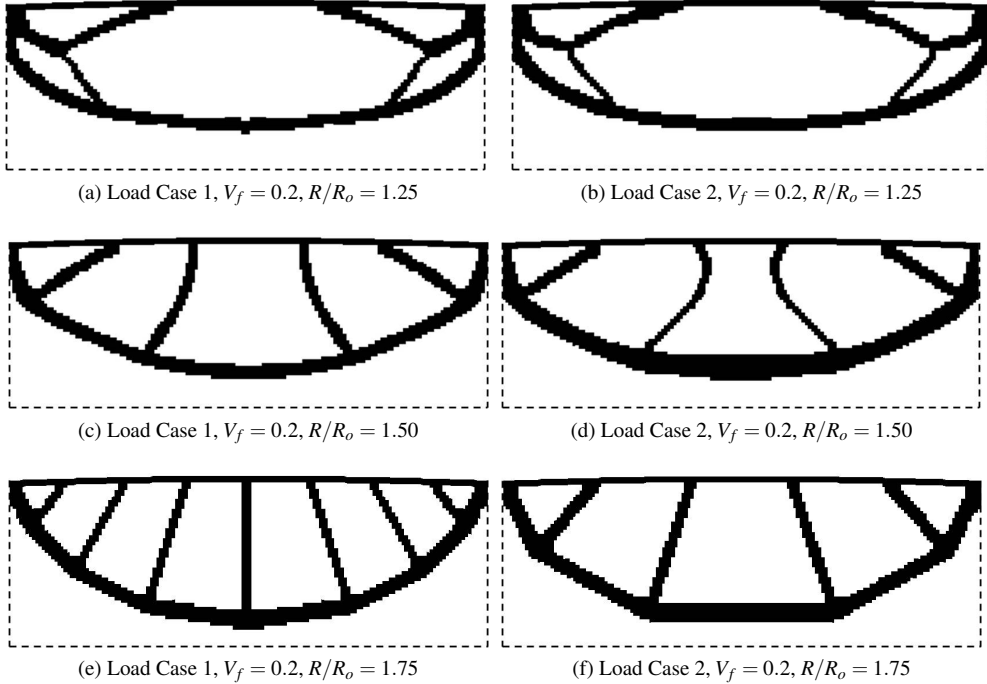


Figure 55: Topology optimization results for the thermoelastic combination problem with constraints on reaction load corresponding to  $R/R_o$  of (a,b) 1.25, (c,d) 1.50, and (e,f) 1.75.

load problem) the volume constraint remains active in the final design, which helps lead to a solid/void design. It should also be commented that convergence is much less smooth in these cases when compared to that observed in Figures 53b and 54 for the prior two problem formulations. By closely inspecting the numerical behavior of the reaction load constraint, it was observed that it is a highly sensitive quantity in elements with near zero density. In addition, the sensitivity for some elements is not unconditionally positive (increasing density increases the reaction loading) as one might expect. Thus, as the optimization process begins to approach a topology with large regions of void material (nearly zero density), small oscillations appear in convergence. However, as observed in the iteration history, these oscillations do not cause instabilities that impede convergence.

#### 4.5.3 Qualitative Assessment

In this section the thermoelastic qualities of the structures produced by the fictitious mechanical load and thermoelastic combination methods are studied. Designs are compared in terms of the reaction ratio  $R/R_o$  and the displacement ratio  $U/U_o$ . Similar to the reaction ratio, the displacement ratio is defined as the out-of-plane displacement measured at the top center node of the non-design domain for a particular stiffened design to that of the non-design domain with no stiffening material. These metrics are given in Table 4. and also provide insight into the unique mechanics by which they accomplish a reduction in deformation while limiting reaction load.

We note from the table that in all cases, the displacement ratio is reduced. This indicates that the minimum com-

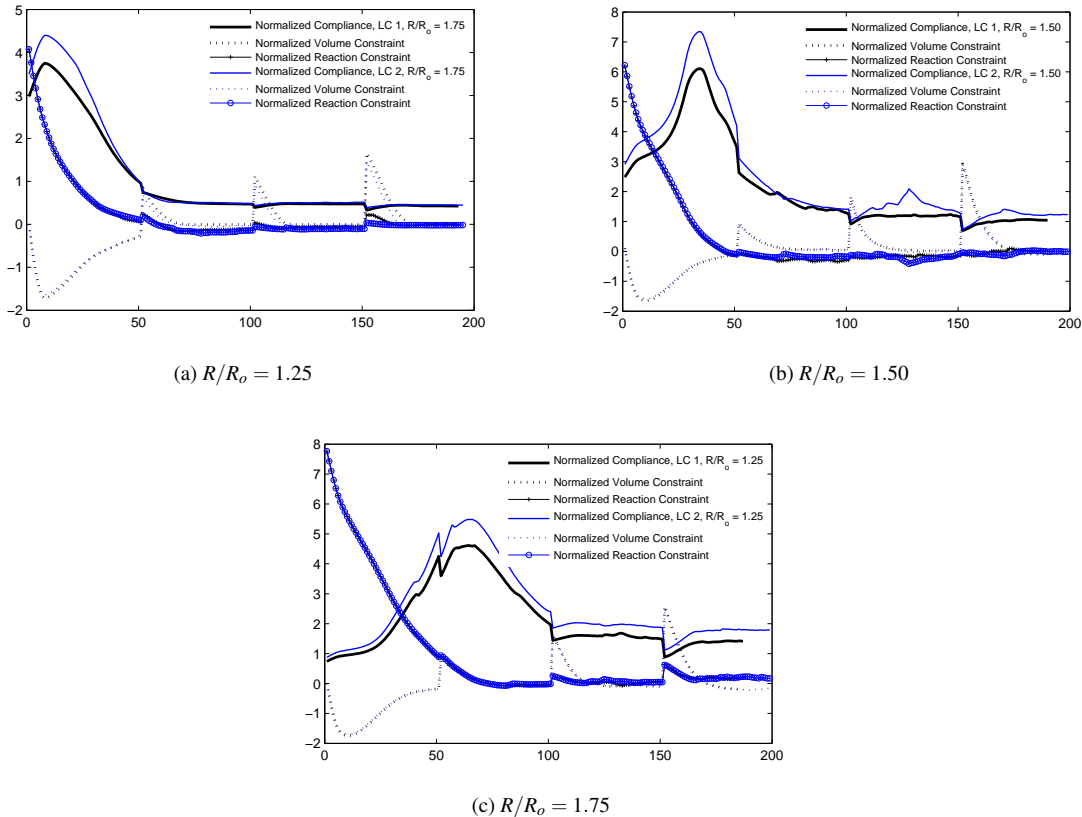


Figure 56: Iteration history for compliance, volume constraint, and reaction constraint corresponding to the topology thermoelastic combination topology optimization problems

pliance problem using the fictitious mechanical load cases does result in structures that are resistant to deformation out-of-plane and satisfy the basic design goals for displacement reduction. This holds true even when the structure is subjected to the elevated temperature environment after having been derived using mechanical loads. As evidenced by negative displacement ratios, for all of the designs, excluding those with the tightest reaction constraints, deformation at the middle of the non-design domain actually occurs downwards. This indicates the mechanics that produce reduction in displacement, when compared to the undeformed case, result in a pull-down effect due to the expansion of the stiffening structure. For the designs produced by the thermoelastic combination method and reaction ratio limited to 1.25, we note the non-design domain still deforms in the positive direction, but only do so with roughly half the magnitude of the unstiffened structure. In practical application, this halving of displacement may result in removing nearly all tensile stresses as observed in the demonstration case in Section 4.1.1. As an added benefit, this stress reduction could come at only a 25% increase in reaction loading. This effect is achieved only by harnessing the potential thermoelastic tailoring capabilities of topology optimization when the proper responses are included in the problem formulation.

<b>Topology Problem</b>	<b>Figure</b>	<b>Reaction Ratio (<math>R/R_o</math>)</b>	<b>Displacement Ratio (<math>U/U_o</math>)</b>
Artificial load (Case 1), $V_f = 0.20$	Figure 53a	2.18	-0.0470
Artificial load (Case 1), $V_f = 0.30$	Figure 53b	2.32	-0.0646
Artificial load (Case 2), $V_f = 0.20$	Figure 53c	1.73	-0.0567
Artificial load (Case 2), $V_f = 0.30$	Figure 53d	1.81	-0.0540
Thermoelastic Combo (Case 1), $R/R_o = 1.25$	Figure 55a	1.25	0.5303
Thermoelastic Combo (Case 2), $R/R_o = 1.25$	Figure 55b	1.25	0.5593
Thermoelastic Combo (Case 1), $R/R_o = 1.50$	Figure 55c	1.50	-0.0364
Thermoelastic Combo (Case 2), $R/R_o = 1.50$	Figure 55d	1.50	-0.0425
Thermoelastic Combo (Case 1), $R/R_o = 1.75$	Figure 55e	1.75	-0.0547
Thermoelastic Combo (Case 2), $R/R_o = 1.75$	Figure 55f	1.75	-0.0630

Table 4: Reaction and displacement comparison for all structural topologies for strip stiffening example.

## 5 Stress-based Topology Optimization with Thermal Loads

While the alternative topology optimization formulations developed in the previous chapter are capable of generating structures with desirable thermoelastic performance, a direct treatment of thermal stresses, which represent a primary design consideration for exhaust-washed structures, was not included. In this chapter, the application of stress-based design criteria in the topology optimization of thermal structures is studied. Based on the current state-of-the-art, appropriately considering stresses in topology optimization is challenging in itself. In addition, the application of stress criteria to thermal structures has yet to be demonstrated in the literature. Further motivation for the consideration of stresses is first discussed, then methods for addressing the fundamental challenges of thermal stress topology optimization are introduced, and finally demonstration follows.

### 5.1 A Practical Consideration

Apart from the fact that the minimum compliance formulation with thermal loading poses a challenging numerical optimization problem, there exist far more practical reasoning that minimum compliance is not a suitable objective for thermal structures design. To demonstrate on a simple problem, two identical axial rods subjected to a uniform elevated temperature  $\Delta T$  are shown in Figure 57.

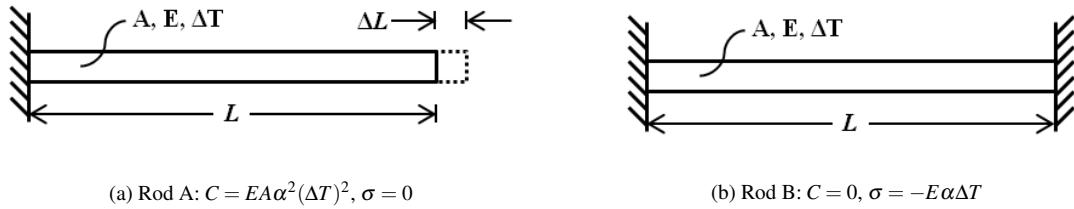


Figure 57: Axial rods with (a) fixed-free and (b) fixed-fixed end conditions subjected to a uniform elevated temperature  $\Delta T$  along with the compliance and thermal stress of each.

Rod A is freely allowed to expand while rod B is rigidly fixed on both ends. We observe that in the case of a free end, the stress equals zero because there is no thermal expansion, but compliance takes a positive value. Rod B Comparing this undergoes no deformation and thus has zero compliance, but is subjected to thermal stresses due to the restrained expansion. From strictly a thermal stress point of view, the behavior of rod A is more desirable than that of rod B; however, a minimum compliance optimization would attempt to reduce the deformation to reduce compliance, which is diametrically opposed to the basic design prescription for design against thermal stress, which we recall is to simply accommodate thermal expansion [3]. In this simple case, only compressive thermal stresses develop; however, in problems that allow for bending effects, the restrained expansion can lead to tensile stresses as observed previously. This behavior provides the basic motivation for us to seek a topology optimization formulation

that is more effective in a thermal environment from both numerical optimization and practical engineering design perspectives. In contrast the alternative formulations of the previous chapter, a direct treatment of thermal stresses in the structure is sought.

## 5.2 Finite Element Analysis for Stress

The fundamental finite element analysis and parameterization for topology optimization for the thermal stress problem follows that in Section 4.2. Once assembled using the parameterization based on density variables at the element level, the finite element problem in Equation (44) is solved to determine the global displacement vector. Using local element displacements, for a general continuum element  $e$ , the stress vector  $\sigma_e$  can be computed as

$$\sigma_e = \bar{\mathbf{C}}_e \mathbf{B}_e \mathbf{U}_e - \bar{\mathbf{C}}_e \bar{\alpha}_e \Delta T. \quad (72)$$

where both  $\bar{\mathbf{C}}_e$  and  $\bar{\alpha}_e$  are taken as the element elasticity matrix and vector containing thermal expansion coefficients for a solid element. For a two-dimensional continuum element, the stress vector contains two normal stress components,  $\sigma_{x,e}$  and  $\sigma_{y,e}$ , in addition to a shear stress  $\tau_{xy,e}$  as

$$\sigma_e = \begin{bmatrix} \sigma_{x,e} & \sigma_{y,e} & \tau_{xy,e} \end{bmatrix}^T. \quad (73)$$

The principle stresses and maximum shear stress in element  $e$  can then be computed as

$$\sigma_{1,e} = \frac{\sigma_{x,e} + \sigma_{y,e}}{2} + \sqrt{\left(\frac{\sigma_{x,e} - \sigma_{y,e}}{2}\right)^2 + \tau_{xy,e}^2}, \quad (74)$$

$$\sigma_{2,e} = \frac{\sigma_{x,e} + \sigma_{y,e}}{2} - \sqrt{\left(\frac{\sigma_{x,e} - \sigma_{y,e}}{2}\right)^2 + \tau_{xy,e}^2}, \quad (75)$$

$$\tau_{max,e} = \sqrt{\left(\frac{\sigma_{x,e} - \sigma_{y,e}}{2}\right)^2 + \tau_{xy,e}^2}, \quad (76)$$

which yield the most severe (max/min) normal and shear stress conditions in element  $e$  for the prescribed stress vector. While failure in an element can be based on the principle or maximum shear stresses, in design more failure metrics are commonly utilized to generalize material failure to states of combined normal and shear stress. For example, assuming a general failure metric is taken as a function of the element tensor as  $F_e(\sigma_e)$ , material failure is predicted in element  $e$  if

$$\frac{F_e}{\bar{\sigma}} \leq 0 \quad (77)$$

where  $\bar{\sigma}$  is a stress limit, for example the yield stress of the material. One of the most common failure metrics for metallic materials is the von Mises failure criterion, which can be determined directly from the element stress vector as

$$F_e^{(\text{vm})} = \sqrt{\sigma_{x,e}^2 - \sigma_{x,e}\sigma_{y,e} + \sigma_{y,e}^2 + 3\tau_{xy,e}^2}. \quad (78)$$

Other failure metrics, for example the Tresca (maximum shear) criterion, maximum normal stress (for brittle materials), or the Drucker-Prager criteria (which allows for different tensile and compressive yield strength), can be selected based on knowledge about the nature of material failure.

The foregoing discussions also apply to a variety of different element types. For example, the stress vector for a three-dimensional continuum element contains six components (three normal stresses and three shear stresses) as

$$\sigma_e = \begin{bmatrix} \sigma_{x,e} & \sigma_{y,e} & \sigma_{z,e} & \tau_{xy,e} & \tau_{yz,e} & \tau_{xz,e} \end{bmatrix}^T. \quad (79)$$

Three principle stresses and a maximum shear are obtained and various failure metrics can be computed for each element. For non-continuum element types, such as rod and beam elements, alternative stress components and failure metrics can be utilized. Stress relations and suitable failure metrics for most structural or continuum elements are available in most finite element, strength of materials, or applied elasticity texts [26, 123] and can ultimately be treated identically in topology optimization.

### 5.3 Relaxed Stress

As previously noted in Section 3.3.5 one of primary challenges related to including stresses in topology optimization is the singularity phenomena. In this work, the relaxation method of Le et al. [107] is adopted to relax elemental stress values and remove the singularity issues.

The elemental failure metric, for example the von Mises stress from Equation (78), is multiplied onto an interpolation function for stress  $\eta_\sigma(\rho)$  as

$$F_e = \eta_\sigma(\rho)F_e^{(\text{vm})}. \quad (80)$$

By ensuring that the solid and void values of the stress interpolation function are  $\eta_\sigma(1) = 1$  and  $\eta_\sigma(0) = 0$ , the failure metric yields the proper values for solid material and zero for void material. This removes the singularity by allowing for a state of zero stress for void material. To achieve the proper material penalization, it is desirable that intermediate density material should experience a stress state that is more severe than that obtained when a linearly proportional relationship exists between stress and material usage. This is analogous to the desire for intermediate density material to have less stiffness with respect to material whose stiffness is linearly proportional to material usage, which yields the common SIMP penalization of  $p = 3$  in minimum compliance problems. Thus, we use a stress interpolation function

of  $\eta(\rho) = \rho^{1/2}$ .

The effectiveness of this relaxation technique at removing the singularity phenomenon in the topological design space is shown in Figure 58. Two arbitrary density distributions are given in Figure 58a and Figure 58d where white regions correspond to void and black regions to solid material. The structure is fixed in all directions along the vertical edges on the left and right side and a mechanical load is applied at the center of the bottom edge. A uniform elevated temperature is also applied to the entire domain. Figures 58b and 58e show the von Mises stress field as computed directly from the finite element results using Equations (72) and (78) for the two density distributions. We note that excessively high stresses are apparent for both cases in regions where there is actually no material due to the singularity in the stress function. Figures 58c and 58f show the relaxed von Mises stress measure that results after application of the stress interpolation function in Equation (80) with  $\eta(\rho) = \rho^{1/2}$ . It is readily apparent that the relaxation is effective at removing the singularities in regions where there is no material, while retaining stress information in solid regions of the structure. These insights are significant because they indicate that the method is effective for stresses of non-mechanical origin.

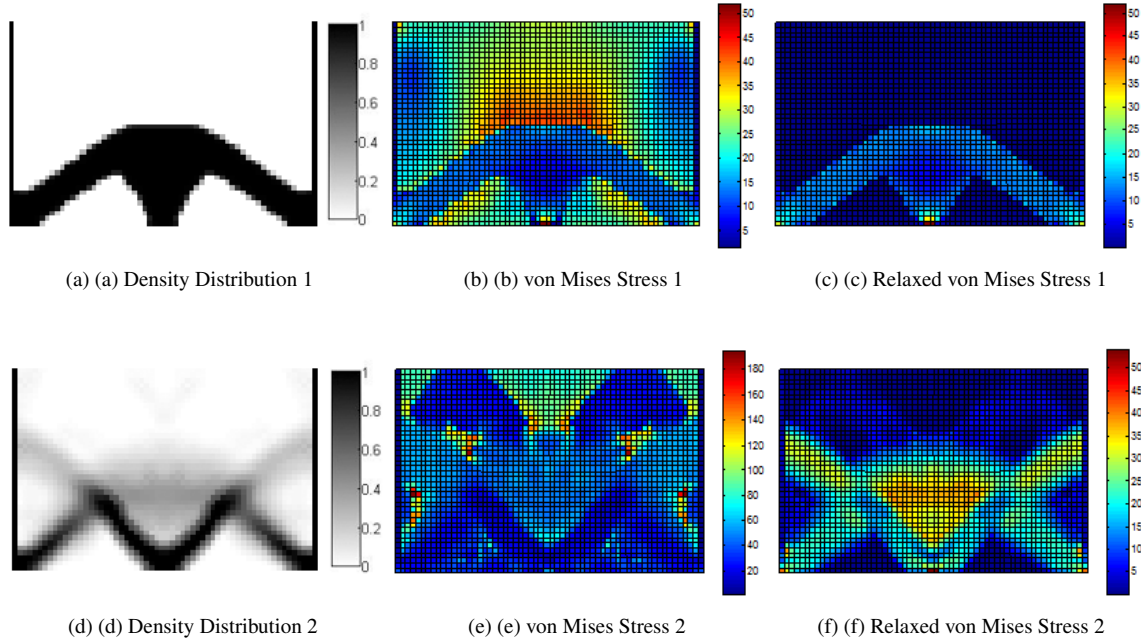


Figure 58: Two arbitrary density distributions for structures subjected to combined mechanical and thermoelastic loads given in (a,d) along with their corresponding von Mises stress distributions (b,e) and relaxed von Mises stress distributions (c,f) using the interpolation from Equation (80).

## 5.4 Adaptive Stress Aggregation

Another primary challenge in stress-based topology optimization is effectively capturing the the maximum stress within an evolving design domain at a level of computational expense that is suitable for industrial size topology optimization problems. As discussed previously, the local method, in which stresses are monitored locally in every element, proves computationally infeasible in topology optimization due to the excessive cost of sensitivity analysis (one adjoint evaluation per element). Global or aggregation methods can group the stress measure of a number of elements into a single value; however, doing so leads severely degrades the local resolution of stress. In fact, increasing the number of elements that are grouped together tends to increase the discrepancy between the aggregated prediction and the actual maximum stress within the grouped set such that limits on stress or material failure cannot be reliably enforced.

To overcome the loss of local accuracy associated with aggregation methods while retaining their efficient sensitivity computation, an adaptive aggregation technique to capture the maximum stress within the design domain is utilized in this work. At each iteration in topology optimization, the relaxed failure metric for stress  $F_e$ , from Equation (80), is first computed for each element whose stress is of interest. Without loss of generality, a *p-norm* function is utilized to aggregate the elemental failure metrics as

$$PN = \left[ \sum_{e=1}^{N_e} \left( \frac{F_e}{\bar{\sigma}} \right)^p \right]^{1/p} \quad (81)$$

where  $N_e$  is the number of elements to be aggregated together and  $p$  is a specified tuning parameter. In general, higher values of  $p$  increase the accuracy of the approximation with  $PN \rightarrow \max(F_e/\bar{\sigma})$  for  $p \rightarrow \infty$ ; however, in practice both numerical and optimization convergence issues occur if the value selected for  $p$  is too great. This ensures considerable error between  $PN$  and  $\max(F_e/\bar{\sigma})$  is present for all feasible values of  $p$ . Assuming no discrepancy between  $PN$  and  $\max(F_e/\bar{\sigma})$ , material failure is predicted if  $PN \geq 1$  and a constraint in the optimization problem can be posed as

$$g = PN - 1 \leq 0. \quad (82)$$

Consider now, the behavior of a typically gradient-based optimization process. As the objective function converges and constraints are satisfied, converging behavior is also generally observed in all system responses, including elemental stresses. If an aggregation, such as that in Equation (81), is utilized, this implies that the values that are grouped together, in this case  $F_e/\bar{\sigma}$  for all  $N_e$ , and the aggregation result  $PN$  exhibit convergent behavior. It follows then that the discrepancy between  $PN$  and  $\max(F_e/\bar{\sigma})$  approaches a constant value. Exploiting this feature, the constraint in

Equation (82) can be rewritten with an adaptive factor  $s^i$  as

$$g = s^i PN^i - 1 \leq 0. \quad (83)$$

Here  $s^i$  is taken as the ratio between the  $PN$  value and  $\max(F_e/\bar{\sigma})$  in the previous optimization iteration and given by

$$s^i = \frac{PN^{i-1}}{\max(F_e/\bar{\sigma})^{i-1}}. \quad (84)$$

We note here that by modifying constraints in the optimization problem in this way, a new problem is actually posed in each iteration. Since nearly all gradient-based optimization algorithms utilize information from previous design iterations, some amount of noise and error is introduced to the process. However, as iteration continues, these issues are alleviated as variations in the design are reduced and  $s^i$  approaches a constant value. In addition, as  $s^i$  becomes constant, the constraint in Equation (83) is acting to satisfy the prescribed limit stress  $\bar{\sigma}$  with the discrepancy introduced by aggregation effectively removed.

## 5.5 Problem Formulations

Using the methods discussed in this chapter to treat the fundamental challenges of stress criteria in topology optimization, stress-based design criteria can be addressed in two ways. That is, stress considerations may be treated as an objective of design or a constraint. Treating stress criteria as a constraint on design relates to conventional mechanical design practices, where a component is developed such that the maximum stress does not exceed an allowable value. While not a typical design objective, the idea of minimizing the maximum stress in a structure is useful in multiple ways. First, it is a useful objective for comparing the stress distribution for a given design with that of the most benign stress distribution that can be obtained in a prescribed design domain. Moreover, minimizing stress can also identify beneficial structural features that aid in the reduction of stress for problematic domains or challenging physics. Two mathematical formulations for topology optimization with stress criteria are now introduced, beginning first with stress considerations as constraints in the optimization problem.

Equation (85) gives the formulation for a topology optimization where the objective is to minimize the material usage with a constraint on the maximum stress in the designable region. The adaptive stress measure from Equation (83) is utilized to ensure the constraint accurately reflects the maximum stress limit.

$$\begin{aligned}
\min : \quad f(\mathbf{x}) &= \sum_{e=1}^{N_d} (\rho_e v_e) \\
\text{subject to :} \quad g(\mathbf{x}) &= s^i PN^i - 1 \leq 0 \\
\mathbf{K}(\mathbf{x})\mathbf{U} &= \mathbf{F}^m + \mathbf{F}^{th}(\mathbf{x}) \\
0 < x_{min} &\leq x_e \leq 1
\end{aligned} \tag{85}$$

In the formulation, a finite element analysis with both mechanical and thermal loading is utilized. In addition, any metric may be utilized to represent the material failure criterion  $F_e$  in the  $PN$  aggregation.

Equation (86) gives the formulation for a minimum stress criterion formulation.

$$\begin{aligned}
\min : \quad f(\mathbf{x}) &= PN \\
\text{subject to :} \quad g(\mathbf{x}) &= \sum_{e=1}^{N_d} (\rho_e v_e - V_f v_e) \leq 0 \\
\mathbf{K}(\mathbf{x})\mathbf{U} &= \mathbf{F}^m + \mathbf{F}^{th}(\mathbf{x}) \\
0 < x_{min} &\leq x_e \leq 1
\end{aligned} \tag{86}$$

Here, a constraint that limits the material usage is selected; however, other constraints are possible. The objective is to minimize the basic  $PN$  relation from Equation (81). Since the goal is to minimize overall stress field in the structure, the adaptive technique is not required because we need not capture the actual maximum value of elemental stress in the optimization problem. A reduction in any elemental stress included in the aggregation will be reflected by a reduction in the value of  $PN$ .

## 5.6 Demonstration

The topology optimization formulations described in the previous sections are now demonstrated on an example problem with combined thermal and mechanical loading. The test problem is inspired by the bi-clamped domain with combined loading first introduced by Rodrigues and Fernandes [67] and explored by various authors for compliance minimization in the presence of thermal loading. Figure 59 shows the design domain for the structure. It is discretized with four node bi-linear quadrilateral plane stress elements with 90 elements in the horizontal direction and 60 elements in the vertical direction. The elastic modulus of the material is  $E = 210$  GPa, the coefficient of thermal expansion is  $\alpha = 1.1 \times 10^{-5}/^\circ\text{C}$ , the Poisson's ratio is  $\nu = 0.3$ , and the thickness is taken as  $t = 0.01$  m. Gray elements in the figure denote non-design regions in the model while white elements give the designable domain. A mechanical load of

$F = 10$  kN is applied to the center of the bottom edge along with a uniform temperature increase of  $\Delta T$ . A small non-design region near the application of the mechanical point load is included to prevent a geometrical stress singularity.

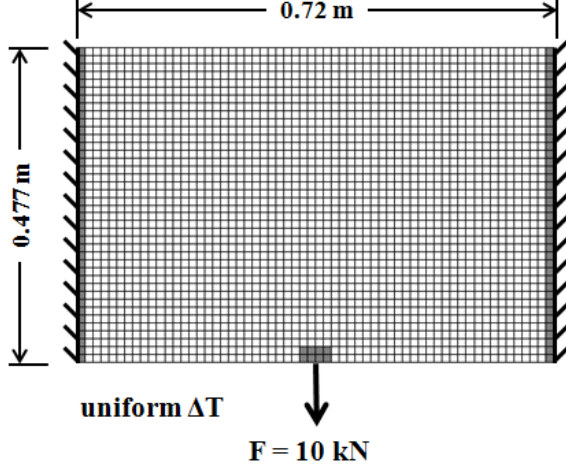


Figure 59: Bi-clamped structural domain with non-design (gray) and designable (white) regions.  $E = 210$  GPa,  $\alpha = 1.1 \times 10^{-5}/^\circ\text{C}$ ,  $v = 0.3$ ,  $t = 0.01$  m

Both the stress-constrained topology optimization problem posed in Equation (85) and the minimum stress measure problem in Equation (86) are solved with temperature load  $\Delta T = 5$ . The nonlinear optimization problems are solved using the MMA optimizer [?] and custom finite element and sensitivity analysis. The von Mises failure criterion is utilized for both problems and the limit stress for the stress-constrained problem is taken as  $\bar{\sigma} = 50$  MPa. For the minimum stress measure problem, the allowable volume is taken as 25% of the designable domain. The p-norm parameter in Equation (81) is taken as  $p = 10$ . The density filter is utilized and the filter radius is taken as 0.02. Finally, the RAMP interpolation scheme is utilized for the stiffness and thermal stress coefficient are  $q_E = 8$  and  $q_\beta = 0$ , while a SIMP model is adopted for stress interpolation as  $\eta_\sigma = \rho_e^{1/2}$ .

### 5.6.1 Results

Figure 60 shows the results of both the stress-constrained topology problem along with the minimum stress measure, material-constrained problem. The density distribution for the stress-constrained design is given in Figure 60a, the von Mises stress distribution in 60c, and the iteration history of the normalized objective and constraint is given in 60e. The same results are given in Figures 60b, 60d, and 60f for the minimum stress measure design.

Inspecting the density distributions in Figures 60a and 60b, we note that similar structural connectivity is observed in the domain. In fact, this is expected due to the simplicity of the loading and domain in this demonstration problem; however, the differences in the design indicative of the fundamental workings of each design formulation. The first primary difference we observe is the material usage in each design problem. For the stress-constrained design, only

13.7% of the domain is utilized for structural material, compared with 24.5% in the minimum stress measure problem. In addition, the stress-constrained problem satisfied the stress constraint of 50 MPa with a maximum stress of 50.5 MPa in the domain, which lies within the small tolerance for constraint violation set in the optimizer. In Figures 60c and 60d, we observe in each case, the maximum stresses in the design appear along the top edge of the structure and near the applied load. From Figure 60d, by reconfiguring the shape of the top surface of the structure, a maximum stress of only 45.2 MPa was achieved.

Another important difference between the results is the overall distribution of stress. Again, referring to Figure 60c, a very uniform stress distribution is evident in the stress-constrained design. This contrasts sharply with that observed in Figure 60d produced by the minimum stress measure design, which contains large portions of under-stressed material and areas of high stress along the edges of the structure. Especially in thermal design, the uniformly stressed structure is preferred because under-stressed material is not only inefficient from a weight perspective, but also serves only to add additional design dependent loading to the domain, which may complicate other design criteria such as buckling.

Finally, small amounts of gray material are observed in both designs that are not associated with the density filter. In these problems, the root of this material is different. For the stress-constrained design, the spurious gray material is due to small oscillations near the end of optimization in regions of zero (or nearly zero) density. It is likely that this effect can be removed by simply applying the Heaviside projection filter to damp these numerical artifacts. On the other hand, the gray material observed in the minimum stress measure design, which we observe to have higher density when compared to the stress-constrained design, results because, much the minimum compliance problem with thermal loading, the optimization problem is not sufficiently constrained. In general, to remove gray material in density-based topology optimization, an active constraint (not simply nearly active as observed here) is required to achieve a “penalizing” effect from the interpolation schemes. This need is satisfied when minimizing material usage with stress constraints as the optimum structure is naturally one that utilizes only enough material to satisfy stress constraints. This does not occur for a minimum stress measure objective. Ultimately, in the presence of thermal or other design dependent loading effects, utilizing more material (up to the constraining limit) does not result in a more benign stress state. As a result, obtain a fully solid/void design for this problem formulation, an additional constraint is required that be unconditionally active in the final design. To this point, a suitable constraint that does not impede the evolution of the structure, such as one imposed directly on the percentage of gray material, has yet to be identified.

### 5.6.2 Effectiveness of Adaptive Stress Measure

As mentioned previously, the adaptive technique utilized for the stress constraint actually results in a different numerical optimization problem, which may cause troubles with convergence. The additional iteration history for the stress

measure  $PN$  and actual maximum stress for the stress-constrained problem are given in Figure 61.

In the figure, the blue and red curves (measured on the left axis) represent the  $PN$  measure and adaptively scaled  $PN$  measure, respectively. The black curve (measured on the right axis) gives the actual maximum von Mises stress in the designable domain. The effect of adapting the aggregation measure is observed as the discrepancy between the red and blue curves. We note that after only a few iterations, the difference between the curves begins to stabilize before reaching a nearly constant value after approximately 50 iterations. This convergence results in the the maximum stress limit of 50 MPa being perfectly captured at the end of optimization. Had the adaptive technique not been employed, by nature of the  $p$  – *norm* function, the maximum stress would have been over-predicted. In this case, by investigating the difference between the red and blue curves, a design would have resulted that was over conservative by a factor of 2 to 3. Finally, on closer inspection, no significant numerical issues are apparent from the adaptive constraint. This implies the process is robust against slight variations in the optimization problem between iterations.

## 5.7 Chapter Summary

In this chapter, the problems associated with including stress-based design criteria in a density-based topology optimization problem have been discussed and methods were proposed to circumvent them. The singularity phenomena is removed using a relaxation technique and an adaptive technique has been developed to increase the resolution of an aggregation function when used with elemental stress values. These techniques were then demonstrated on a benchmark problem with two topology optimization problems with stress-criteria and combined thermal and mechanical loading. Early results indicate that stress criteria perform well in the presence of thermal loading and may yield a viable alternative to the ineffective minimum compliance formulations for thermoelasticity. In the future, to further test this conclusion, additional problems must be solved using various geometries and different combinations of thermal and mechanical loading.

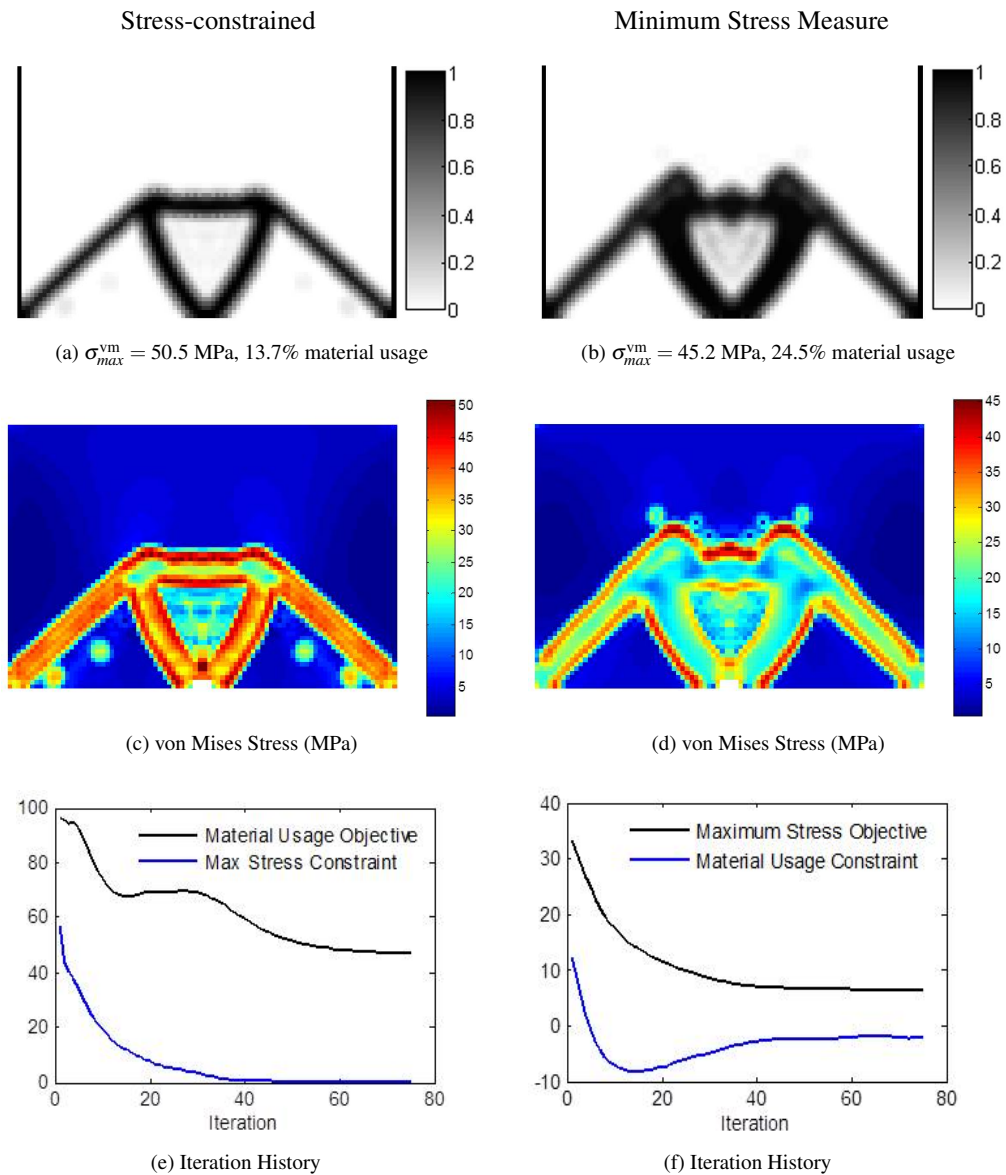


Figure 60: (a,b) Density distribution, (c,d) von Mises stress distribution, and (e,f) iteration history for both the stress-constrained and minimum stress measure problems. Stress constrained results given in the left column and minimum stress measure results in the right column.

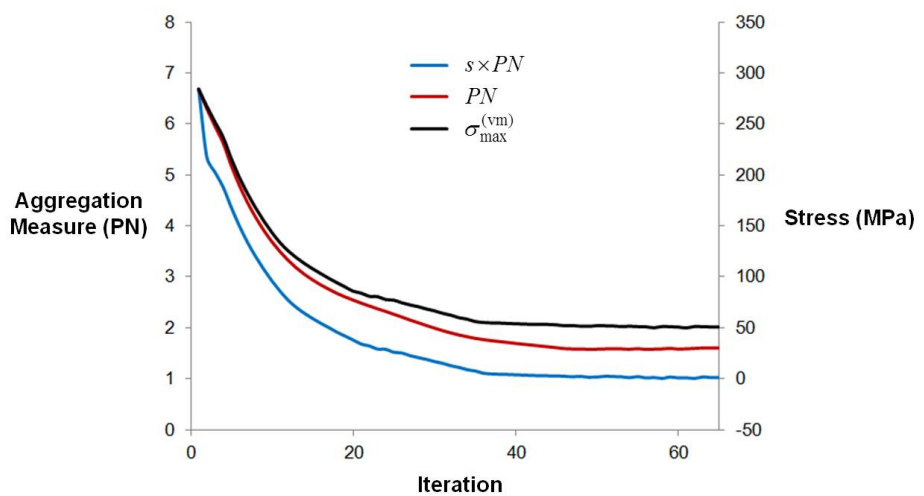


Figure 61: Iteration history for the  $PN$  measure, adapted/scaled  $PN$  value, and actual maximum stress in the stress-constrained demonstration problem.

## 6 Future Work

The developments in the previous two chapters related to the topology optimization for thermoelasticity represent some basic tools that can be utilized for the design of engine exhaust-washed structures. To date, the developed techniques have been demonstrated on various benchmark problems with prescribed temperature distributions. A natural extension that significantly enhances the capabilities of these methods is to include design dependent temperature loading in the topology optimization. In addition, further demonstration examples are necessary to show the generality and exhibit the effectiveness of topology optimization for both EEWs systems and other thermal structures. To this end, future work addressing these topics is now highlighted.

### 6.1 Coupled Thermal-Structural Topology Optimization

Including the design dependent physics of heat transfer in the topology optimization of thermal structures is an important consideration. The assumptions of a prescribed temperature distribution that have been utilized thus far serve as only approximations for the true thermal environment. In the actual physical scenario, temperature loads are a result of heat flux across boundary surfaces that is conducted throughout the structure. This leads to spatially varying distributions that are likely heavily influenced by density variations during the course of the topology optimization process. Referencing the beam strip stiffening example, Figure 62 shows a theoretical EEWs design case where heat transfer effects are considered. Here, we see that the effect of hot exhaust gas is more appropriately represented as a flux boundary condition, from which thermal energy is conducted through the structure. As the topology evolves, the surfaces of void regions also develop flux boundaries to represent active or convective cooling sources.

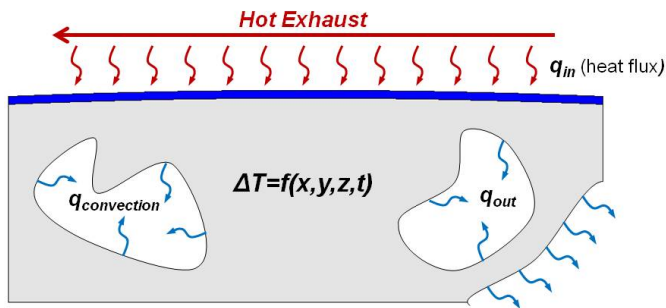


Figure 62: Example of heat transfer effects to be included in topology optimization.

While the prescribed temperature assumptions served as a valuable first step, the assertion that including design dependent heat transfer is of benefit is straight-forward. Not only does this provide a better representation of the true loading environment, but it also affords additional freedom to the topology optimization, which may enable better designs. Reducing temperatures in a thermal structure is perhaps the most obvious way to reduce the severity of design criteria such as thermal stresses or buckling. When heating is represented as a heat flux, a structure that is

more effectively cooled by efficient conduction paths and convective and radiative heat loss will likely possess superior thermoelastic performance when compared to one that maintains higher temperatures due to limited cooling. This possibility is unlocked by making the temperature distribution sensitive to the topology design process. A finite element formulation that can be used for the combined heat transfer and structural analysis is now highlighted with the sensitivity analysis necessary for topology optimization.

### 6.1.1 Finite Element Formulation

The steady-state, linear thermoelastic scenario can be analyzed using the finite element systems

$$\mathbf{K}_t(\mathbf{x})\mathbf{T}(\mathbf{x}) = \mathbf{F}_t(\mathbf{x}) \quad (87)$$

$$\mathbf{K}(\mathbf{x})\mathbf{U}(\mathbf{x}) = \mathbf{F}^m + \mathbf{F}^{th}(\mathbf{T}(\mathbf{x}), \mathbf{x}) \quad (88)$$

where Equations (87) and (88) represent the heat transfer and structural systems, respectively. Here  $\mathbf{K}_t$  is the conductivity matrix,  $\mathbf{T}$  is the nodal temperature vector, and  $\mathbf{F}_t$  is the load vector for heat transfer. Variables in Equation (88) remain consistent with definitions in Section 4.2; however, we note now that the thermal load vector in (88) is dependent on the temperature result from Equation (87).

Topology optimization for the coupled system is accomplished by parameterizing both finite element systems with density variables. Assuming conduction and free convection through a film coefficient are included in the heat transfer analysis, both the thermal conductivity and convection film coefficient must be interpolated. The element conductivity matrix for heat conduction is given by

$$\mathbf{k}_{c,e} = \int_{\Omega_e} \mathbf{B}^T k \mathbf{B} d\Omega_e, \quad (89)$$

and can be parameterized using a conventional interpolation scheme applied to the thermal conductivity  $k$ . The convection contributions to the global conductivity matrix  $\mathbf{K}_t$  and load vector  $\mathbf{F}_t$ , given at the element level by

$$\mathbf{k}_{h,e} = \int_{S_e} h \mathbf{N}^T \mathbf{N} dS_e \quad (90)$$

$$\mathbf{f}_{h,e} = \int_{S_e} h T_e \mathbf{N} dS_e, \quad (91)$$

will require more advanced interpolation of the convection coefficient  $h$ , likely based on the technique demonstrated by Bruns [88]. In the preceding relationships,  $\Omega_e$  is the volume domain of element  $e$ ,  $S_e$  is the surface on which convection is applied at  $e$ , and  $\mathbf{N}$  is the vector of shape functions, whose spatial derivatives are contained in  $\mathbf{B}$ . Finally, the structural system is parameterized as described in Section 4.2.

### 6.1.2 Sensitivity Analysis

The sensitivity analysis for the coupled heat transfer and structural problem is accomplished using a coupled adjoint solution. Assuming that topology optimization objectives and constraints are computed from displacement results obtained from Equation (88), the sensitivity analysis is formulated by first taking the derivative of a general function  $f(\mathbf{U}(\mathbf{x}))$  with respect to the physical density  $\rho_j$  as

$$\frac{df}{d\rho_j} = \frac{\partial f}{\partial \rho_j} + \frac{\partial f}{\partial \mathbf{U}} \frac{d\mathbf{U}}{d\rho_j}. \quad (92)$$

Differentiating the structural system in Equation (88), the sensitivity of the displacement vector to the density is obtained as

$$\frac{d\mathbf{U}}{d\rho_j} = \mathbf{K}^{-1} \left( \frac{d\mathbf{F}^{th}}{d\rho_j} - \frac{d\mathbf{K}}{d\rho_j} \mathbf{U} \right). \quad (93)$$

Substituting (93) into (92) yields

$$\frac{df}{d\rho_j} = \frac{\partial f}{\partial \rho_j} + \frac{\partial f}{\partial \mathbf{U}} \mathbf{K}^{-1} \left( \frac{d\mathbf{F}^{th}}{d\rho_j} - \frac{d\mathbf{K}}{d\rho_j} \mathbf{U} \right) = \frac{\partial f}{\partial \rho_j} + \lambda_1^T \left( \frac{d\mathbf{F}^{th}}{d\rho_j} - \frac{d\mathbf{K}}{d\rho_j} \mathbf{U} \right) \quad (94)$$

in which the adjoint vector  $\lambda_1$  has been introduced and is determined by solving the adjoint system

$$\mathbf{K} \lambda_1 = \frac{\partial f}{\partial \mathbf{U}}. \quad (95)$$

From (88), we recall that the load vector  $\mathbf{F}^{th}$  is a function of the temperature distribution  $\mathbf{T}$ , which is no longer assumed design independent. Thus, the sensitivity of the thermal load vector in the structural analysis is expanded as

$$\frac{d\mathbf{F}^{th}}{d\rho_j} = \frac{\partial \mathbf{F}^{th}}{\partial \rho_j} + \frac{\partial \mathbf{F}^{th}}{\partial \mathbf{T}} \frac{d\mathbf{T}}{d\rho_j} \quad (96)$$

where the partial derivative term  $\partial F^{th}/\partial \rho_j$  captures the explicit sensitivity of the interpolation used in the thermal load and the terms  $(\partial F^{th}/\partial \mathbf{T})(d\mathbf{T}/d\rho_j)$  capture the implicit sensitivity of the temperature distribution  $\mathbf{T}$  to the design variable  $\rho_j$ . Including Equation (96) into (94) gives

$$\frac{df}{d\rho_j} = \frac{\partial f}{\partial \rho_j} + \lambda_1^T \left( \frac{\partial \mathbf{F}^{th}}{\partial \rho_j} + \frac{\partial \mathbf{F}^{th}}{\partial \mathbf{T}} \frac{d\mathbf{T}}{d\rho_j} - \frac{d\mathbf{K}}{d\rho_j} \mathbf{U} \right) = \frac{\partial f}{\partial \rho_j} + \lambda_1^T \left( \frac{\partial \mathbf{F}^{th}}{\partial \rho_j} - \frac{d\mathbf{K}}{d\rho_j} \mathbf{U} \right) + \lambda_1^T \frac{\partial \mathbf{F}^{th}}{\partial \mathbf{T}} \frac{d\mathbf{T}}{d\rho_j}, \quad (97)$$

which now necessitates computation of the derivative of the temperature vector to variable  $\rho_i$ . This is again accomplished by first differentiating the state equation, in this case for the heat transfer analysis, in (87) yielding

$$\frac{d\mathbf{T}}{d\rho_j} = \mathbf{K}_t^{-1} \left( \frac{d\mathbf{F}_t}{d\rho_j} - \frac{d\mathbf{K}_t}{d\rho_j} \mathbf{T} \right). \quad (98)$$

Here, for generality, the design dependency of the load vector for heat transfer  $F_t(x)$  is retained, which may not occur in all cases. Now, substituting Equations (98) into (94) yields

$$\frac{df}{d\rho_j} = \frac{\partial f}{\partial \rho_j} + \lambda_1^T \left( \frac{\partial \mathbf{F}^{th}}{\partial \rho_j} - \frac{d\mathbf{K}}{d\rho_j} \mathbf{U} \right) + \lambda_1^T \frac{\partial \mathbf{F}^{th}}{\partial \mathbf{T}} \mathbf{K}_t^{-1} \left( \frac{d\mathbf{F}_t}{d\rho_j} - \frac{d\mathbf{K}_t}{d\rho_j} \mathbf{T} \right), \quad (99)$$

to which a second adjoint vector is introduced after simplification as

$$\frac{df}{d\rho_j} = \frac{\partial f}{\partial \rho_j} + \lambda_1^T \left( \frac{\partial \mathbf{F}^{th}}{\partial \rho_j} - \frac{d\mathbf{K}}{d\rho_j} \mathbf{U} \right) + \lambda_2^T \left( \frac{d\mathbf{F}_t}{d\rho_j} - \frac{d\mathbf{K}_t}{d\rho_j} \mathbf{T} \right). \quad (100)$$

The additional adjoint vector  $\lambda_2$  is determined from

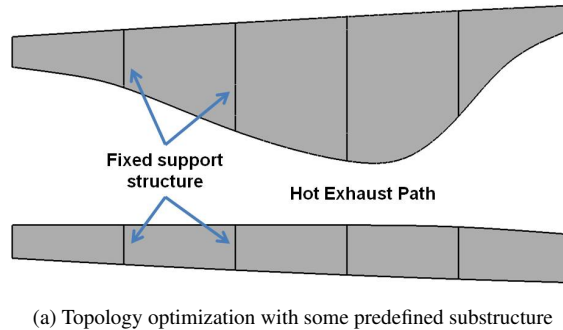
$$\mathbf{K}_t \lambda_2 = \frac{\partial \mathbf{F}^{th}}{\partial \mathbf{T}} \lambda_1. \quad (101)$$

In summary, obtaining the sensitivity of a response for topology optimization from the sequentially coupled heat transfer and structural analysis is a multistage process. First the finite element solution to the heat transfer problem in Equation (87) is obtained, which is utilized to solve for the displacement response of the structure in Equation (88). Next, the appropriate adjoint problem in Equation (95) is formulated, with the adjoint load term  $\partial f / \partial \mathbf{U}$  depending on the form of response  $f$ , and the adjoint vector  $\lambda_1$  is obtained. These results are then used in the formation of the second adjoint problem in Equation (101). Here it is important to note that if element average temperatures are utilized, the matrix  $\partial \mathbf{F}^{th} / \partial \mathbf{T}$  is a sparse matrix with the number of nonzero terms in each column equal to the number of nodes in each element and the system can be assembled quickly. Solution of the second adjoint system yields all the necessary information required for substitution into Equation (100) to obtain the final sensitivity of the response  $f$  to a design variable  $\rho_j$ . The solution of Equation (100) also benefits in efficiency because it can be solved at the element matrix level (and also in parallel), rather than the system matrix level because the partial derivative with respect to a design variable for an element yields zero sensitivity for all global induces not in that element. The solution of the additional adjoint problems has modest computational cost because the decomposed stiffness and conductivity matrices are available from the finite element solution. As a result, just as with topology optimization based on single physics analysis, the process is tractable for a reasonable number of design responses. Finally, we recall that the physical density  $\rho$ , which the preceding sensitivities have been derived with respect to, is either equal to the design

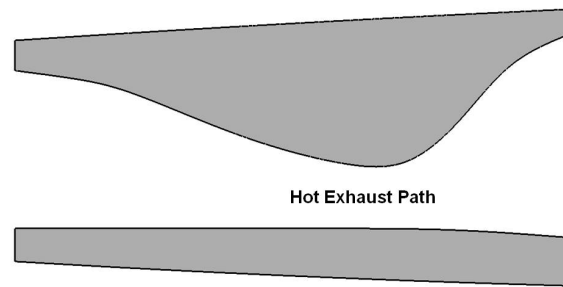
variable density  $x$  or a function of the design variable density as  $\rho_j(\mathbf{x})$  depending on the filter. With the appropriate chain rules from Section (3.2.2), the sensitivity of the function to the density design variables  $df/dx_i$ , can be obtained.

## 6.2 Topology Layout for Engine Exhaust-Washed Structures

Future work also includes additional applications of the topology optimization methods that have been developed. Thus far, the developments have been tested on benchmark problems and characteristic structures. A number of additional demonstration problems can be tested with inspiration taken from the conceptual EEWS configuration original shown in Figure 4. For example, a 2D idealization of a structure that possesses the basic deformation response of the exhaust-washed nozzle surface can be explored as shown in Figure 63. Here, we see two distinct topology optimization problems. The first problem given in Figure 63a consists of adding additional material to a pre-existing configuration to provide stiffening. Various instances of the connectivity between the design domain and predefined substructure can also be explored. A more desirable problem is the full substructure layout shown in Figure 63b, where the entire structure between the exhaust-washed surface and outer aircraft skins is designed via topology optimization. This idea could also be extended to three dimensions, where the open region in Figure 64 represents a full topology optimization design space.



(a) Topology optimization with some predefined substructure



(b) Topology optimization of full substructure domain

Figure 63: Example of topology design domains for representative 2D EEWS for (a) topology optimization with some predefined substructure and (b) full substructure design.

In addition to demonstrating the versatility of topology optimization methods for thermal structures, additional examples across a range of geometries will also provide valuable insight into the proper alignment of structural material

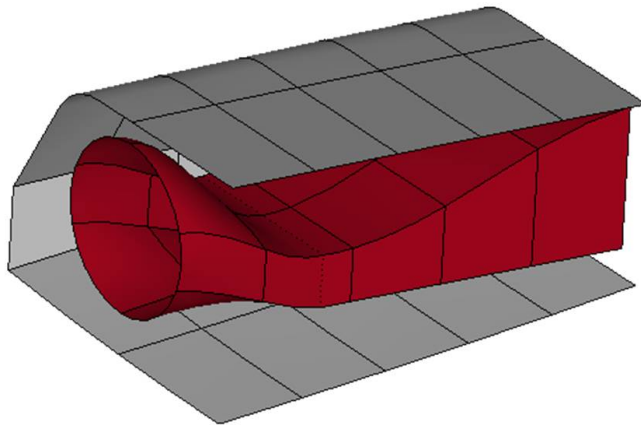


Figure 64: Example of full EEWs substructure topology optimization design domain.

for varying geometric shapes and boundary conditions in a thermal environment. Just as with the studies described in Chapter 2, this information is useful for design “rules of thumb” when working at the conceptual level and a better understanding of the structural mechanics of the thermoelastic design environment.

## 7 Research Plan Summary

New challenges presented by the unique requirements of engine exhaust-washed structures have provided the impetus for development of advanced methods for thermal structures design. By observing the basic response of this class of aerospace structures, along with the nuances related to the design of structures in a thermal environment, intuition has been gained regarding the basic features that a successful design method must possess. Of primary concern is the fundamental ability to place structural material in orientations such that it does not adversely effect the thermoelastic performance. To address this, the application of structural topology optimization, which by formulation is a material layout technique, is proposed for the design of thermal structures inspired by embedded-engine aircraft applications.

Resulting from limitations in standard techniques, the direct application of topology optimization to these problems is not possible. In fact, no existing commercial design packages or, based on thorough review of published literature, academic and research codes, have the capability to rigorously treat the engine exhaust-washed structure (EEWS) design problem. Thus, research in this direction is necessary to develop an effective design mechanism.

To this end, some limitations related to the topology optimization with thermal loading have been investigated and alternative problem formulations have been identified that are consistent with thermal structures design goals. These formulations have been demonstrated on characteristic thermal structures for both stiffening and configuration design. In addition, stress-based design criteria have also been applied to thermal stresses. As a result, methods have been developed to perform topology optimization of structures that are subjected to a predefined temperature field in addition to any combined mechanical effects. Through examples, these methods have demonstrated the possibility of tailoring the topological layout of candidate structure for improved thermoelastic performance.

Capturing the effect of topological variation on the temperature distribution in the structure is also of prime importance. In order to do this, the heat transfer physics of heat conduction, free convection, and radiation heat loss, will be parameterized and included in the topology optimization formulation. This affords the optimization process control over the heat flows throughout the structure and even greater design freedom. Analytical sensitivities for the coupled heat transfer and structural system will be developed such that the design dependency of thermal effects is accurately captured at all levels. The effectiveness of the coupled solution strategy will be demonstrated on example problems inspired by the EEWS application.

Completion of the proposed efforts is expected to provide contributions to both the aerospace design and structural optimization communities. The advanced design methods based on topology optimization will be applicable to a variety of thermal structures problems, but will provide particular value in addressing the challenges related to exhaust-washed structures. Within the structural optimization field, additional emphasis is currently placed on methods and applications that are not related to the traditional stiffness design of mechanically loaded structures, which still constitute the bulk of research knowledge. Thus, the methods to be developed for thermoelastic topology optimization

of problems with practical design criteria (i.e. not compliance-based) represent a useful application of the technique to a challenging multiphysics problem that holds real-world significance.

## References

- [1] E. A. Thornton, *Thermal Structures for Aerospace Applications*. AIAA Education Series, Reston, VA: AIAA, 1996.
- [2] B. A. Boley and J. H. Weiner, *Theory of Thermal Stresses*. John Wiley and Sons, Inc., 1960.
- [3] B. E. Gatewood, *Thermal Stresses*. McGraw-Hill Book Company, Inc., 1957.
- [4] J. J. McNamara and P. P. Friedmann, “Aeroelastic and Aerothermoelastic Analysis in Hypersonic Flow: Past, Present, and Future,” *AIAA Journal*, vol. 49, no. 6, pp. 1089–1122, 2011.
- [5] G. V. Rao, C. P. Shore, and R. Narayanaswami, “An Optimality Criterion for Resizing Heated Structures with Temperature Constraints,” *Tech. Rep. NASA TN D-8525*, 1977.
- [6] H. M. Adelman, P. L. Sawyer, and C. P. Shore, “Optimum Design of Structures at Elevated Temperatures,” *AIAA Journal*, vol. 17, pp. 622–629, June 1979.
- [7] R. T. Haftka and C. P. Shore, “Approximation Methods for Combined Thermal/Structural Design,” Technical Paper 1428, June 1979. NASA Technical Paper 1428.
- [8] S. Xu and R. V. Grandhi, “Structural Optimization with Thermal and Mechanical Constraints,” *Journal of Aircraft*, vol. 36, pp. 29–35, January–February 1999.
- [9] D. A. Tortorelli, R. B. Haber, and S. C. Y. Lu, “Design sensitivity analysis for nonlinear thermal systems,” *Computer Methods in Applied Mechanics and Engineering*, vol. 77, pp. 61–77, 1989.
- [10] D. A. Tortorelli, G. Subramani, and S. C. Y. Lu, “Sensitivity analysis for coupled thermelastic systems,” *International Journal of Solids and Structures*, vol. 27, no. 12, pp. 1477–1497, 1991.
- [11] M. Bhatia and E. Livne, “Design-Oriented Thermostructural Analysis with External and Internal Radiation, Part 1: Steady State,” *AIAA Journal*, vol. 46, pp. 578–590, March 2008.
- [12] M. Bhatia and E. Livne, “Design-Oriented Thermostructural Analysis with External and Internal Radiation, Part 2: Transient Response,” *AIAA Journal*, vol. 47, pp. 1228–1240, May 2009.
- [13] R. F. Barron and B. R. Barron, *Design for Thermal Stresses*. Hoboken, NJ: John Wiley & Sons, Inc., 2012.
- [14] J. Paterson, “Overview of Low Observable Technology and Its Effects on Combat Aircraft Survivability,” *Journal of Aircraft*, vol. 36, pp. 380–388, March–April 1999.

- [15] M. A. Haney and R. V. Grandhi, “Consequences of Material Addition for a Beam Strip in a Thermal Environment,” *AIAA Journal*, vol. 47, pp. 1026–1034, April 2009.
- [16] M. A. Haney, *Topology Optimization of Engine Exhaust-Washed Structures*. PhD thesis, Wright State University, 2006.
- [17] J. S. Arora, *Introduction to Optimum Design*. Academic Press, 2 ed., 2004.
- [18] D. L. Allison, C. C. Morris, J. A. Schetz, R. K. Kapania, J. D. Deaton, and R. V. Grandhi, “Development of a Multidisciplinary Design Optimization Framework for an Efficient Supersonic Air Vehicle,” *AIAA Journal*, p. submitted, 2013.
- [19] B. D. Flansburg, S. P. Engelstad, and J. Lua, “Robust Design of Composite Bonded Pi Joints,” in *50th AIAA/ASME/AASCE/AHS/ASC Structures, Structural Dynamics, and Materials Conference*, (Palm Springs, CA), May 2009.
- [20] MSC.Software, *MD Nastran 2010 Quick Reference Guide*. Santa Ana, CA, 2010.
- [21] E. R. Van Driest, “The Problem of Aerodynamic Heating,” *Aeronautical Engineering Review*, vol. 15, no. 10, pp. 26–41, 1956.
- [22] E. R. G. Eckert, “Engineering Relations for Heat Transfer and Friction in High-Velocity Laminar and Turbulent Boundary-Layer Flow Over Surfaces with Constant Pressure and Temperature,” *Transactions of the ASME*, vol. 78, no. 6, pp. 1273–1283, 1956.
- [23] Cytec, “CYCOM 5250-4 Prepreg System - Technical Data Sheet,” tech. rep., Cytec Engineered Materials, March 2012.
- [24] S. T. Gonczy and J. G. Sikonia, “Nextel 312/Silicon Oxycarbide Ceramic Composites,” in *Handbook of Ceramic Composites* (N. P. Bansal, ed.), ch. 15, pp. 347–373, Springer US, 2005.
- [25] K. K. Chawla, *Ceramic Matrix Composites*. Springer, 2 ed., 2003.
- [26] R. D. Cook, D. S. Malkus, M. E. Plesha, and R. J. Witt, *Concepts and Applications of Finite Element Analysis*. John Wiley & Sons, Inc., 2001.
- [27] G.-J. Park, “Technical overview of the equivalent static loads method for non-linear static response structural optimization,” *Structural and Multidisciplinary Optimization*, vol. 43, pp. 319–337, 2011.
- [28] M. P. Bendsøe and O. Sigmund, *Topology Optimization: Theory, Methods and Applications*. Springer, 2nd ed., 2003.

- [29] H. A. Eschenauer and N. Olhoff, “Topology optimization of continuum structures: A review,” *Applied Mechanics Reviews*, vol. 54, no. 4, pp. 331–390, 2001.
- [30] G. I. N. Rozvany, “Aims, scope, methods, history and unified terminology of computer-aided topology optimization in structural mechanics,” *Structural and Multidisciplinary Optimization*, vol. 21, no. 2, pp. 90–108, 2001.
- [31] M. P. Bendsøe and N. Kikuchi, “Generating optimal topologies in structural design using a homogenization method,” *Computer Methods in Applied Mechanics and Engineering*, vol. 71, pp. 198–224, 1988.
- [32] M. P. Bendsøe, “Optimal shape design as a material distribution problem,” *Structural Optimization*, vol. 1, no. 4, pp. 193–202, 1989.
- [33] G. I. N. Rozvany, M. Zhou, and T. Birker, “Generalized shape optimization without homogenization,” *Structural Optimization*, vol. 4, pp. 250–254, 1992.
- [34] M. Stolpe and K. Svanberg, “An alternative interpolation scheme for minimum compliance topology optimization,” *Structural and Multidisciplinary Optimization*, vol. 22, no. 2, pp. 116–124, 2001.
- [35] T. E. Bruns, “A reevaluation of the SIMP method with filtering and an alternative formulation for solid-void topology optimization,” *Structural and Multidisciplinary Optimization*, vol. 30, no. 6, pp. 428–436, 2005.
- [36] O. Sigmund and J. Petersson, “Numerical instabilities in topology optimization: A survey on procedures dealing with checkerboards, mesh-dependencies, and local minima,” *Structural Optimization*, vol. 16, no. 1, pp. 68–75, 1998.
- [37] B. Bourdin, “Filters in topology optimization,” *International Journal for Numerical Methods in Engineering*, vol. 50, no. 9, pp. 2143–2158, 2001.
- [38] T. E. Bruns and D. A. Tortorelli, “Topology optimization of non-linear elastic structures and compliant mechanisms,” *Computer Methods in Applied Mechanics and Engineering*, vol. 190, no. 26-27, pp. 3443–3459, 2001.
- [39] J. K. Guest, J. H. Prévost, and T. Belytschko, “Achieving minimum length scale in topology optimization using nodal design variables and projection functions,” *International Journal for Numerical Methods in Engineering*, vol. 61, no. 2, pp. 238–254, 2004.
- [40] O. Sigmund, “Morphology-based black and white filters for topology optimization,” *Structural and Multidisciplinary Optimization*, vol. 33, no. 4-5, pp. 401–424, 2007.
- [41] O. Sigmund and K. Maute, “Sensitivity filtering from a continuum mechanics perspective,” *Structural and Multidisciplinary Optimization*, vol. 46, no. 4, pp. 471–475, 2012.

- [42] F. Wang, B. S. Lazarov, and O. Sigmund, “On projection methods, convergence and robust formulations in topology optimization,” *Structural and Multidisciplinary Optimization*, vol. 43, no. 6, pp. 767–784, 2011.
- [43] J. K. Guest, A. Asadpoure, and S.-H. Ha, “Eliminating beta-continuation from Heaviside projection and density filter algorithms,” *Structural and Multidisciplinary Optimization*, vol. 44, no. 4, pp. 443–453, 2011.
- [44] M. Zhou and G. I. N. Rozvany, “On the validity of ESO type methods in topology optimization,” *Structural and Multidisciplinary Optimization*, vol. 21, no. 1, pp. 80–83, 2001.
- [45] G. I. N. Rozvany, “A critical review of established methods of structural topology optimization,” *Structural and Multidisciplinary Optimization*, vol. 37, no. 3, pp. 217–237, 2009.
- [46] Y. M. Xie and G. P. Steven, *Evolutionary Structural Optimization*. Springer, 1997.
- [47] X. Huang and Y. M. Xie, *Evolutionary Topology Optimization of Continuum Structures: Methods & Applications*. John Wiley & Sons, Inc., 2010.
- [48] N. P. van Dijk, K. Maute, Langelaar, and F. van Keulen, “Level-set methods for structural topology optimization: a review,” *Structural and Multidisciplinary Optimization*, 2013.
- [49] D. Makhija and K. Maute, “Numerical instabilities in level set topology optimization with the extended finite element method,” *Structural and Multidisciplinary Optimization*, 2013.
- [50] S. J. Osher and J. A. Sethian, “Fronts propagating with curvature dependent speed: algorithms based on the Hamilton-Jacobi formulation,” *Journal of Computational Physics*, vol. 79, no. 1, pp. 12–49, 1988.
- [51] J. A. Sethian, *Level set methods and fast marching methods: evolving interfaces in computational geometry, fluid mechanics, computer vision and materials science*, vol. 3 of *Cambridge Monographs on Applied and Computational Mechanics*. Cambridge: Cambridge University Press, 2 ed., 1999.
- [52] S. J. Osher and R. Fedkiw, *Level set methods and dynamic implicit surfaces*, vol. 153 of *Applied Mathematical Sciences*. New York, NY: Springer, 2002.
- [53] J. A. Sethian and A. Wiegmann, “Structural boundary design via level set and immersed interface methods,” *Journal of Computational Physics*, vol. 163, no. 2, pp. 489–528, 2000.
- [54] S. J. Osher and F. Santosa, “Level set methods for optimization problems involving geometry and constraints I. Frequencies of a two-density inhomogenous drum,” *Journal of Computational Physics*, vol. 171, no. 1, pp. 272–288, 2001.

- [55] Z. Luo, N. Zhang, W. Gao, and H. Ma, “Structural shape and topology optimization using a meshless Galerkin level set method,” *International Journal for Numerical Methods in Engineering*, vol. 90, no. 3, pp. 369–389, 2012.
- [56] M. Y. Wang, X. Wang, and D. Guo, “A level set method for structural topology optimization,” *Computer Methods in Applied Mechanics and Engineering*, vol. 192, no. 1-2, pp. 227–246, 2003.
- [57] P. D. Dunning and H. A. Kim, “A new hole insertion method for level set based structural topology optimization,” *International Journal for Numerical Methods in Engineering*, vol. 93, pp. 118–134, 2013.
- [58] L.-Q. Chen, “Phase-field models for microstructure evolution,” *Annual Review of Materials Research*, vol. 32, no. 32, pp. 113–140, 2002.
- [59] A. Takezawa, S. Nishiwaki, and M. Kitamura, “Shape and topology optimization based on the phase field method and sensitivity analysis,” *Journal of Computational Physics*, vol. 229, no. 7, pp. 2697–2718, 2010.
- [60] M. Y. Wang and S. Zhou, “Phase field: a variational method for structural topology optimization,” *Computer Modeling in Engineering and Sciences*, vol. 6, no. 6, pp. 547–566, 2004.
- [61] B. Bourdin and A. Chambolle, “The Phase-Field Method in Optimal Design,” in *IUTAM Symposium on Topological Design Optimization of Structures, Machines and Materials* (M. P. Bendsøe, N. Olhoff, and O. Sigmund, eds.), vol. 137 of *Solid Mechanics and Its Applications*, pp. 207–215, Springer, 2006.
- [62] M. H. Kobayashi, “On a biologically inspired topology optimization method,” *Communications in Nonlinear Science and Numerical Simulation*, vol. 15, no. 3, pp. 787–802, 2010.
- [63] A. Nakamura, A. Lindenmeyer, and K. Aizawa, *Some Systems for Map Generation*. The Book of L, Springer, 1986.
- [64] B. Stanford, P. Beran, and M. H. Kobayashi, “Aeroelastic Optimization of Flapping Wing Venation: A Cellular Division Approach,” *AIAA Journal*, vol. 50, pp. 938–951, April 2012.
- [65] J. D. Deaton and R. V. Grandhi, “A survey of structural and multidisciplinary continuum topology optimization: post 2000,” *Structural and Multidisciplinary Optimization*, 2013.
- [66] O. Sigmund and K. Maute, “Topology optimization approaches,” *Structural and Multidisciplinary Optimization*, 2013.
- [67] H. Rodrigues and P. Fernandes, “A material based model for topology optimization of thermoelastic structures,” *International Journal for Numerical Methods in Engineering*, vol. 38, pp. 1951–1965, 1995.

- [68] Q. Xia and M. Y. Wang, “Topology optimization of thermoelastic structures using level set method,” *Computational Mechanics*, vol. 42, no. 6, pp. 837–857, 2008.
- [69] C. Jog, “Distributed-parameter optimization and topology design for non-linear thermoelasticity,” *Computer Methods in Applied Mechanics and Engineering*, vol. 132, pp. 117–134, 1996.
- [70] P. Pedersen and N. L. Pedersen, “Strength optimized designs of thermoelastic structures,” *Structural and Multidisciplinary Optimization*, vol. 42, no. 5, pp. 681–691, 2010.
- [71] P. Pedersen and N. L. Pedersen, “Interpolation/penalization applied for strength design of 3D thermoelastic structures,” *Structural and Multidisciplinary Optimization*, vol. 42, no. 6, pp. 773–786, 2012.
- [72] T. Gao and W. Zhang, “Topology optimization involving thermo-elastic stress loads,” *Structural and Multidisciplinary Optimization*, vol. 42, no. 5, pp. 725–738, 2010.
- [73] Q. Li, G. P. Steven, O. M. Querin, and Y. Xie, “Optimization of thin shell structures subjected to thermal loading,” *Structural Engineering and Mechanics*, vol. 7, no. 4, pp. 401–412, 1999.
- [74] Q. Li, G. P. Steven, and Y. Xie, “Displacement minimization of thermoelastic structures by evolutionary thickness design,” *Computer Methods in Applied Mechanics and Engineering*, vol. 179, pp. 361–378, 1999.
- [75] W.-Y. Kim, R. V. Grandhi, and M. A. Haney, “Multiobjective Evolutionary Structural Optimization Using Combined Static/Dynamic Control Parameters,” *AIAA Journal*, vol. 44, pp. 794–802, April 2006.
- [76] B. Wang, J. Yan, and G. Cheng, “Optimal structure design with low thermal directional expansion and high stiffness,” *Engineering Optimization*, vol. 43, no. 6, pp. 581–595, 2011.
- [77] J. Deng, J. Yan, and G. Cheng, “Multi-objective concurrent topology optimization of thermoelastic structures composed of homogeneous porous material,” *Structural and Multidisciplinary Optimization*, vol. 47, pp. 583–597, 2013.
- [78] X. Yang and Y. Li, “Topology optimization to minimize the dynamic compliance of a bi-material plate in a thermal environment,” *Structural and Multidisciplinary Optimization*, vol. 47, pp. 399–408, 2013.
- [79] X. Yang and Y. Li, “Structural topology optimization on dynamic compliance at resonance frequency in thermal environments,” *Structural and Multidisciplinary Optimization*, 2013.
- [80] B. Stanford and P. Beran, “Aerothermoelastic topology optimization with flutter and buckling metrics,” *Structural and Multidisciplinary Optimization*, vol. 48, pp. 149–171, 2013.

- [81] O. Sigmund and S. Torquato, “Design of materials with extreme thermal expansion using a three-phase topology optimization method,” *Journal of the Mechanics and Physics of Solids*, vol. 45, no. 6, pp. 1037–1067, 1997.
- [82] A. Gersborg-Hansen, M. P. Bendsøe, and O. Sigmund, “Topology optimization of heat conduction problems using the finite volume method,” *Structural and Multidisciplinary Optimization*, vol. 31, no. 4, pp. 251–259, 2006.
- [83] G. P. Steven, Q. Li, and Y. M. Xie, “Evolutionary topology and shape design for general physical field problems,” *Computational Mechanics*, vol. 26, no. 2, pp. 129–139, 2000.
- [84] Q. Li, G. P. Steven, Y. M. Xie, and O. M. Querin, “Evolutionary topology optimization for temperature reduction of heat conducting fields,” *International Journal for Heat and Mass Transfer*, vol. 47, no. 23, pp. 5071–5083, 2004.
- [85] T. Gao, W. H. Zhang, J. H. Zhu, Y. J. Xu, and D. H. Bassir, “Topology optimization of heat conduction problem involving design-dependent load effect,” *Finite Elements in Analysis and Design*, vol. 44, no. 14, pp. 805–813, 2008.
- [86] S. H. Ha and S. Cho, “Topological shape optimization of heat conduction problems using level set approach,” *Numerical Heat Transfer, Part B: Fundamentals: An International Journal of Computation and Methodology*, vol. 48, no. 1, pp. 67–88, 2005.
- [87] C. G. Zhuang, Z. H. Xiong, and H. Ding, “A level set method for topology optimization of heat conduction problem under multiple load cases,” *Computer Methods in Applied Mechanics and Engineering*, vol. 196, no. 4–6, pp. 1074–1084, 2007.
- [88] T. E. Bruns, “Topology optimization of convection-dominated, steady-state heat transfer problems,” *International Journal for Heat and Mass Transfer*, vol. 50, no. 15-16, pp. 2859–2873, 2007.
- [89] A. Iga, S. Nishiwaki, K. Izui, and M. Yoshimura, “Topology optimization for thermal conductors considering design-dependent effects, including heat conduction and convection,” *International Journal for Heat and Mass Transfer*, vol. 52, pp. 2721–2732, 2009.
- [90] S. Cho and J.-Y. Choi, “Efficient topology optimization of thermo-elasticity problems using coupled field adjoint sensitivity analysis method,” *Finite Elements in Analysis and Design*, vol. 41, no. 15, pp. 1481–1495, 2005.
- [91] Q. Li, G. P. Steven, O. M. Querin, and Y. M. Xie, “Structural topology design with multiple thermal criteria,” *Engineering Computations*, vol. 17, no. 6, pp. 715–734, 2000.

- [92] Q. Li, G. P. Steven, and Y. M. Xie, “Thermoelastic Topology Optimization for Problems with Varying Temperature Fields,” *Journal of Thermal Stresses*, vol. 24, no. 4, pp. 347–366, 2001.
- [93] O. Sigmund, “Design of multiphysics actuators using topology optimization - Part I: One-material structures,” *Computer Methods in Applied Mechanics and Engineering*, vol. 190, no. 49-50, pp. 6577–6604, 2001.
- [94] O. Sigmund, “Design of multiphysics actuators using topology optimization - Part II: Two-material structures,” *Computer Methods in Applied Mechanics and Engineering*, vol. 190, no. 49-50, pp. 6605–6627, 2001.
- [95] R. Ansola, E. Veguería, J. Canales, and C. Alonso, “Evolutionary optimization of compliant mechanisms subjected to non-uniform thermal effects,” *Finite Elements in Analysis and Design*, vol. 57, pp. 1–14, 2012.
- [96] Z. Luo, L. Tong, and H. Ma, “Shape and topology optimization for electrothermomechanical microactuators using level set methods,” *Journal of Computational Physics*, vol. 228, no. 9, pp. 3173–3181, 2009.
- [97] Y. Li, K. Saitou, and N. Kikuchi, “Topology optimization of thermally actuated compliant mechanisms considering time-transient effect,” *Finite Elements in Analysis and Design*, vol. 40, pp. 1317–1331, 2004.
- [98] P. Duysinx and M. P. Bendsøe, “Topology optimization of continuum structures with local stress constraints,” *International Journal for Numerical Methods in Engineering*, vol. 43, pp. 1453–1478, 1998.
- [99] G. Cheng and Z. Jiang, “Study on topology optimization with stress constraints,” *Engineering Optimization*, vol. 20, no. 2, pp. 129–148, 1992.
- [100] G. Cheng and X. Guo, “Epsilon-relaxed approach in structural topology optimization,” *Structural Optimization*, vol. 13, pp. 258–266, 1997.
- [101] J. Pereira, E. Fancello, and C. Barcellos, “Topology optimization of continuum structures with material failure constraints,” *Structural and Multidisciplinary Optimization*, vol. 26, no. 1-2, pp. 50–66, 2004.
- [102] F. Navarrina, I. Muiños, I. Colominas, and M. Casteleiro, “Topology optimization of structures: A minimum weight approach with stress constraints,” *Advances in Engineering Software*, vol. 36, no. 9, pp. 599–606, 2005.
- [103] M. Bruggi, “On an alternative approach to stress constraints relaxation in topology optimization,” *Structural and Multidisciplinary Optimization*, vol. 36, no. 2, pp. 125–141, 2008.
- [104] M. Bruggi and P. Venini, “A mixed FEM approach to stress-constrained topology optimization,” *International Journal for Numerical Methods in Engineering*, vol. 73, no. 12, pp. 1693–1714, 2008.
- [105] J. París, F. Navarrina, I. Colominas, and M. Casteleiro, “Topology optimization of continuum structures with local and global stress constraints,” *Structural and Multidisciplinary Optimization*, vol. 39, no. 4, pp. 419–437, 2009.

- [106] C. E. M. Guilherme and J. S. O. Fonesca, “Topology optimization of continuum structures with epsilon-relaxed stress constraints,” in *International Symposium on Solid Mechanics* (M. Alves and H. da Costa Mattos, eds.), vol. 1 of *Mechanics of Solids in Brazil*, pp. 239–250, Brazilian Society of Mechanical Sciences in Engineering, 2007.
- [107] C. Le, J. Norato, T. E. Bruns, C. Ha, and D. A. Tortorelli, “Stress-based topology optimization for continua,” *Structural and Multidisciplinary Optimization*, vol. 41, no. 4, pp. 605–620, 2010.
- [108] J. París, F. Navarrina, I. Colominas, and M. Casteleiro, “Global versus Local Statement of Stress Constraints in Topology Optimization,” in *Computer Aided Optimum Design of Structures* (M. Alves and H. da Costa Mattos, eds.), pp. 13–23, Southampton: WIT Press, 2007.
- [109] G. Y. Qiu and X. S. Li, “A note on the derivation of global stress constraints,” *Structural and Multidisciplinary Optimization*, vol. 40, pp. 625–628, 2010.
- [110] J. París, F. Navarrina, I. Colominas, and M. Casteleiro, “Block aggregation of stress constraints in topology optimization of structures,” *Advances in Engineering Software*, vol. 41, no. 3, pp. 433–441, 2010.
- [111] J. París, F. Navarrina, I. Colominas, and M. Casteleiro, “Improvements in the treatment of stress constraints in structural topology optimization problems,” *Journal of Computational and Applied Mathematics*, vol. 234, no. 7, pp. 2231–2238, 2010.
- [112] E. Holmberg, B. Torstenfelt, and A. Klarbring, “Stress constrained topology optimization,” *Structural and Multidisciplinary Optimization*, 2013.
- [113] Y. Luo, M. Y. Wang, and Z. Kang, “An enhanced aggregation method for topology optimization with local stress constraints,” *Computer Methods in Applied Mechanics and Engineering*, vol. 254, pp. 31–41, 2013.
- [114] F. V. Stump, E. C. N. Silva, and G. H. Paulino, “Optimization of material distribution in functionally graded structures with stress constraints,” *Communications in Numerical Methods in Engineering*, vol. 23, no. 6, pp. 535–551, 2007.
- [115] Y. Luo and Z. Kang, “Topology optimization of continuum structures with Drucker-Prager yield stress constraints,” *Computers and Structures*, vol. 90-91, no. 90-91, pp. 65–75, 2012.
- [116] E. Lee, K. A. James, and J. R. R. A. Martins, “Stress-constrained topology optimization with design-dependent loading,” *Structural and Multidisciplinary Optimization*, vol. 46, no. 5, pp. 647–661, 2012.
- [117] M. Bruggi and P. Duysinx, “Topology optimization for minimum weight with compliance and stress constraints,” *Structural and Multidisciplinary Optimization*, vol. 46, pp. 369–384, 2012.

- [118] K. Sherif, W. Witteveen, K. Puchner, and H. Irschik, “Efficient Topology Optimization of Large Dynamic Finite Element Systems Using Fatigue,” *AIAA Journal*, vol. 48, no. 7, pp. 1339–1347, 2010.
- [119] G. Allaire and F. Jouve, “Minimum stress optimal design with the level set method,” *Engineering Analysis with Boundary Elements*, vol. 32, no. 11, pp. 909–918, 2008.
- [120] X. Guo, W. S. Zhang, M. Y. Wang, and P. Wei, “Stress-related topology optimization via level set approach,” *Computer Methods in Applied Mechanics and Engineering*, vol. 200, no. 47-48, pp. 3439–3452, 2011.
- [121] M. Y. Wang and L. Li, “Shape equilibrium constraint: a strategy for stress-constrained structural topology optimization,” *Structural and Multidisciplinary Optimization*, vol. 47, pp. 335–352, 2013.
- [122] M. Burger and R. Stainko, “Phase-field relaxation of topology optimization with local stress constraints,” *SIAM Journal of Control and Optimization*, vol. 45, no. 4, pp. 1447–1466, 2006.
- [123] A. C. Urugal and S. K. Fenster, *Advanced Mechanics of Materials and Applied Elasticity*. Prentice Hall, 5 ed., 2011.